UNIVERSIDADE FEDERAL DO RIO GRANDE DO NORTE
CENTRO DE CIÊNCIAS EXATAS E DA TERRA
PROGRAMA DE PÓS-GRADUAÇÃO EM
GEODINÂMICA E GEOFÍSICA

TESE DE DOUTORADO

INFLUÊNCIA DE DESCONTINUIDADES ESTRUTURAIS E SEDIMENTARES NA POROSIDADE CÁRSTICA DA FORMAÇÃO JANDAÍRA, BACIA POTIGUAR

Autora:
Renata Emily Brito de Araújo

Orientador:
Prof. Dr. Francisco Hilário Rego Bezerra (DG/PPGG/UFRN)

Coorientador:
Dr. Vincenzo La Bruna (PPGG/UFRN)

Tese nº 73/PPGG

Setembro de 2022

Natal/RN, Brasil

UNIVERSIDADE FEDERAL DO RIO GRANDE DO NORTE
CENTRO DE CIÊNCIAS EXATAS E DA TERRA
PROGRAMA DE PÓS-GRADUAÇÃO EM
GEODINÂMICA E GEOFÍSICA

RENATA EMILY BRITO DE ARAÚJO

INFLUÊNCIA DE DESCONTINUIDADES ESTRUTURAIS E SEDIMENTARES NA POROSIDADE CÁRSTICA DA FORMAÇÃO JANDAÍRA, BACIA POTIGUAR

Tese apresentada em 08 de setembro de 2022 ao Programa de Pós-Graduação em Geodinâmica e Geofísica (PPGG) da Universidade Federal do Rio Grande do Norte (UFRN) como requisito à obtenção do Título de Doutor em Geodinâmica e Geofísica, Área de Concentração Geodinâmica.

BANCA EXAMINADORA:

____
PROF. DR. FRANCISCO HILÁRIO REGO BEZERRA
Presidente e orientador (PPGG-UFRN)

____
PROF. DR. FRANCISCO PINHEIRO LIMA FILHO
Membro interno (PPGG-UFRN)

____
PROF. DRA. MARCELA MARQUES VIEIRA
Membro interno (DGEO-UFRN)

____
PROF. DRA. PAOLA FERREIRA BARBOSA
Membro externo (IG-UnB)

____
DR. FABIO LUIZ BAGNI
Membro externo (Petrobras)

Universidade Federal do Rio Grande do Norte - UFRN
Sistema de Bibliotecas - SISBI
Catalogação de Publicação na Fonte. UFRN - Biblioteca Central Zila Mamede

Araújo, Renata Emily Brito de.
Influência de descontinuidades estruturais e sedimentares na porosidade cárstica da Formação Jandaíra, Bacia Potiguar / Renata Emily Brito de Araújo. - 2022.
144 f.: il.

Tese (doutorado) - Universidade Federal do Rio Grande do Norte, Centro de Ciências Exatas e da Terra, Programa de Pós-Graduação em Geodinâmica e Geofísica, Natal, RN, 2022.
Orientador: Prof. Dr. Francisco Hilário Rêgo Bezerra.
Coorientador: Dr. Vincenzo La Bruna.

1. Carste - Tese. 2. Reservatório - Tese. 3. Dissolução - Tese. 4. Diagênese - Tese. 5. Estilólito - Tese. 6. Fratura - Tese. I. Bezerra, Francisco Hilário Rêgo. II. Bruna, Vincenzo La. III. Título.

RN/UF/BCZM CDU 550.3

Elaborado por Ana Cristina Cavalcanti Tinoco - CRB-15/262

AGRADECIMENTOS

Agradeço aos meus pais e as minhas irmãs por todo apoio e dedicação que sempre tiveram no meu desenvolvimento e educação. Agradeço à André por seu companheirismo e conselhos durante esse doutorado, em especial no período de pandemia.

Ao Professor Dr. Francisco Hilário Bezerra por ter me orientado no mestrado e doutorado e ter me proporcionado muito aprendizado nesse período. Ao meu amigo e co-orientador Vincenzo La Bruna, por todo o suporte no desenvolvimento da pesquisa, pelas diversas oportunidades de discussões técnicas, por todo o apoio quando me sentia aflita.

À Universidade Federal do Rio Grande do Norte e ao Programa de Pós-Graduação em Geodinâmica e Geofísica (PPGG-UFRN) e ao projeto acadêmico Porocarste 3D/Shell pela oportunidade de estudo e aprendizado. Esta pesquisa foi realizada em associação com o projeto de P&D em andamento registrado como ANP 20502–1, "Processos e Propriedades em Reservatórios Carbonáticos Fraturados e Carstificados – POROCARSTE 3D" (UFRN / UNB / UFRJ / UFC / Shell Brasil / ANP) – Porokarst – Processos e Propriedades em Reservatórios de Carbonato Fraturados e Karstificados, patrocinados pela Shell Brasil sob a taxa de P&D da ANP como "Compromisso de Investimento com Pesquisa e Desenvolvimento".

Aos colegas de pós-graduação, pela apoio e troca de idéias, e funcionários de atividades de campo que contribuíram com essa pesquisa: Ingrid, Tomaz, Iuriane, Juliana Rabelo, Juliana Lopes, Cayo, Fernando, Pedro, Antônio, Peter, Uilson e demais.

RESUMO

O carste epigênico em rochas carbonáticas comumente resulta na dissolução quimica por ação de águas meteóricas ao longo do tempo. A geração da porosidade e permeabilidade secundárias contribuem para a dissolução dos carbonatos em reservatórios de petróleo e aquíferos. Esses dois fatores podem impactar a capacidade de armazenamento do reservatório e o fluxo de fluidos. O presente estudo investiga (1) o controle das descontinuidades estruturais (estilólitos verticais e fraturas) e descontinuidades sedimentares (estilólitos horizontais, estratificações cruzada e plano-paralelas) na geração de cavidades de dissoluções cársticas, da microescala (10^2 - 10^{10}µm) a mesoescala (0,1 - 5 m), e (2) a relação das porosidades formadas por processos diagenéticos e seu impacto na geração de carste epigênico da Formação Jandaíra, Bacia Potiguar, Brasil. O estudo apresenta-se em análise de campo de micro a mesoescala baseado em imagens de drone, perfis estratigráficos, dados estruturais e de resistência de rochas coletados pelo martelo de Schmidt. Os estudos de laboratório concentraram-se em imagens microtomográficas, petrografia e petrofísica. Os resultados mostram que os estilólitos verticais podem ser conectados pela percolação de águas meteóricas até formarem um sistema de canal único que corta todas as camadas. Os estilólitos paralelos ao acamamento se encontram nos limites das camadas e, portanto, podem atuar como condutos horizontais de fluidos, formando porosidade em canal. A dissolução ocorre em todas as etapas diagenéticas na matriz, grãos e cimentos da rocha carbonática. A telodiagênese é a etapa mais importante na geração de porosidade secundária devido à mais recente exposição aérea. A telodiagênese gerou diferentes tipos de porosidade devido à dissolução de diferentes feições diagenéticas anteriores, como a cimentação, dolomitas e estilólitos. A dissolução também atuou em descontinuidades preexistentes, como estilólitos, fraturas e superfícies estratigráficas. Em sistemas cársticos epigênicos, altas porcentagens de microporosidade são comumente devido às porosidades móldicas, intrapartícula e intercristais. Tais porosidades podem ser conectadas a fraturas, veios e estilólitos em microescala, aumentando ainda mais a porosidade e a permeabilidade geral da rocha.

Palavras-chave: Carste; reservatório; dissolução; diagênese; estilólito; fratura

ABSTRACT

Epigenic karst in carbonate rocks commonly results in progressive dissolution by the action of meteoric waters over time. The generation of secondary porosity and permeability allows for the dissolution of carbonates in geofluid reservoirs. These two factors can impact reservoir storage capacity and fluid flow. The present study investigates (1) the control of structural discontinuities (tectonic stylolites and fractures) and sedimentary discontinuities (stylolites generated by diagenesis, cross-bedding, and plane-parallel) in the generation of karst dissolution cavities, from microscale (10^2 - 10^{10}µm) to mesoscale (0.1 - 5 m), and (2) the relationship of porosities formed by diagenetic processes and their impact on the generation of epigenic karst from the Jandaíra Formation, Potiguar Basin, Brazil. The study is based on micro to mesoscale analysis based on field analysis based on drone images, stratigraphic logs, structural and rock strength data collected by Schmidt's hammer. Laboratory studies focused on microtomographic images, petrography and petrophysics. . The results show that the stratabound and non-stratabound bed-perpendicular stylolites can be enlarged due to the percolation of meteoric waters until they merge and form a single channel system that cuts all the layers. The bed-parallel stylolites are at the limits of the layers and, therefore, can act as horizontal fluid conduits when well dissolved and forming channel porosity. Dissolution can occur in all diagenetic stages the carbonate rock matrix. Telodiagenesis, is the most important due to the most recent aerial exposure. The dissolution in telodiagenesis generated different types of porosity due to the dissolution of various diagenetic features previously formed, such as cementation, dolomitization, and compaction. Dissolution is also localized to preexisting discontinuities such as stylolites, fractures, and bedding surfaces. In epigenic karst systems, high percentages of microporosity are commonly due to mold, intragrain/intrafossil, and intercrystal porosities. Such porosities can be connected to microscale fractures, veins, and stylolites, further increasing the porosity and overall permeability of the rock.

Keywords: karst; reservoir; dissolution; diagenesis; stylolite; fracture

SUMÁRIO

ÍNDICE DE FIGURAS

ÍNDICE DE TABELAS

1. INTRODUÇÃO

1.1 Apresentação

Este trabalho constitui parte da tese de doutorado do Programa de Pós-Graduação em Geodinâmica e Geofísica (PPGG) da Universidade Federal do Rio Grande do Norte (UFRN). A presente pesquisa discute uma abordagem multidisciplinar e multiescalar, partindo da escala microscópica (tomografia e lâmina delgada) para a mesoscópica (escala de afloramento), para explicar a origem, evolução e ocorrência da carstificação epigênica.

Dois pontos principais são investigados nessa pesquisa. O primeiro é relativo às descontinuidades estruturais e sedimentares que controlam a dissolução de cavidades e geração de carste nas rochas carbonáticas da Formação Jandaíra. Pretende-se entender a importância das fraturas, estilólitos e estratificações no processo da carstificação e sua implicação para o desenvolvimento da porosidade e da permeabilidade. O segundo ponto é relativo aos controles diagenéticos responsáveis pela formação e desenvolvimento de porosidade nas mesmas rochas. Busca-se, nesse ponto, compreender a distribuição e concentração da carstificação nos depósitos sedimentares estudados e associados às diferentes origens e tipos de porosidade.

A região de Lajedo Soledade, área de estudo dessa tese, está localizada em Soledade, distrito de Apodi (RN), no sudoeste da Bacia Potiguar (Fig. 1.1). Esta área possui a maior ocorrência de rochas carbonáticas da seção inferior da Formação Jandaíra e exibe diversas feições cársticas, cujas exposições ocorrem em forma de lajedos e cavernas, além de ser uma região de fácil acesso ao estudo de análogos de reservatórios carbonáticos. A área apresenta vestígios arqueológicos, tais como fragmentos cerâmicos, material da fase da pedra polida, pinturas rupestres e vestígios paleontológicos, que incluem restos de vertebrados quaternários e fósseis da fauna marinha cretácea. As áreas de maior interesse paleontológico e arqueológico são protegidas pela Fundação Amigos do Lajedo de Soledade, além do envolvimento da comunidade local. O lajedo apresenta diversas falhas e fraturas de direção preferencial NE/SW e NW/SE, que permitiram o desenvolvimento de ravinas e pequenas cavernas a partir do intenso processo de carstificação. As áreas de maior interesse paleontológico e arqueológico são protegidas e a preservação do Lajedo é assegurada pela Fundação Amigos do Lajedo de Soledade e pelo envolvimento da comunidade local.

A presente tese é parte do Projeto FUNPEC/UFRN/SHELL/POROCARSTE 3D, financiado pela Shell e executado pela UFRN, sob a coordenação do Prof. Dr. Francisco Hilario Rego Bezerra (DG-UFRN). Também contou com o apoio do Laboratório de

Engenharia de Reservatórios de Petróleo (LABRES, Universidade Federal do Rio Grande do Norte-UFRN, coordenado pelo professor Marcos Allyson Rodrigues) e do Laboratório de Tomografia Computadorizada de Raios-X (Departamento de Energia Nuclear (DEN), Universidade Federal de Pernambuco-UFPE, coordenado pelo professor Antônio Celso Dantas Antonino).

1.2 Estrutura da tese

No escopo desta tese de Doutorado estão inseridos dois artigos científicos: um já publicado e outro submetido a uma revista científica internacional, em conformidade com as normas internas do PPGG/UFRN. A tese está estruturada em cinco capítulos. O Capítulo 1 traz um contexto geralsobre o trabalho, com objetivos, justificativas e localização da área de estudo. No Capítulo 2 é abordada a caracterização litoestratigráfica da Formação Jandaíra e seu carste epigênico. O Capítulo 3 discorre sobre as feições que definem e determinam a ocorrência e distribuição observadas na diagênese em rochas carbonáticas, importantes para concentração de dissolução cárstica em reservatórios carbonáticos.

Ambos os artigos foram submetidos ao Journal of Marine and Petroleum Geology e serão apresentados nos capítulos 4 e 5. O primeiro artigo, intitulado "*Structural and sedimentary discontinuities control the generation of karst dissolution cavities in a carbonate sequence, Potiguar Basin, Brazil*", aborda o comportamento das fraturas e estilólitos que se limitam no contato das camadas (*stratabound*) ou não se limitam aos contatos das camadas (*non-stratabound*), como também as suas relações com as estratificações planares e cruzadas que podem ser alargadas devido a percolação de águas meteóricas. O segundo artigo submetido, intitulado "Pore network characteristics as a function of diagenesis: Implications for epigenic karstification in shallow-water carbonates" descreve como os diferentes tipos de feições diagenéticas podem impactar no desenvolvimento da porosidade e formação de carste em análogos de reservatórios carbonáticos. O Capítulo 6 apresenta as principais conclusões da tese e as considerações finais. As referências estão localizadas no final da tese.

1.3 Objetivos e justificativas

Esse estudo foca nos carbonatos de águas rasas do Cretáceo da Formação Jandaíra, Bacia Potiguar. As rochas da Formação Jandaíra, na área de Lajedo Soledade, foram selecionadas para estudo por ser uma região de fácil acesso e considerada como análoga a reservatórios carbonáticos (e.g., Carlotto et al., 2017; Chafetz et al., 2018; Goldberg et al., 2017; Herlinger, Zambonato & De Ros, 2017). Esses afloramentos mostram cavidades resultantes do intenso processo de dissolução cárstica, cuja dimensão varia de milímetros a dezenas de metros ao longo de superfícies sedimentares, estilólitos e fraturas. Essas feições cársticas exibem padrões horizontais e verticais. O estudo desses análogos de reservatório é importante, uma vez que muitas feições (poros vugulares, estratificações, fraturas e estilólitos) estão abaixo da resolução das técnicas sísmicas e de dados de radar de penetração (*Ground Penetrating Radar – GPR*) e, consequentemente, são detectáveis apenas em análises microscópicas. A dissolução cárstica apresenta-se de diferentes formas e tamanhos, como vugs, canais e cavernas (Choquette & Pray, 1970) em reservatórios, mas poucos estudos abordam os fatores que controlam sua distribuição espacial ainda são raros. Poucos estudos explicam como os processos diagenéticos, da eodiagênese à telodiagênese, podem controlar a formação, desenvolvimento progressivo e distribuição espacial dos sistemas cársticos epigênicos de micro a macroescala (p. ex., Hajikazemi et al., 2010; Wang & Al-Aasm, 2002).

O objetivo desse estudo é analisar as descontinuidades estruturais (fraturas e estilólitos verticais) e sedimentares (estilólitos horizontais, estratificações planares e cruzadas), como também os componentes das rochas carbonáticas (grãos, matriz e cimento) que influenciam na geração e desenvolvimento da dissolução cárstica epigênica. Todas as descontinuidades e componentes das rochas foram examinadas no campo e em laboratório através de análises petrográficas, petrofísicas e análises de imagens de drone e tomografia. Com esses dados é possível explicar o controle e distribuição espacial do carste epigênico desde a escala de afloramento (imagens de drone) à escala microscópica, mostrando como ocorre o desenvolvimento das dissoluções cársticas do ponto de vista evolutivo diagenético.

Novos desafios em reservatórios carbonáticos carstificados e fraturados requerem a integração desses dados uma vez que a presença de carstes afeta a circulação do fluido, pode gerar colapso das colunas de poços de perfuração e modificar a porosidade/permeabilidade do reservatório durante a perfuração (por exemplo, Aquilina et al., 2003; Klimchouk & Ford, 2000; Li et al., 2017; Youssef & Awotunde, 2019). O estudo de afloramentos carbonáticos análogos a reservatórios petrolíferos são frequentemente empregados para reduzir as incertezas associadas a caracterização e modelagem de reservatórios (p.ex., Agosta et al., 2010; Giuffrida et al., 2020, 2019; La Bruna et al., 2018, 2017; Lamarche et al., 2012; Rustichelli et al., 2013).

1.4 Localização da área de estudo

A região de estudo está localizada na porção sudoeste do estado do Rio Grande do Norte, no município de Apodi (Fig. 1.1), onde ocorrem excelentes exposições de rochas carbonáticas fraturadas e carstificadas da Formação Jandaíra (Bacia Potiguar). O Lajedo de Soledade, um dos sítios arqueológicos mais importantes do Brasil, está localizado a 12 km do centro da cidade de Apodi.

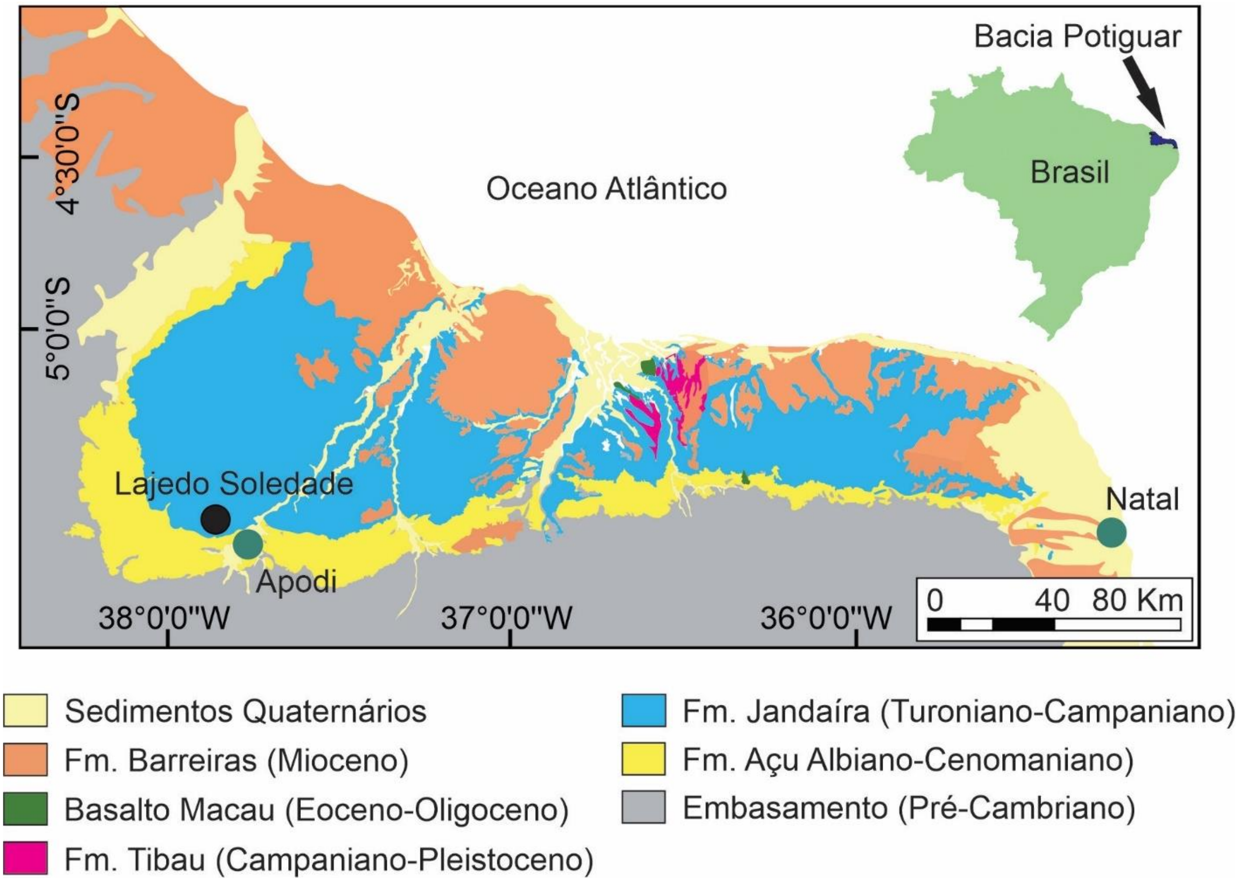

Fig. 1.1 - Mapa geológico simplificado da Bacia Potiguar e localização da área de estudo. Base de dados: Serviço Geológico do Brasil (Angelim et al., 2006).

1.5 Base de dados

Para a realização desse estudo, foram utilizados dados de diferentes naturezas e escalas,desde dados de imagens de VANT, dados estruturais e estratigráficos, dados de resistência à compressão uniaxial, coletados em campo; e dados petrográficos e petrofísicos adquiridos a partir da preparação e processamento de amostras de plugs. Abaixo segue uma breve descrição dos dados utilizados. Os detalhes de cada método estão melhor apresentados nas duas publicações, nos Capítulo 4 e 5.

1.6 Imagens de VANT

Foram elaborados dois modelos digitais diferentes do afloramento no Lajedo Soledade. O primeiro consiste em um modelo de 420 m x 680 m, obtido a partir de imagem de VANT (Phatom 4 pro–DJI) a uma altura de aproximadamente 15 m da superfície do afloramento, com resolução espacial de 4 cm/pixel. O segundo modelo se refere a uma parede vertical de 3m de altura x 14,5 cm de largura (Fig. 1.2). As imagens de VANT foram adquiridas e processadas durante as atividades de campo e tiveram cobertura ortofotogramétrica de 80%. As imagens foram processadas no *software* Agisoft Photoscan Professional, usando os pontos adquiridos em voos e uma base geodésica local.

Fig. 1.2 - Exemplo de imagem de VANT adquirida e processada durante e após atividades de campo.

1.7 Dados de Campo

Nessa etapa foram analisados 6 paredes verticais naturais, localizados no Lajedo Soledade (RN), que são orientados NNW-SSE e ENE-WSW, onde foram levantadas seções colunares (Fig. 1.3). Caracterizações preliminares de superfícies de acamamento, litologias, estruturas sedimentares e evidências de dissolução cárstica foram acompanhados pela coleta de amostras (plugs) de aproximadamente 4 cm de altura x 2,5 cm de diâmetro. Foram coletadas 58 amostras paralelas e 49 amostras perpendiculares ao acamamento para o estudo petrográficos e caracterizações petrofísicas. Optamos por coletar as amostras que não mostram poros vísiveis a olho nu, como vugs e canais para manter um padrão da escala de poros analisada (µm) e evitar quebra dos plugs durante pressão para cálculos de porosidade e permeabilidade.

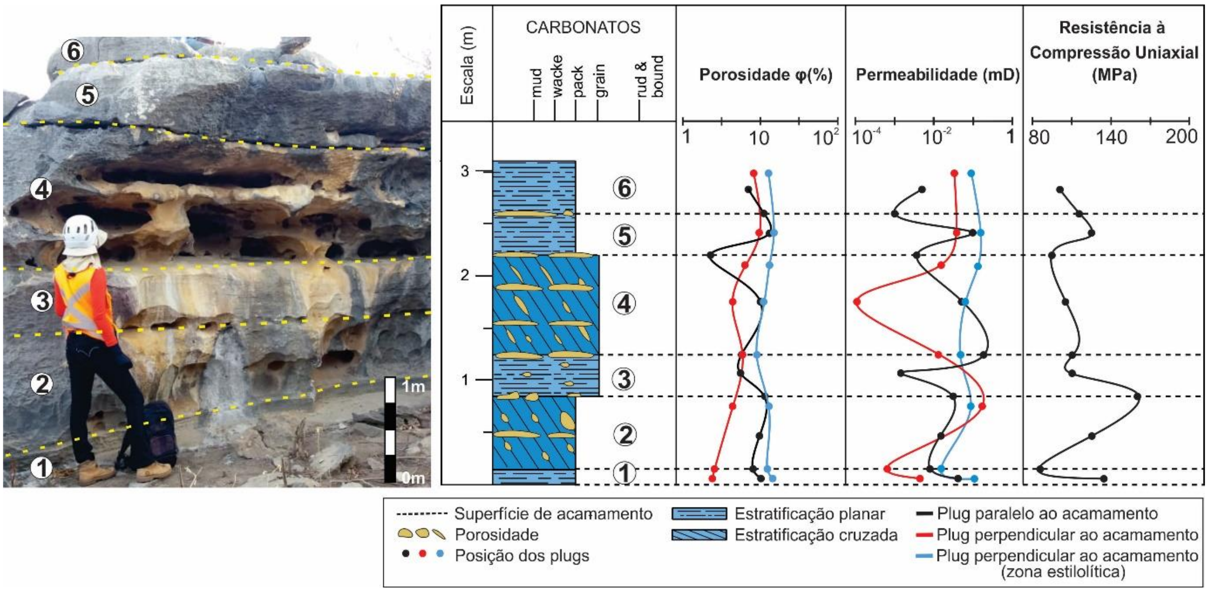

Fig. 1.3 - Exemplo de confecção de seção colunar com correlação de porosidade, permeabilidade e martelo de Schmidt.

Nessas paredes verticais também foram feitas análises estruturais qualitativas em fraturas e estilólitos a fim de caracterizar a geometria, orientação, estrutura interna, preenchimento de material, etc. Além disso, as propriedades mecânicas atuais das rochas carbonáticas, como à resistência a compressão uniaxial (*Uniaxial Compressive Strenghts – UCS*) foram estimadas seguindo os procedimentos publicados (p. ex., Aydin, 2008; Aydin & Basu, 2005; Zoback, 2007) usando o teste de dureza do rebote do martelo de Schmidt (Fig. 1.4).

Fig. 1.4 - Martelo de Schmidit para teste de dureza das rochas.

1.8 Dados de Laboratório - Preparo, análise e descrição das amostras de plug

Com as amostras de plug foram confeccionadas 119 lâminas petrográficas. As descrições e análises petrográficas foram realizadas usando um microscópio óptico Olympus BX41 polarizado localizado na UFRN. Com a catodoluminescência acoplada a um microscópio Zeiss Scope A1, realizada na UNESP, foram coletadas imagens por uma câmera colorida Zeiss Axiocam 705 e processadas pelo *software* Zeiss Zen 3.3 lite pela UFRJ. Imagens de Microscópio Eletrônico de Varredura (MEV) foram coletadas no CTGAS (Senai RN). Análises petrofísicas de laboratório foram realizadas no Laboratório de

Engenharia de Reservatórios de Petróleo (LABRES) do Departamento de Engenharia de Petróleo da Universidade Federal do Rio Grande do Norte (DPET / UFRN), Natal-RN. As 107 amostras de plug foram aplanadas pelo técnico de laboratório antes de serem analisadas no equipamento Coreval 700 (Fig. 1.5A), para extração de dados de porosidade e permeabilidade em gás N_2 a 1000 psi. As imagens de tomografia computadorizada foram adquiridas em 20 plugs digitalizados (Fig. 1.5B) pelo Laboratório de Tomografia Computadorizada de Raios-X no Departamento de Energia Nuclear na UFPE. Todas as reconstruções de imagens foram feitas pelo *software* CT Pro 3D. Os *softwares* ImageJ e 3Dslicer foram responsáveis pelo processamento e análise digital das imagens. Os dados relativos a porosidade total, conectada e isoladas das imagens de tomografia foram computados para gerar gráficos através do *software* Origin 6.1.

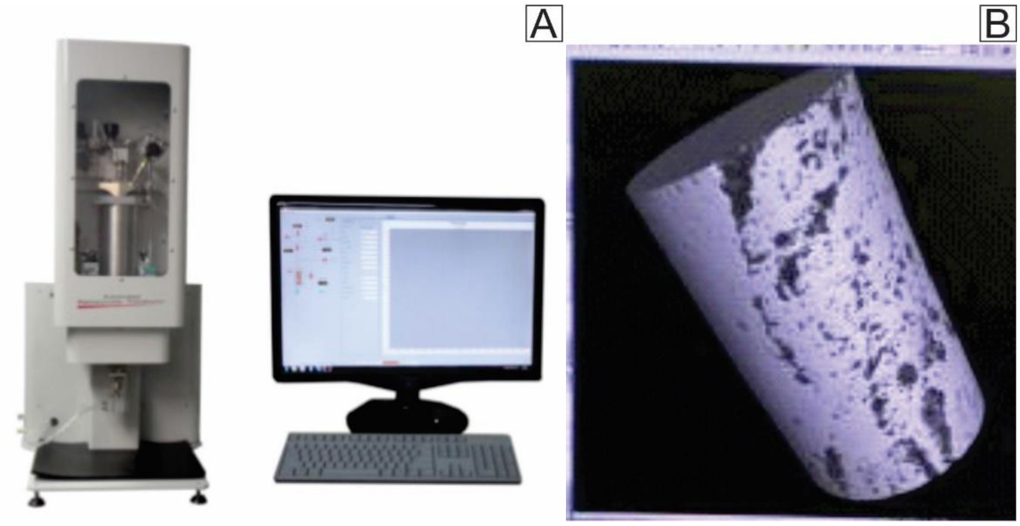

Fig. 1.5 - (A) Equipamento Coreval 700 responsável pelos dados de porosidade e permeabilidade em amostras plugs, (B) imagem de tomografia de plug.

2. A FORMAÇÃO JANDAÍRA E O CARSTE EPIGÊNICO

2.1 Formação jandaíra

A Formação Jandaíra faz parte de uma sequência sedimentar drifte e consiste em rochas carbonáticas que tiveram a sua deposição em águas rasas entre o Turoniano e Campaniano (Cretáceo Superior) (Pessoa Neto et al., 2007). Representam a implantação do sistema marinho após a separação dos continentes sul-americano e africano associado à abertura do Atlântico Sul (Matos, 1992; Pessoa Neto et al., 2007). Essas rochas apresentam-se na forma de extenso planalto, na porção emergente da Bacia Potiguar, e são intensamente erodidas e carstificadas, com suave mergulho para nordeste em direção ao Oceano Atlântico (Pessoa Neto et al., 2007). As rochas desta unidade litoestratrigráfica apresentam espessura máxima de 600 m, distribuídas na porção emersa e submersa da Bacia, com mergulho regional para N-NE.

As rochas da Formação Jandaíra encontram-se acima das rochas siliciclásticas da Formação Açu. Na porção emersa da Bacia, apresenta-se parcialmente recoberta por rochas siliciclásticas da Formação Barreiras e na porção submersa, encontra-se recoberta por rochas carbonáticas e siliciclásticas das formações Ubarana, Tibau e Guamaré (Pessoa Neto et al., 2007)

As rochas carbonáticas da Formação Jandaíra foram depositadas, inicialmente, através de uma transição com os sedimentos estuarinos da Formação Açu. O clima árido e a transgressão do Neocenomaniano favoreceram a diminuição gradual do influxo de terrígenos na bacia e o acréscimo da produtividade carbonática em águas rasas (Garcia, 2014).

Os sedimentos carbonáticos foram depositados em ambiente marinho-plataformal, em forma de uma rampa carbonática, em profundidades de água inferiores a 50 m de acordo com as assembléias de biotas (por exemplo, ostracodes, algas verdes/vermelhas, foraminíferos planctônicos e bentônicos e equinodermas) (Tibana & Terra, 1981). As fácies carbonáticas dominantes são: (1) packstones bioclásticos para wackestones, que registram um sistema marinho com baixo consumo de água e; (2) grainstones bioclásticos a packstones, que indicam um sistema marinho raso com maior energia hídrica (Santos Filho et al., 2015). Rochas híbridas carbonato-siliciclásticas também são identificadas, especialmente próximas ao limite de contato da Formação Açu (Tibana & Terra, 1981).

A rampa carbonática da Formação Jandaíra foi submetida, durante e após sua deposição,a vários eventos de soerguimento, relacionados a dois importantes campos de tensão pós-rifte na Bacia Potiguar (Bezerra et al., 2008; Bezerra and Vita-Finzi, 2000).

O primeiro campo de tensão ocorreu no Cretáceo Superior ao Mioceno Médio (Fig. 2.1A) e compreende uma compressão sub-horizontal máxima orientada a N-S e uma extensão orientada para E-W (Bezerra et al., 2020). Esse evento ocasionou as fraturas N-S preenchidas com veios de calcita e estilólitos tectônicos de direção E-W, distribuídos regionalmente ao longo da Bacia Potiguar (Bertotti et al., 2017; Bezerra et al., 2020; de Graaf et al., 2017). Durante esse período, rochas cristalinas da Província Borborema oriental sofreram resfriamento crustal, registrados por traços em fissão de apatita, sinalizando soerguimento e denudação, entre o Maastrichtiano-Paleoceno (Morais Neto et al., 2009).

O segundo campo de tensão, do Mioceno Médio até os dias atuais (Fig. 2.1B e C), inclui compressão sub-horizontal E-W a NW-SE combinada com extensão sub-horizontal

N-S e NE-SW (Bezerra et al., 2020). Esse evento causou a reativação e inversão de falhas NE-SW do rifte, com dobramento e fraturamento associado (Bagni et al., 2020; Bezerra et al., 2020; Bezerra and Vita-Finzi, 2000; Hackspacher et al., 1985; Morais Neto et al., 2000).

Ambos os campos de tensão reativaram falhas geradas na fase rifte. A deformação pós-rifte ocasionou falhas com rejeitos verticais de dezenas de metros na Formação Jandaíra, no entanto, essa deformação não foi tão intensa quanto os rejeitos verticais observados nas unidades de rifte, que somam 6 km (Bezerra et al., 2020; Silva et al., 2017).

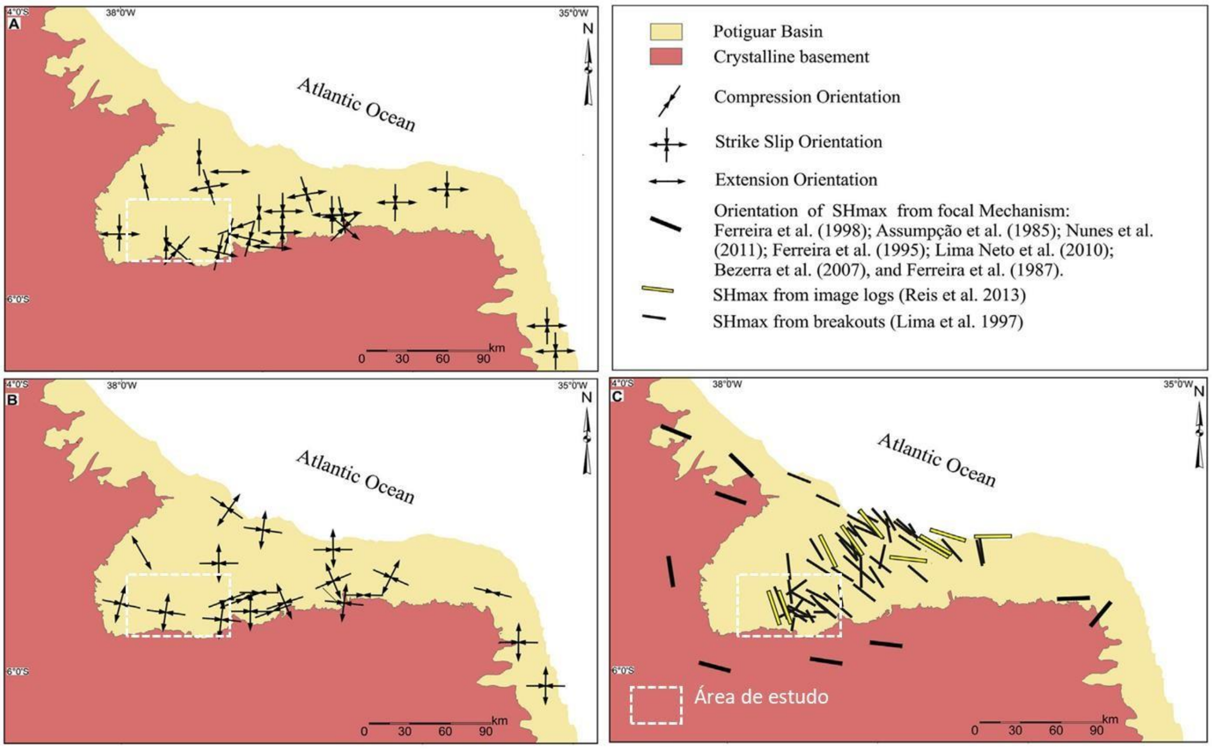

Fig. 2.1 - Mapas simplificados dos três campos de tensão, destacando as direções de máxima compressão horizontal e extensão e cinemática das falhas: A) Campo de tensão 1; B) Campo de tensão 2; e C) Campo de tensão atual. Retirado de Bezerra et al., 2020.

2.2 Carste epigênico

Carste é um termo com sentido amplo que inclue todas as feições diagenéticas de superfície e subsuperfície tanto em escala microscópica quanto macróscopica que são geradas durante a dissolução química (James and Choquette, 1988) e precipitação química, como estalactites e estalagmites. Esse termo representa um tipo de relevo geológico com hidrogeologia diversa que resulta de uma associação de rochas com alta solubilidade e porosidade secundária (fraturas) bem avançada (Ford & Williams, 2007). A paisagem cárstica é caracterizada por superfícies acidentadas dominadas por depressões locais, paredões rochosos, drenagens subterrâneas e cavernas (Monroe, 1970), como também por blocos colapsados e torres cásticas, (Ford & Williams, 2007; Goldscheider and Drew, 2007). Em uma visão geomorfológica, há vários constituintes de um sistema cárstico (Fig. 2.2), tanto em relação aos processos e componentes da paisagem quanto a complexidade gerada pela dissolução de carbonatos na zona de erosão e a região de deposição (Ford, 1988).

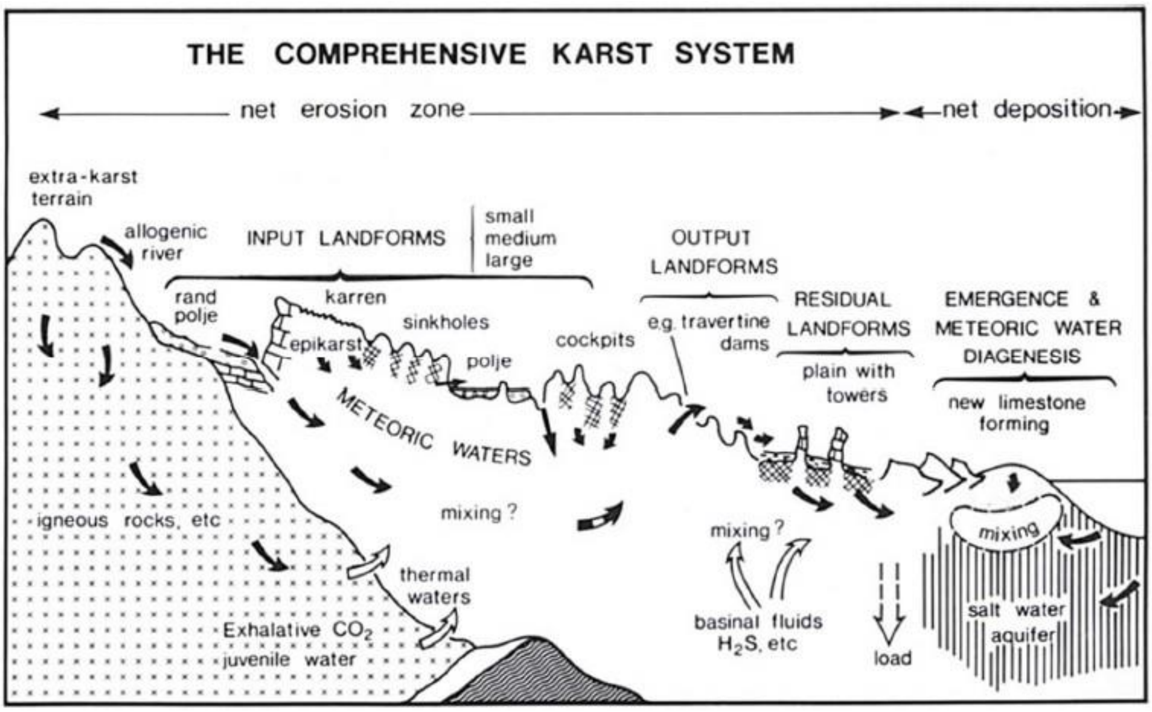

Fig. 2.2 - Diagrama com os principais constituintes do sistema cárstico. Retirado de Ford (1988).

A presença de descontinuidades estruturais e sedimentares (Araújo et al., 2021) e a influência da diagênese pode controlar o estilo de carstificação, gerando condutos, poros e/ou alargamento dos poros preexistentes nas rochas. A carstificação pode ser: (1) epigênica, quando a dissolução das rochas ocorre mediante o escoamento descendente de águas meteóricas (p.ex., Heward et al., 2000; Vacher & Mylroie, 2002; Weidlich, 2010; White, 1977); e (2) hipogênica, quando a dissolução é originada por fluxo ascendente de águas subterrâneas (p. ex., Cazarin et al., 2019; Ford & Williams, 2013; Klimchouk et al., 2017; Mádl-Szőnyi et al., 2017). Há também carstificação em contexto epigênico e hipogênico ao mesmo tempo (p.ex., Gutiérrez et al., 2019; Rajaram et al., 2009; Stafford et al., 2008; Upchurch et al., 2019).

A carstificação epigênica (Fig. 2.3) é gerada pela reação química das águas meteóricas com o dióxido de carbono (CO_2) presente na atmosfera e solo (Palmer, 1991). Essa reação propicia a dissolução química das rochas devido a formação de ácido carbônico (H_2CO_3) ou água ácida (Ford & Williams, 2007), sendo o causador da dissolução ácida da calcita. As principais reações que ocorrem na carstificação são:

(1) Geração do ácido carbônico: H2O + CO2 → H2CO3

(2) Dissolução da calcita: CaCO3 + H2CO3 → Ca2+ + 2HCO3-

(3) Precipitação da calcita: $Ca^{2+} + 2HCO_3^- \rightarrow CaCO_3 + CO_2 + H_2O$

A geração de ácido carbônico evoluiu no tempo e no espaço, alargando fraturas preexistentes e gerando condutos e cavernas (Goldscheider & Drew, 2007). Muitos fatores podem interferir na evolução cárstica, desde fatores climáticos (p.ex., quantidade de chuva), circulação de fluidos e composição mineralógica e geoquímica da rocha, até estruturas regionais (Ford & Williams, 2007; Goldscheider & Drew, 2007). As rochas carbonáticas (calcários, dolomitos e mármores) que possuem como mineral principal a calcita ($CaCO_3$) ou dolomita ($CaMg(CO_3)_2$) apresentam íons dissociados de Ca^{2+} e CO_3^{2-} em um sistema hidrogeológico. Como a solubilidade da calcita é maior do que a solubilidade da dolomita, os calcários tendem a ser mais solúveis que dolomitos.

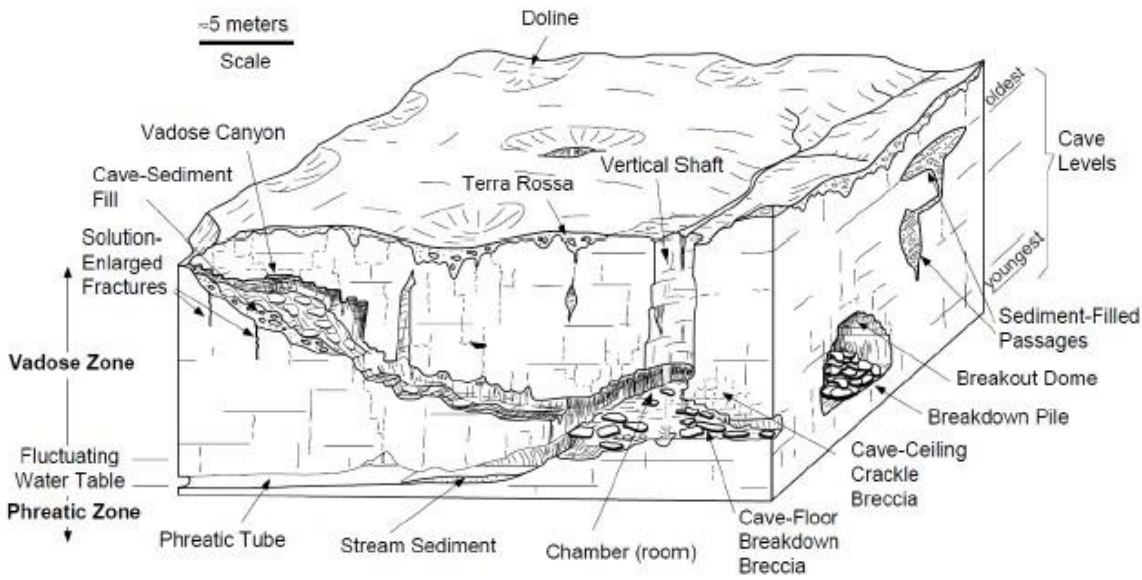

Fig. 2.3 - Bloco diagrama do sistema cárstico epigênico. Retirado e modificado de Loucks & Handford (1992).

A carstificação epigênica da Formação Jandaíra respeita descontinuidades sedimentares e estruturais, sendo esta última relacionada a tensores tectônicos que atuaram após sua deposição. Vários trabalhos investigaram a importância das fraturas na formação e evolução do carste epigênico na Formação Jandaíra (Araújo et al., 2021; Bagni et al., 2020; Bertotti et al., 2017; Carneiro et al., 2015; de Graaf et al., 2017; Fernandes et al., 2015; Menezes et al., 2020; Rabelo et al., 2020, 2015; Silva et al., 2017; Xavier Neto & Medeiros, 2006). No entanto, poucos trabalhos apontam a relação do carste com a estratigrafia e sedimentologia no controle do carste (Fig. 2.4). Diferentes formas de relevo cárstico foram relacionados com sistemas de fraturas, estratificações sedimentares e processos fluviais (Silva et al., 2017). Descontinuidades sedimentares, como as estratificações plano-paralelas e cruzadas também atuam na dissolução e geração do carste (Araújo et al., 2021). Um estudo detalhado da parassequência diagenética dos carbonatos da Formação Jandaíra foi proposto por Bagni et al. (2022) com o objetivo de compreender a superposição de eventos geológicos, o desenvolvimento de dissolução cárstica e a concentração de cavernas. O principal resultado desse trabalho foi mostrar que as cavernas e grandes corredores de permeabilidade ocorrem principalmente abaixo das discordâncias regionais subaéreas e ao longo do vale do Rio Apodi. No entanto, é necessário estudos mais detalhados quanto a distribuição espacial e geometria dos poros em 3D e sua relação na formação do carste.

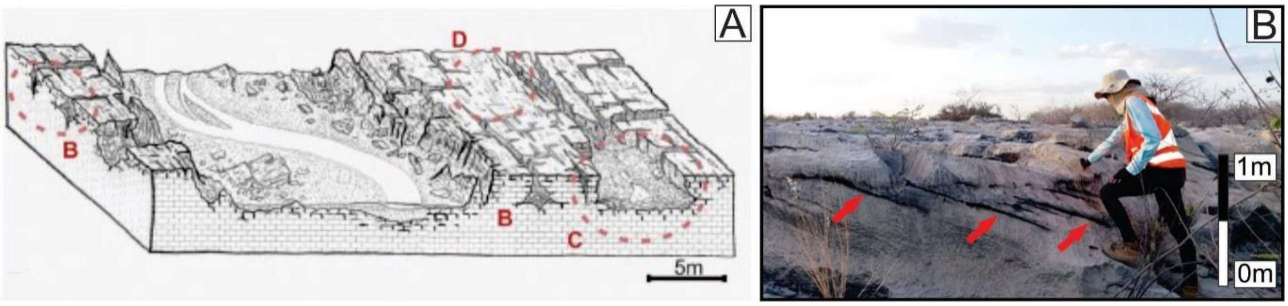

Fig. 2.4 - (A) Esquema do vale do rio Apodi-Mossoró, apresentando fraturas, drenagem e feições cársticas associadas (retirado de Silva et al., 2017); (B) Carste ao longo de estratificação cruzada (retirado de Araújo et al., 2021).

3. DIAGÊNESE

3.1 Introdução

Os primeiros estudos sobre diagênese, em rochas sedimentares, adquiriram notoriedade no final da década de 50 (p. ex., Fairbridge, 1967; Friedman, 1964; Sujkowski, 1958). Estudos anteriores a década de 80 (Hayer, 1979; Heald and Larese, 1973; McBride, 1977; Schmidt and McDonald, 1979) já sugeriram que os processos responsáveis pela geração de porosidade secundária, característico da diagênese, são provocados por influxo de água meteórica, que fornecem a lixiviação (Bloch, 1994). A porosidade e permeabilidade são elementos importantes, pois armazenam e transportam fluidos na rocha. Mudanças nessas propriedades devido à diagênese podem impactar a heterogeneidade e qualidade de reservatórios (Wilson & Stanton, 1994).

A diagênese compreende processos físicos, químicos e biológicos que ocorrem em diversos ambientes, tanto em arenitos quanto em carbonatos e as assembléias minerais juntamente com as águas dos poros reagem para alcançar um equilíbrio textural e geoquímico em condições pós-deposicionais (Choquette & Pray, 1970; Schmidt & Mcdonald, 1979), excluindo processos envolvendo temperaturas e pressões altas o suficiente para serem chamados de metamorfismo. A diagênese impacta na porosidade e permeabilidade deposicionais ou primárias, devido ao contexto do ambiente deposicional, diminuindo ou aumentando seus volumes em relação a rocha total (Byrnes, 1994; Worden & Burley, 2003).

3.2 Diagênese em carbonatos

A diagênese de carbonatos pode ocorrer em muitos ambientes: no ambiente marinho durante a deposição do sedimento, próximo à superfície do sedimento, onde as águas doces penetram nos sedimentos, ou em salmouras do subsolo mais profundo. A diagênese pode ser originada em todos os ambientes acima citados (alteração singenética ou eogenética), continuar com o soterramento profundo (alteração mesogenética) e estender-se à elevação subsequente (alteração telogenética) (Choquette & James, 1987; Choquette & Pray, 1970; James & Choquette, 1984; Scholle & Ulmer-Scholle, 2003). A diagênese pode mascarar informações sobre características primárias, como também a história de configurações pós-deposicionais, composições de água de poro e temperaturas (Scholle & Ulmer-Scholle, 2003).

A diagênese pode diminuir ou aumentar a porosidade e a permeabilidade. No entanto, com tempo prolongado e profundidade de soterramento, a tendência é de perda gradual de porosidade e permeabilidade, e essa mudança é frequentemente significativa (Lucia, 2007; Scholle & Ulmer-Scholle, 2003).

O gráfico abaixo (Fig. 3.1) descreve as porosidades médias altamente generalizadas dos depósitos carbonáticos antigos e atuais, além das rochas "excepcionalmente porosas" dos reservatórios de hidrocarbonetos. A perda de porosidade está ligada a uma série de eventos diagenéticos marinhos, meteóricos e de sepultamento que ocorrem durante as histórias sin e pós-deposição dos estratos (Scholle & Ulmer-Scholle, 2003). Grainstones têm porosidades entre 35% a 45%, enquanto argilitos têm porosidades de aproximadamente 70%. A porosidade da maioria dos carbonatos antigos é < 5%, e as rochas reservatório têm menos da metade da porosidade das rochas carbonáticas atuais.

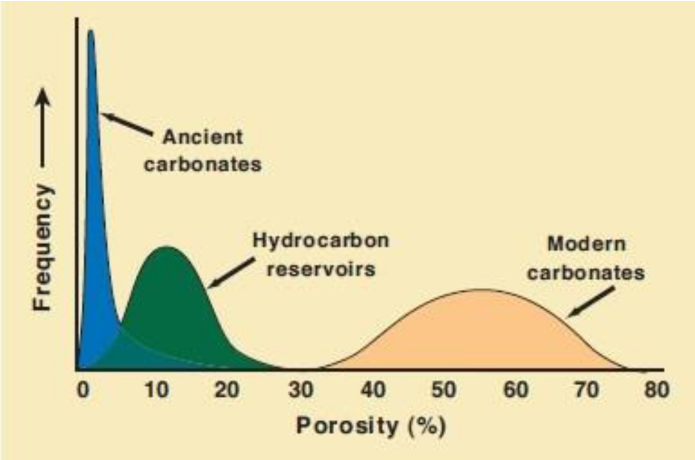

Fig. 3.1 - Diferenças de porosidades médias dos depósitos carbonáticos antigos, atuais e reservatórios de hidrocarbonetos. Retirado de Scholle & Ulmer-Scholle (2003).

A exploração de hidrocarbonetos e depósitos minerais hospedados por carbonato requer um conhecimento dos processos diagenéticos, variáveis que impedem a perda de porosidade e o tempo relativo de migração de óleo x evolução da porosidade.

Os processos diagenéticos podem ser:

1) Cimentação (o enchimento de materiais recentemente precipitados em espaços de poros abertos de origem primária ou secundária);
2) Dissolução (a lixiviação de minerais instáveis formando poros secundários, vugs ou cavernas);
3) Substituição mineral (a substituição de um polimorfo de um mineral por outro);
4) Recristalização (mudanças no tamanho do cristal, estado de deformação ou geometria sem uma mudança na mineralogia) ou recristalização de deformação;

5) Compactação mecânica (incluindo desidratação e deformação ou reorientação de grãos);
6) Compactação química (dissolução principalmente ao longo de superfícies como estilólitos ou dissolução por pressão);
7) Fraturamento.

Para a caracterização de cimentação, Folk (1965) propôs que os cimentos preenchedores de poros são classificados de acordo com seu método de produção (precipitação passiva ou deslocável), formato do cristal e tamanho do cristal (Fig. 3.2).

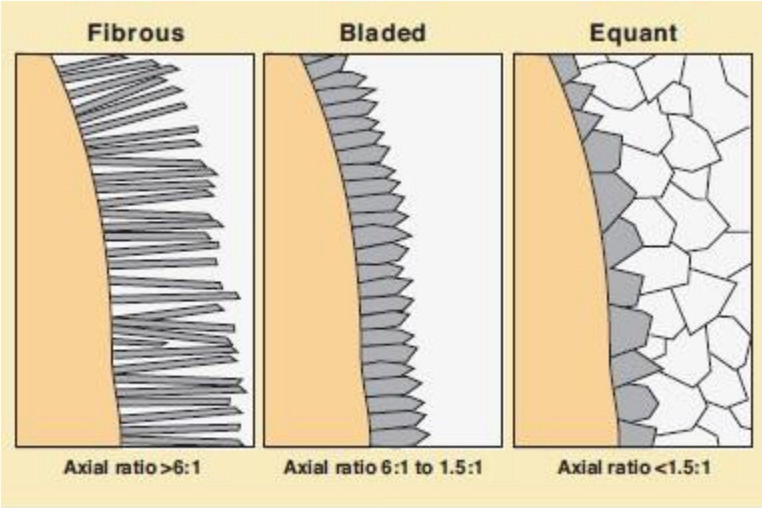

Fig. 3.2 - Classificação da cimentação de acordo com as proporções relativas entre comprimento e largura das formas de cristal de carbonato. Retirado de Scholle & Ulmer-Scholle (2003).

A dissolução acontece quando os fluidos dos poros encontram-se subsaturados com relação a mineralogia do constituinte carbonático. A dissolução pode ocorrer próxima a superfície ou em subsuperfície. Quando ocorre próxima a ambientes meteóricos de superfície, contribui no processo de carstificação com a formação e evolução de vugs, canais e cavernas (Choquette and Pray, 1970). Há diversos tipos de porosidade secundária (Fig. 3.3), conforme classificação de Choquette and Pray (1970). Choquette & Pray (1970) descreveram a "porosidade vuggy" como poros observáveis a olho nu e aparentes em seções finas causadas pela quebra indiscriminada de cimento e grãos.

No entanto, Lucia (2007) propôs uma nova e detalhada classificação de dissolução (Fig. 3.4), afirmando que a trama das rochas e parâmetros petrofísicos devem ser considerados na definição e classificação do espaço dos poros (Lucia, 2007). Para relacionar a trama das rochas carbonáticas com a distribuição de tamanho de poro, é importante determinar se o espaço de poro pertence a uma das três principais classes de tipo de poro:

1) Interpartícula (*interparticle*);

2) Vug-separado (*separate-vug*);
3) Vug-tocante (*touching-vug*).

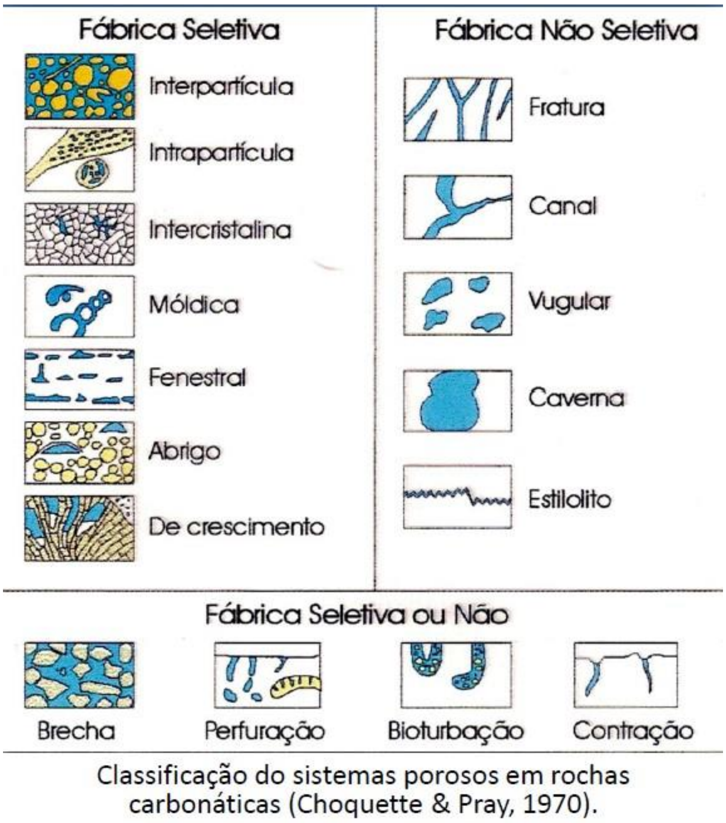

Fig. 3.3 - Classificação de sistemas porosos em rochas carbonáticas. Retirado e modificado de Choquette & Pray (1970).

A porosidade interpartícula altera as características petrofísicas, alterando a maneira como o espaço poroso está conectado, e assim todo o espaço de poro é conectado de alguma forma (Fig. 3.5). Vugs separados são definidos como espaços de poros que estão interconectados apenas por meio de poros interpartículas. Vugs-tocantes são definidos como espaços de poros que formam um sistema de poros interconectado independente do espaço de poros interpartículas (Fig. 3.6).

A compactação é um processo importante que ocorre com o soterramento das rochas, e assim reduzindo sua porosidade, e pode ser de dois tipos: mecânica e química. A compactação mecânica é evidenciada pela rotação, quebra de grãos frágeis e/ou esmagamento de grãos dúcteis (Fig. 3.6).

A compactação química, também chamada de dissolução por pressão, provoca a dissolução a nível de grãos, gerando contatos interpenetrativos do tipo suturado e côncavo-convexo (Fig. 3.7), como também estilólitos. Os grãos se dissolvem em seus contatos devido à pressão de sobrecarga durante o soterramento. Os volumes frequentemente grandes de material podem mais tarde ser precipitados como um cimento em outro lugar no sistema (Boggs, 1992; Tucker, 2001).

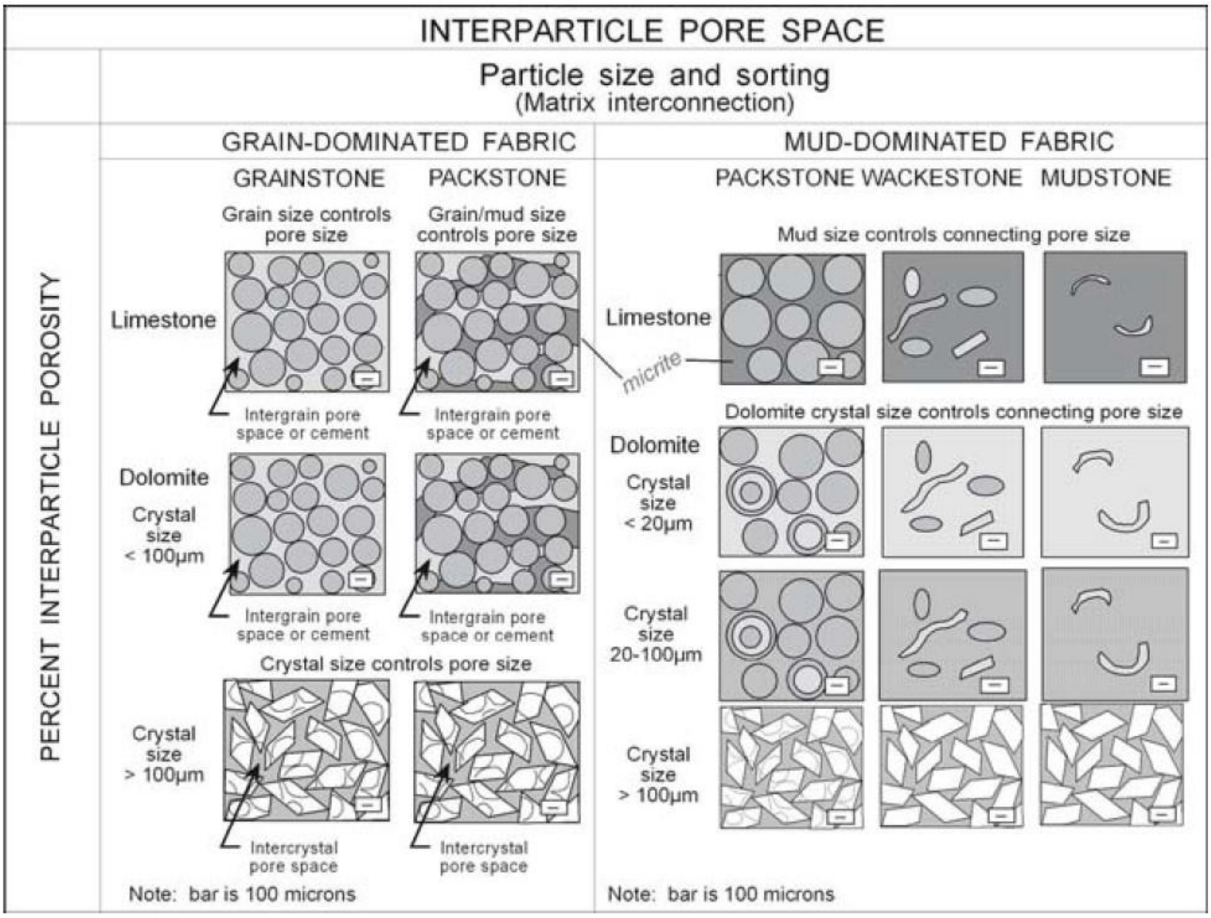

Fig. 3.4 - Classificação geológica/petrofísica da porosidade interpartícula no carbonato com base no tamanho e classificação de grãos e cristais. Retirado de Lucia (2007).

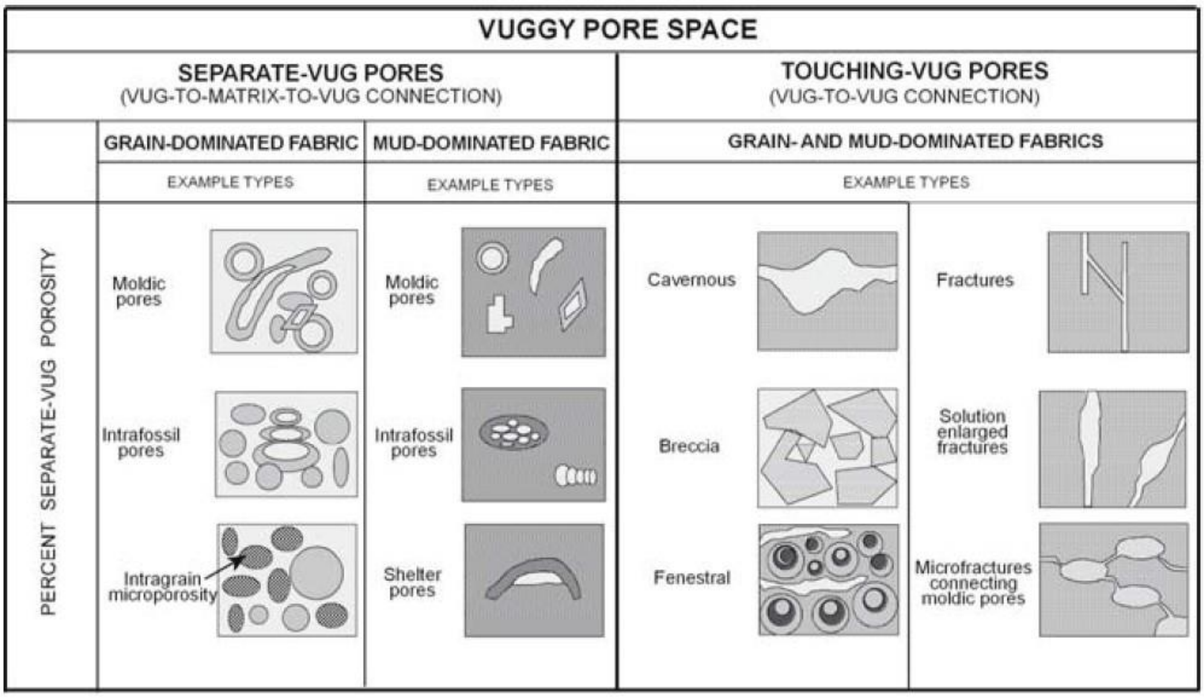

Fig. 3.5 - Classificação geológica/petrofísica da porosidade vug no carbonato com base no tamanho e classificação de grãos e cristais. Retirado de Lucia (2007).

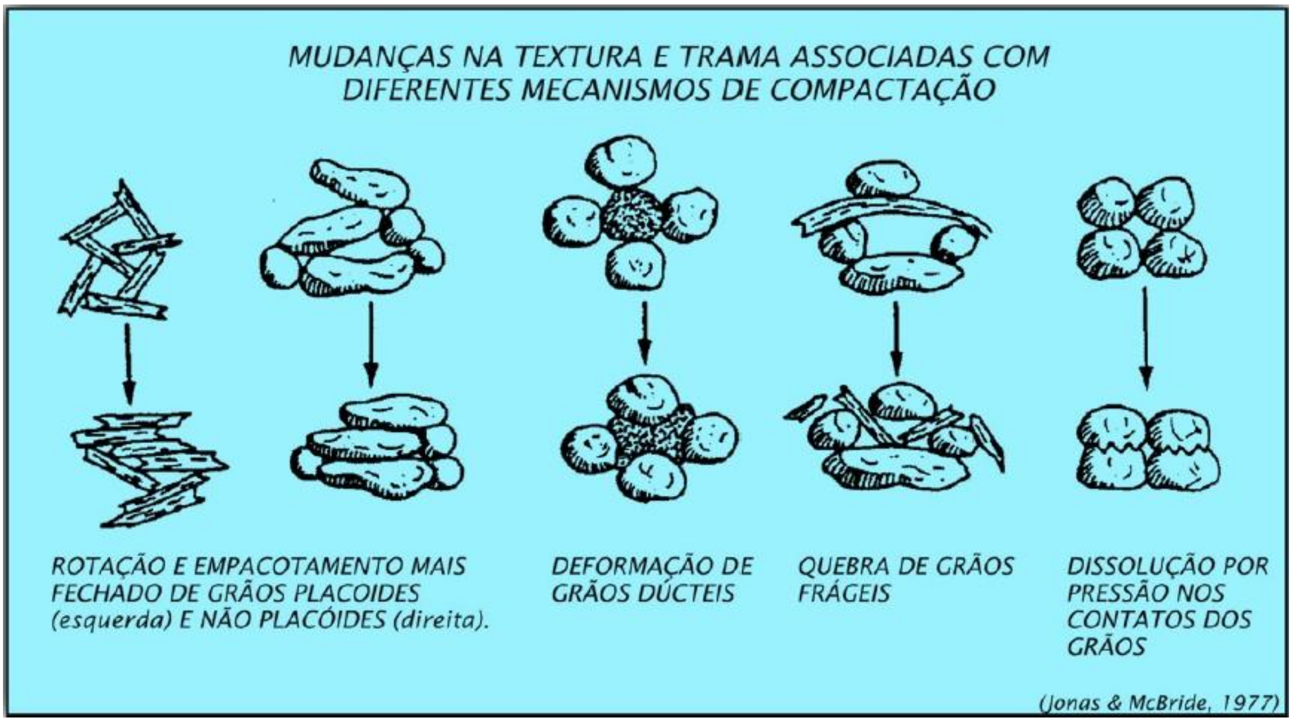

Fig. 3.6 - Diferentes processos de compactação que mudam a textura e trama das rochas. Retirado e modificado de Jonas & McBride (1977).

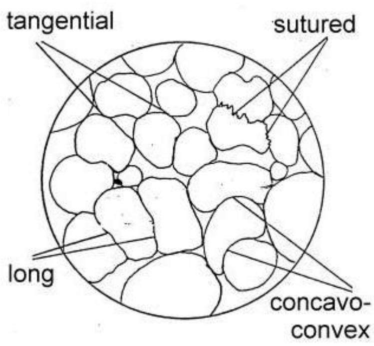

Fig. 3.7 - Diferentes processos de compactação que mudam a textura e trama das rochas. Retirado de Taylor (1950) e modificado por http://www.virtual-geology.info/sedimentology/sst-diag-lect.html.

3.3 Diagênese e ambientes de modificação de porosidade

Os processos químicos (mecanismos de cimentação e dissolução) e físicos são os principais processos diagenéticos que determinam a qualidade dos reservatórios siliciclásticos e carbonáticos (rearranjo dos grãos, deformação plástica, fraturação e compactação química). A rede de poros do reservatório é afetada por todos esses elementos (Wilson & Stanton, 1994).

Existem três ambientes diagenéticos principais em que a porosidade do carbonato é formada ou modificada: meteórico, marinho e subsuperficial (Fig. 3.8). A existência de fluidos nos poros distintamente diferentes separam dois ambientes superficiais ou próximos à superfície: meteórico e marinho (presentes nas zonas eogenética e telogenética de Choquette & Pray, 1970). Misturas de fluidos marinhos-meteóricos ou salmouras descrevem o terceiro habitat, a subsuperfície (zona mesogenética de Choquette & Pray, 1970).

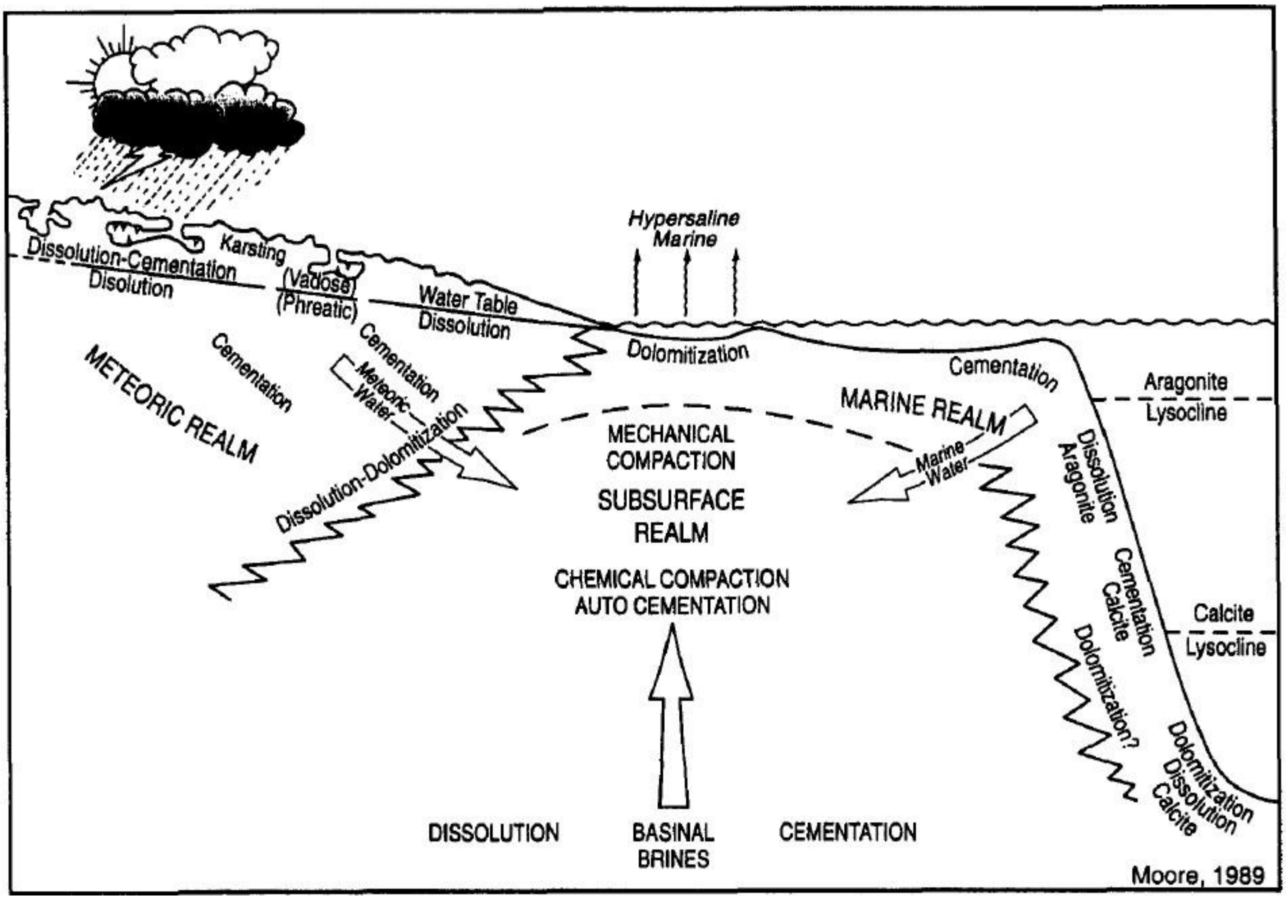

Fig. 3.8 - Diagrama esquemático que ilustra os ambientes diagenéticos comuns dentro dos quais há modificação e evolução porosidade pós-deposição. Retirado de Moore (1989).

3.3.1 Ambiente diagenético marinho

A maioria dos sedimentos carbonáticos hoje em dia são formados em um ambiente marinho com fluidos de poros marinhos normais ou modificados que são geralmente supersaturados em relação à maioria das espécies minerais carbonáticas (Moore, 1989; Morse & Mackenzie, 1990; Tucker & Wright, 1990). Como resultado, os cimentos marinhos têm o potencial de causar ampla degradação da porosidade no ambiente marinho (James and Choquette, 1983; Land, 1980). A química do carbonato das águas marinhas pode ter mudado com o tempo. As águas oceânicas foram definidas como mares aragoníticos durante os tempos climáticos de *icehouse*, e essas águas foram presumivelmente supersaturadas com todas as espécies minerais carbonáticas. No entanto, durante os períodos climáticos de estufa, as águas marinhas podem ter ficado subsaturadas em termos de aragonita, mas supersaturadas em termos de calcita (Moore and Wade, 2013). Os grãos de aragonita podem ter se desintegrado nessas circunstâncias, resultando na formação de porosidade secundária e na precipitação de cimentos de calcita, como visto em ambientes marinhos meteóricos e profundos (Palmer et al., 1988).

A velocidade de passagem do fluido pelo sistema de poros do sedimento controla a distribuição da cimentação marinha, que é influenciada significativamente por variáveis no local de deposição, tais como: níveis de energia, taxa de sedimentação, porosidade e permeabilidade do sedimento (Moore, 2001). Como resultado, a cimentação não é encontrada em todo o oceano, mas apenas em subambientes específicos adequados, como o recife de borda da plataforma e a zona intermarés (Moore, 2001). O desenvolvimento da porosidade secundária através da dolomitização é prevalente em conjunto com as águas marinhas evaporativas, mas também pode acontecer quando as águas marinhas normais se deslocam através de sequências de calcário por convecção térmica ou convecção de Kohout (Vahrenkamp and Swar, 1994).

3.3.2 Ambiente diagenético meteórico

O ambiente diagenético meteórico é caracterizado pela exposição a condições subaéreas e a presença de águas que geralmente exibem uma ampla gama de estados de saturação do mineral carbonato, do subsaturado ao supersaturado (Choquette and Pray, 1970; James and Choquette, 1984). No que diz respeito à maioria das espécies de minerais carbonáticos, os fluidos meteóricos que viajam pela zona vadosa (aquela zona acima do lençol freático onde o ar e a água estão presentes) estão gravemente subaturados. O dióxido de carbono prontamente disponível na zona do solo alimenta essa subsaturação (Moore, 1989).

Se a aragonita estiver presente nesses fluidos meteóricos subsaturados, a diferença na solubilidade entre a aragonita e a calcita fará com que a aragonita se dissolva e os cimentos de calcita se precipitem, conduzindo o sistema mineral em direção à fase de calcita estável e menos solúvel (Matthews, 1974; Moore, 1989). A capacidade do ambiente meteórico de modificar a porosidade é freqüentemente auxiliada por taxas de fluxo de fluido relativamente rápidas através da zona freática do sistema (Back et al., 1979; Hanshaw et al., 1971).

3.3.3 Ambiente diagenético subsuperficial

Os fluidos de poros, que podem ser uma combinação de águas meteóricas e marinhas (Folk, 1974) ou uma salmoura quimicamente complexa decorrente da interação rocha-água de longo prazo em temperaturas e pressões extremas, descrevem o ambiente subsuperficial (Stoessell & Moore, 1983). Por causa do contato substancial de rocha-água, as espécies de carbonato mais estáveis, como calcita e dolomita, são consideradas saturadas nesses fluidos (Choquette & James, 1987). A dissolução por pressão (*pressure solution*) é um processo de degradação de porosidade significativa que é frequentemente facilitada pela precipitação de cimento em espaços de poros próximos devido à supersaturação geral dos fluidos de poros sob os regimes de alta pressão e temperatura da subsuperfície (Moore, 2001). Finalmente, porções com subsaturação localizada causada pela degradação térmica do hidrocarboneto podem resultar na formação de porosidade secundária por meio de dissolução (Moore, 2001).

Por causa do fluxo relativamente lento de fluidos em soterramentos profundos, a maioria dos processos diagenéticos funcionam lentamente na subsuperfície (Choquette & James, 1987). Esses processos, por outro lado, requerem uma grande quantidade de tempo geológico para concluir suas tarefas. A mistura pode causar mudanças substanciais na composição do fluido de formação em sequências de subsuperfície sob o impacto da recarga meteórica pós-orogênica (Moore, 2001). Se a anidrita estiver presente e dissolvida, esses fluidos combinados podem dissolver a dolomita e precipitar a calcita (Moore, 2001).

A relação dos três ambientes diagenéticos com a modificação da porosidade é tema do segundo artigo, onde a origem e evolução do carste epigênico em reservatórios carbonáticos podem impactar na qualidade dos reservatórios.

4. ARTIGO 1

Structural and sedimentary discontinuities control the generation of karst dissolution cavities in a carbonate sequence, Potiguar Basin, Brazil

Renata E. B. Araújo[a*], Vincenzo La Bruna[a], Andrea Rustichelli[c], Francisco H. R. Bezerra[a,b], Milton M. Xavier Junior[d], Philippe Audra[e], José A. Barbosa[f], Antônio C. D. Antonino[g]

[a] Post-Graduation Program on Geodynamics and Geophysics, Federal University of Rio Grande do Norte, Brazil

[b] Department of Geology, Federal University of Rio Grande do Norte, Brazil

[c] Geology Division, School of Science and Technology, University of Camerino, Italy

[d] Department of Geophysics, Federal University of Rio Grande do Norte, Brazil

[e] Polytech'Lab - UPR 7498, Université Côte d'Azur, France

[f] Department of Geology, Federal University of Pernambuco, Brazil

[g] Department of Nuclear Energy, Federal University of Pernambuco, Brazil

*Corresponding author: renataaa.brito@gmail.com (R.E.B. Araújo)

Journal of Petroleum and Marine Geology

Volume 123, Oct 2020, 104753 - https://doi.org/10.1016/j.marpetgeo.2020.104753

Submissão: 31 de julho de 2020

Aceite: 12 de outubro de 2020

Publicado: 19 de janeiro de 2020

Abstract

Epigenetic karstic systems in carbonate rocks commonly result from progressive dissolution by acidic meteoric waters over thousands to millions of years. The generation of secondary porosity and permeability improvement due to dissolution in carbonate reservoirs of geofluids (e.g., groundwater, hydrocarbons, and CO2) can profoundly impact reservoir storage capacity and subsurface fluid flow. This study investigates the control of structural discontinuities such as stylolites, fractures, and primary sedimentary discontinuities on the generation of multiscale karst dissolution cavities by epigenetic fluid percolation in a Late Cretaceous carbonate sequence (Jandaíra Formation) in the Potiguar Basin, Northeastern Brazil. The study relies on micro and macroscale analyses such as stratigraphic logs, field structural investigations, rock strength data collected in the field (Schmidt hammer), microtomographic and drone images, thin section analyses, porosity and permeability laboratory measurements. The results show that bed-perpendicular stratabound and non-stratabound stylolites and fractures can be enlarged due to meteoric water percolation until they merge and form a single channel system that crosscuts all sedimentary multilayers. Bed-parallel stylolites are ubiquitous in carbonate sequences overprinting bed interfaces and layers. Where not dissolved, bed-parallel stylolites have low porosity and permeability and thus can act as barriers to vertical fluid flow. Where dissolved, such stylolites can contribute to horizontal fluid flow and form channel porosity. The results of this study led to a formulation of a conceptual model of rock dissolution along structural and sedimentary discontinuities that affects carbonate rock successions in the subsurface

Keywords: Karst, Dissolution, Stylolite, Fracture, Permeability, Porosity, Carbonate reservoir, Geofluids.

4.1 Introduction

Porosity and permeability commonly exhibit heterogeneous distributions in carbonate rocks at both micro and macroscales, and their prediction is still a challenge for application in reservoir models due to the high chemical susceptibility of carbonates (e.g., Moore, 1989; Moore and Wade, 2013; Tucker, 2001; Tucker and Wright, 1990). The development of macroscopic dissolution porosity and permeability systems are related to karstification or speleogenesis (Klimchouk et al., 2012; Worthington and Ford, 1997). In many carbonate reservoirs, karst porosity has been studied over the past decades. In burial settings, karst porosity is commonly related to past periods of subaerial exposure and epigenetic karstification (also known as paleokarst) (e.g., Esteban and Wilson, 1993).

Karst process can occur from the action of acidic meteoric waters that flow by gravity through carbonate rocks (epigenetic karst) and from ascending underground fluids (hypogenic karst). Previous work showed the dissolution process/porosity related to fluid flow (Beaudoin et al., 2018; Heap et al., 2018; Jacquemyn et al., 2012; Szymczak and Ladd, 2009). These phenomena occur at varying scales due to pore-network modifications (e.g. pore enlargement, creation of vugs, and pore filling by mineral reprecipitation) to cave formation (e.g., Drew, 1985; Kerans, 1988). Some karst features record paleo-water levels (Johnson et al., 1977; Kober et al., 2007; Palmer, 1987; Thomas et al., 2012) whereas others overprint stratigraphic surfaces and structural discontinuities (e. g., Cazarin et al., 2019; Fernandes et al., 2015; Filipponi et al., 2009; Heward et al., 2000; Klimchouk and Ford, 2000; Rabelo et al., 2020; Shanov and Kostov, 2015; Silva et al., 2017).

Based on physical and genetic features, 15 types of porosity were distinguished. Seven of these porosity types (e.g., interparticle, intraparticle, intercrystalline, moldic, fenestral, vug, and fracture) are prevalent in carbonate rocks. Primary rock porosity may be modified (enlarged or reduced) immediately after sedimentation by dissolution, mineral formation, compaction, and internal sedimentation which generate secondary porosity (Choquette and Pray, 1974).

In carbonate rocks, some secondary porosity due to dissolution that is not fabric selective is classified by three pores sizes: vugs, channels, and caverns (Choquette and Pray, 1970). Vugs are microscale voids with equidimensional shape and small aspect ratios while channels are elongated pores with high aspect ratios. Caverns are both channels and vugs that are large enough for people to enter. Moctezuma-Berthier et al. (2004), for example, used the term “vugs” for centimeter-scale pores and “caverns” for meter-scale pores.

Pore space must be defined and classified by considering rock fabrics and petrophysical properties (Lucia, 2007). Archie (1952) began classifying pore spaces by estimating porosity, permeability, and capillary properties and then by dividing pore space into visible porosity and matrix porosity. The former porosity type is visible on petrographic thin sections while matrix porosity consists of smaller pore sizes and is not detectable in thin sections. The pore space referred to by Choquette and Pray (1970) as "vuggy porosity" is defined more specifically as pores that are visible with the unaided eye and are visible in thin sections which formed by indiscriminate dissolution of cement and grains. However, Lucia (1983) and Lucia (1995) provided further details on the definition of "vuggy porosity" which was subdivided into two groups according to the interconnection of vugs. Vugs that are interconnected only through the interparticle pore network are called "separate vugs." Vugs that form in the interconnected pore system are called "touching vugs" (Lucia, 1983, 1995).

Other studies have shown that vugs are related to fractures, (e.g., Camacho-Velazquez et al., 2002; Gao et al., 2016; B. Li et al., 2017; Zhu et al., 2017; Worden et al., 2018) or have created models of vuggy pore networks (e.g., Moctezuma-Berthier et al., 2004; Zhang et al., 2005; 2007; Ni et al., 2013). However, studying the formation and distribution of vuggy pore spaces is still a challenge for exploring geofluid reservoirs (e.g., groundwater and CO_2 injection in the subsurface) since they present heterogeneous patterns both at thin section scales and outcrop scales. Laboratory tests (e.g., Vik et al., 2013) performed at millimeter to centimeter scales have shown spatial variations in petrophysical properties such as porosity, permeability, and dispersivity in vugular porous carbonate rocks. In addition, there is a knowledge gap regarding the correlation of microporous millimeter-centimeter scale rock samples to macroporous meter-scale outcrops.

Some previous works focused on the control of fractures, stylolites and, sedimentary surfaces on karst dissolution porosity (e.g., vuggy, channel, and cavern). According to Silva et al. (2017), different types of karst landforms are related to fracture systems, sedimentary bedding, and fluvial dynamics. Fractures are widened by dissolution due to meteoric waters to form vertical to oblique fluid conduits while dissolution occurs even along horizontal layers due to percolation of meteoric waters. Enlargement of conduits can lead to the collapse of blocks in sinkholes and cave formation (Silva et al., 2017).

Although some of these studies are related to the connectivity of stylolite surfaces and fluid percolation along them, there is a gap in the literature that shows the relationships between porosity formation along stylolites that allow the development of channel porosity.

Stylolites can act as barriers (e.g., Burgess and Peter, 1985; Heald, 1959; Koepnick, 1987) or conduits for fluid passage (e.g., Bruna et al., 2019; Carozzi and Bergen, 1987; Martín-Martín et al., 2017; Rustichelli et al., 2015). Stylolites, which act as barriers to fluid flow, can contain low permeability materials such as insoluble clay minerals, residual materials after limestone dissolution, or highly cemented halos around stylolites due to $CaCO_3$ reprecipitation (Corwin et al., 1997; Ehrenberg et al., 2006). Bed-parallel sedimentary stylolites may act as directional pathways for fluid flow by impeding vertical movements when they are the only discontinuities in the rock. Differently, fluid percolation can be decreased even more so when both sedimentary and tectonic stylolites are present (Alsharhan and Sadd, 2000; Bushara and Arab, 1998; Koepnick, 1987; Lavenu and Lamarche, 2018; Martín-Martín et al., 2017). Stylolites are commonly associated with fractures since they can be connected by mode I fractures, which emanate from stylolite teeth, or by mode II fractures when increased shear stress causes fracturing (Ben-Itzhak et al., 2014).

This study focuses on the Cretaceous shallow-water carbonates of the Jandaíra Formation in the Potiguar Basin of Brazil. We selected this basin because it is an easily accessible region where it is possible to study carbonate reservoir analogs (e.g., Carlotto et al., 2017; Chafetz et al., 2018; Goldberg et al., 2017; Herlinger et al., 2017; Lima and De Ros, 2019). These outcrops show impressive karst dissolution cavities from millimeters to tens of meters in size superimposed on sedimentary surfaces, stylolites, and fractures and display both vertical and horizontal patterns. Study of these outcrop analogs is important since many features (e.g., vuggy pores, sedimentary beds and laminae, fractures, and stylolites) are below the resolution of seismic techniques and well and ground penetrating radar (GPR) data and thus are detectable only in field analyses.

The objective of the study is to analyze structural and sedimentary discontinuities such as stylolites, fractures, and cross stratifications both in the field and the laboratory (petrographic and petrophysical analyses) to understand their control on formation and spatial distribution of karst dissolution features in carbonate rocks from microscales (e.g., thin sections and Micro CT images) to outcrop scales (e.g., field and drone image analyses). Micro CT image analyses were mainly performed along bed-perpendicular and bed-parallel stylolites. New challenges in fractured and karstified carbonate reservoirs require integrating these data since karsts affect fluid circulation, collapse of drilling columns, and reservoir porosity and permeability (e.g., Aquilina et al., 2003; Klimchouk and Ford, 2000; H. Li et al., 2017; Youssef and Awotunde, 2019). Along this line, the analysis of outcropping analogs to the subsurface carbonates is often employed to lower the uncertainties and bias associated with reservoir characterization and modeling (Agosta et al., 2010; Giuffrida et al, 2019, 2020; La Bruna et al, 2017, 2018; Lamarche et al., 2012; Rustichelli et al., 2013).

4.2 Geological setting

The Potiguar Basin (Fig. 4.1A) is located in the eastern part of the Brazilian equatorial margin and was formed as a result of the South America and Africa breakup during the Pangea rifting (Matos, 1992, 2000; de Castro et al., 2012; Melo et al., 2016). Proterozoic NE-SW and E-W trending shear zones associated with the Brazilian/Pan-African Orogeny (Matos, 1992) were reactivated as normal faults during Late Cretaceous rifting. This process allowed the formation of several intra-continental basins in Northeastern Brazil, such as the Potiguar Basin (Brito Neves et al., 1984; de Castro et al., 2012).

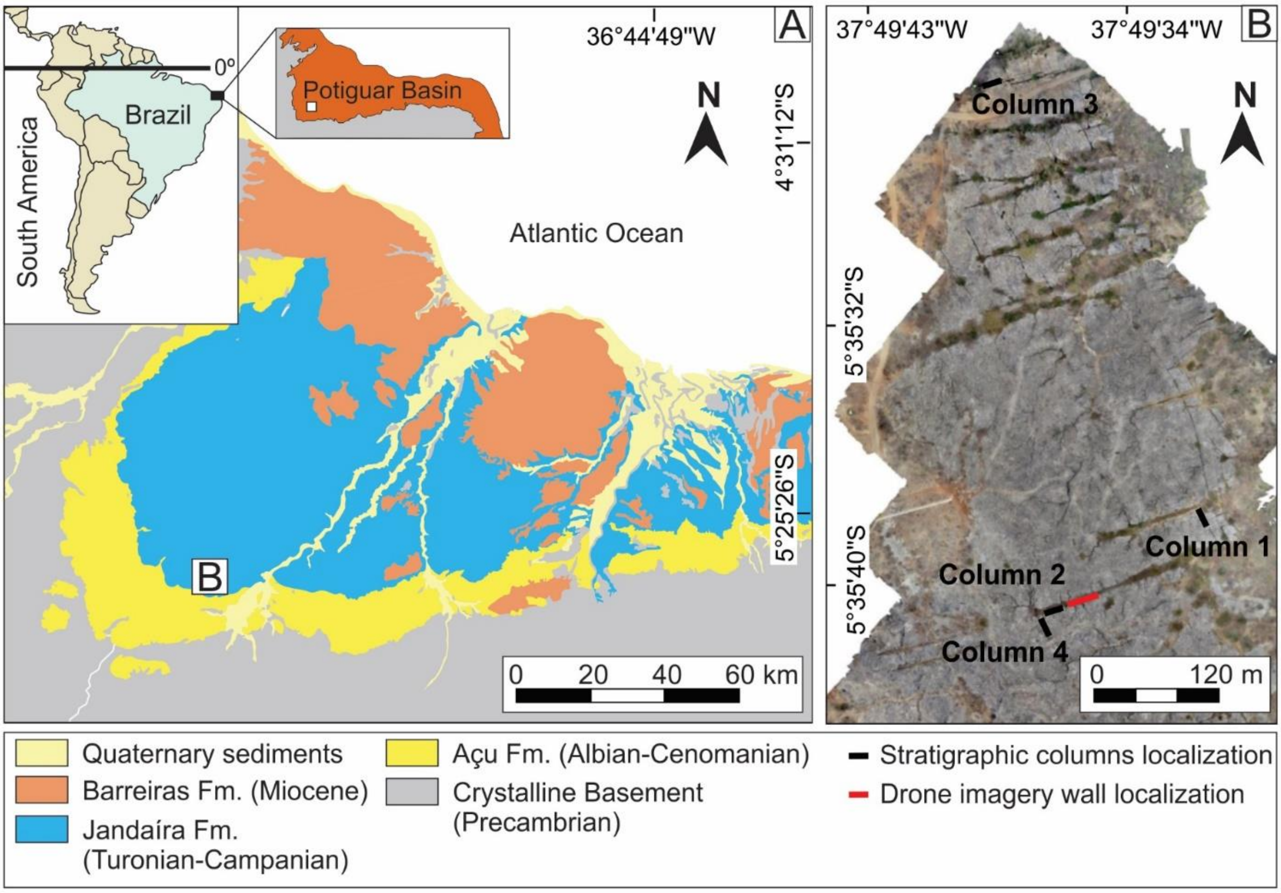

Fig. 4.1 – (A) Simplified geological map of Potiguar Basin and Soledade outcrop location; (B) Drone imagery of the Soledade outcrop.

The Potiguar Basin was involved in three main tectonic stages from the Early Cretaceous to the Quaternary: rift, post-rift, and drift (Pessoa Neto et al., 2007; Souza, 1982). The rift stage can be further subdivided into two distinct tectonic phases: an extensional tectonic phase with high subsidence rates followed by a strike-slip phase. NE-

SW trending normal faults define asymmetric structural highs in the basement in this stage. Two strike-slip stress fields characterized the post-rift stage. The first was a Late Cretaceous to Miocene N–S-oriented horizontal compression and E-W-oriented horizontal extension; the second was a Miocene to Quaternary E-W-oriented horizontal compression and N–S-oriented horizontal extension which rotated clockwise approximately 30◦ in the west part of the basin (e.g., Bezerra et al., 2020; 2011; Reis et al., 2013). These stress fields were constrained by temporal sequences and volcanic rock chronology (Bezerra et al., 2020). The resulting faults are mostly strike-slip in their kinematics and some are reactivated faults from the rift phase (de Castro et al., 2012). At outcrop scale, several structures such as fractures, veins and stylolites formed during the subsidence phase in the Late Cretaceous to Paleocene (Bertotti et al., 2017). The Jandaíra carbonate rocks were affected by both roughly N–S striking sub-vertical joints and shear joints and by sub-vertical E-W trending stylolites (Bertotti et al., 2017). Sub-vertical compression due to progressive accumulation of younger rock layers during subsidence also caused the formation of bed-parallel stylolites that formed at depths estimated between 500 and 800 m (Bertotti et al., 2017).

The Jandaíra Formation is a part of a post-rift sedimentary sequence and consists of shallow-water carbonates deposited in the Late Cretaceous (Sampaio and Schaller, 1968). Jandaíra carbonates consist of gently dipping (<5◦) sub-horizontal beds which dip to the north. Sub-sequently, these carbonates were dissected by extensional faults associated with the South Atlantic opening (Matos, 1992; Pessoa Neto et al., 2007).

Jandaíra Formation carbonates consist of shallow-marine limestone facies which formed in water depths less than 50 m according to the biota assemblages (e.g., ostracodes, green/red algae, planktonic and benthonic foraminifera, and Echinoidea) (Tibana and Terra, 1981). The dominant carbonate facies are (i) bioclastic packstones to wackestones, which record a marine system with low water energy and (ii) bioclastic grainstones to packstones, which indicate a shallow-marine system with higher water energy (Santos Filho et al., 2015). Additional facies include oolitic grainstones, mudstones bearing both planktonic and benthonic foraminifera, and mudstones with birds-eyes (Santos Filho et al., 2015). Dolomitization frequently occurs in low water energy facies and less frequently in high water energy facies (Tibana and Terra, 1981).

4.3 Methodology

4.3.1 Stratigraphic logging

Our study is located along several natural vertical walls in the Soledade outcrop which are oriented NNW-SSE and ENE-WSW (Fig. 4.1B). Four detailed stratigraphic logs were obtained at these sites (Fig. 4.1B). Preliminary characterizations of bedding surfaces, lithologies, sedimentary structures (e.g., laminations) and evidence of karst dissolution were accompanied by the collection of 107, 1-inch (~2.5 cm) diameter bed-parallel (58) and bed-perpendicular (49) plugs. All plugs were cut to a height of 4 cm high for both petrographic and petrophysical characterizations. We opted to collect the most homogeneous plugs, along a pristine portion of the studied outcrops that showed no visible pores as vugs or channels for porosity characterization.

4.3.2 Structural analysis

At each outcrop, we performed high-resolution stratigraphic logging and qualitative structural analysis of the different structural elements documented in the studied outcrops. Detailed structural analysis was aimed at deciphering geometry, orientation, internal structure, infilling material (if present), possible offset, and the abutting crosscutting relationships concerning the surrounding other elements. Concerning stylolites, their orientation was measured concerning for their main dissolution plane.

4.3.3 Schmidt hammer analysis

In addition, the present-day mechanical properties of the carbonates, namely, the uniaxial compressive strengths (UCS), were estimated by following published procedures (Aydin, 2008; Aydin and Basu, 2005; Zoback, 2007) using the Schmidt Hammer Rebound Hardness test. This analysis was performed perpendicularly to the rock surface in three from four stratigraphic logs and avoided dissolved portions of the outcrop. The Schmidt hammer test measures the number of rebounds of a spring-loaded mass impacting the rock surface. The number of rebounds was measured 20 times in correspondence to a unique site for each layer and each bedding surface layer by holding the hammer orthogonal to a flat, smooth, vertical rock surface. These 20 rebound number values were collected in two different portions: (1) within individual layers of approximately 200 cm2 area and (2) along individual bedding surface layers approximately 50 cm long. All of these rebounds were collected one on top of the other. An average was subsequently calculated for the 20 rebound measurements. The mean value of each layer's rebounds and each bedding surface were converted to UCS values by referencing the conversion chart (Table 4.1), following pre-established standards by the American Society for Testing and Material (ASTM, 2001).

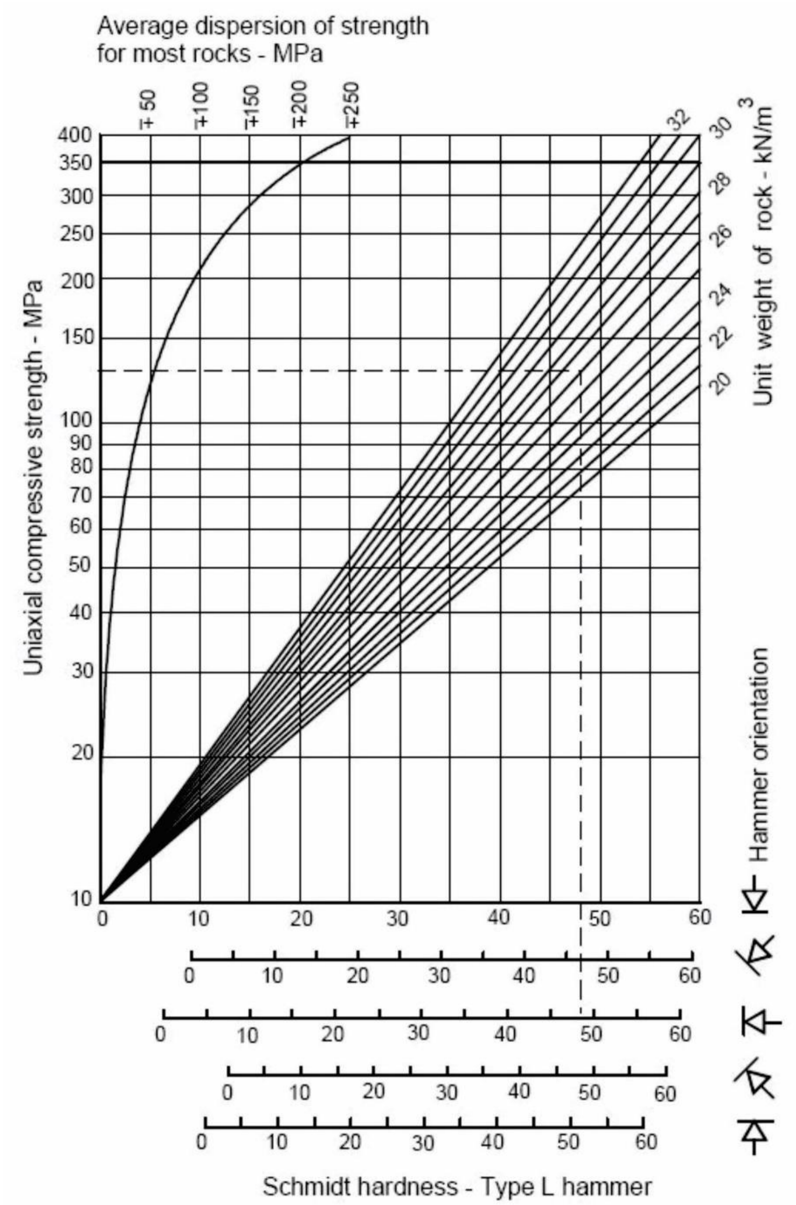

Table 4.1 - Schmidt hammer chart.

4.3.4 Drone imagery acquisition and segmentation

We computed two different digital models of Soledade outcrop. The first one consists of a 420 m x 680 m-wide model, obtained by drone imaging analysis from a height distance of ~15 m, which provided a pixel resolution of 4 cm (Fig. 4.1B). The second model refers to a 3 m height x 14.5 m-wide portion of a vertical wall. Automatic and manual flights were carried out to survey the outcrop wall. First, we generated the surface project with 80%/80% orthophotogrammetric overlap using pix4D Mapper software. Shots were taken every 2 s at a constant speed of 2 m/s. Then, surface mapping was conducted for altimetric and planimetric support in addition to wall mapping.

In the second model, referring to the vertical wall, three columns with different levels of karstification, on the same wall, were chosen from the drone imagery for segmentation and attribute determination. Each column was divided into two sections: 1 m wide by 3 m high for better visualization and analysis. Each section was segmented and divided into ten uniform horizontal subsection areas. The porosity for each area was computed in *ImageJ* software. All images were segmented using the threshold selection method from gray-level histograms proposed by Otsu (1979), and the resulting images were used for the computation of porosity values. Graphs were generated with *Origin 6.1* software.

4.3.5 Petrographic analysis

The laboratory work included petrographic analyses of 119 thin sections that were obtained from plugs collected in the field. Petrographic analyses were carried out using an Olympus BX41 polarized light microscope equipped with a digital camera. Rocks were classified based on their texture according to (Dunham, 1962; Embry and Klovan, 1971). The porosity visible in thin sections was characterized following the Lucia (2007) classification to recognize blue epoxy-stained areas as pore spaces (Gardner, 1980). The goals were to document and analyze karst nucleation and development ranging from micrometer to millimeter scales.

4.3.6 Petrographysical analysis

Petrophysical analyses included porosity, permeability, density, and volume pore measurements performed by means of a Coreval system (unsteady-state gas permeameter and porosimeter at overburden pressure) on 1-inch (~2.5 cm) diameter and 4-cm high plugs. Pore volume calculations were obtained using N_2 gas at a confining pressure of 1000 psi which simulated the pressures in analogous reservoirs. Additionally, Klinkenberg permeabilities (mD) were computed and used the Klinkenberg correction method (Jones, 1972; Klinkenberg, 1941; Li et al., 2016; McPhee and Arthur, 1991).

4.3.7 Computed tomography (CT)

Ten plugs were scanned using a computed tomography (CT) Nikon XT H 225 ST system at the Federal University of Pernambuco, Brazil. Scanning was performed with 3016 projections (1 frame per projection with an exposure time of 500 ms each) with angular steps of 0.12◦. We used an acceleration voltage of 150 kV and a current of 80 μA. A 1.0 mm thick aluminum filter was placed between the X-ray source and sample to reduce artifacts due to beam hardening effects. Samples were positioned 32.4 cm from the X-ray source which generated 2D images with a pixel size of 35 μm and, after reconstruction, a 3D model with a voxel size of 35 μm. The distance from the source to the detector was 117.6 cm (this distance is fixed on the tomography). All imagery reconstruction was performed using CT Pro 3D software.

For standardization and attribute comparisons, after reconstruction of the images, 950 CT slices from each scanned plug were used. This procedure takes inspiration from the methodology described in Wang et al. (2020). A 3x3x3 Gauss Kernel filter was used to reduce noise in the preprocessing phase. We consider one voxel as the minimum size of voxel clustering for reconstruction. After segmentation, the “erode” tool from the ImageJ software was applied to remove isolated small artifacts from the images. Evaluation of relative errors related to the segmentation method was performed based on the variation of the threshold intensity by 1%. ImageJ and 3DSlicer free software were used to perform digital image processing and analysis. Due to small irregularities at the edges of the plugs, a region of interest in each CT image was extracted to avoid these problems. All images were segmented using the same method of drone imagery segmentation and the resulting 3D binary images (plugs) were used for the computation of porosity values. Total connected and isolated porosities were obtained every 2.5 mm along the plugs. In the segmentation process, only the largest connected area in each plug was calculated throughout the segmentation process to obtain the connected porosity. Disconnected porosity was obtained as the difference between the total and the connected porosity. All data analysis (e.g., total, connected, and isolated porosity) along the plugs was computed to generate graphs using Origin 6.1 software.

4.4 Results

Karstification occurred at different stratigraphic levels within the carbonate sequence where slightly karstified horizons alternated with more karstified rocks (Fig. 4.2A, C, D). In agreement with previous work (Fernandes et al., 2015), dissolution evidence occurs: (i) along bed-perpendicular fractures, faults, and stylolites, (ii) within sub-horizontal layers, and (iii) along bedding surfaces (Fig. 4.2). Fractures and faults enlarged by dissolution are stratabound or non-stratabound and are arranged into two orthogonal fault and fracture sets which strike ca. ENE-WSW and NNW-SSE (Fig. 4.1B). ENE-WSW-striking fractures are more enlarged by dissolution than the fractures with NNW-SSE-strikes. The sub-horizontal sedimentary layers are 14 cm–95 cm thick and dip gently to the NE (<5◦) (Bertotti et al., 2017) and also show planar cross stratification intervals which are in the same direction as well as horizontal planar laminations. Sedimentary discontinuities are locally superimposed by sedimentary, bed-parallel stylolites at times.

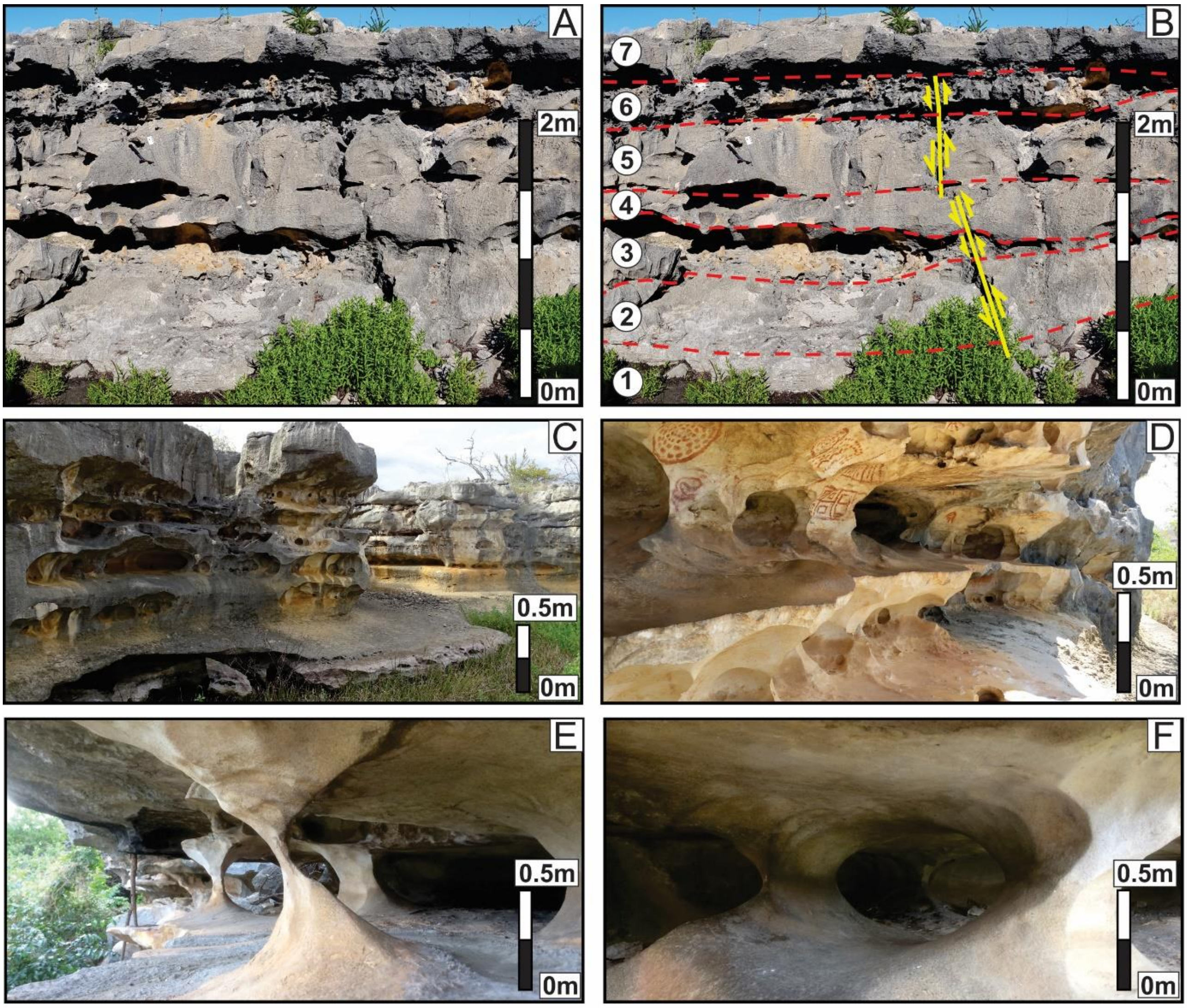

Fig. 4.2 - Karst porosity at the outcrop scale: (A) and (B) karstification occurred at different stratigraphic levels: dissolution evidence occurs along sub-vertical fractures (yellow lines), within sub-horizontal layers and bedding interfaces (red dashed lines); (C) and (D) cavern pore spaces localized on wall notches in sub-horizontal beds; (E) notches separated by thin pillars and (F) pendants. (For interpretation of the references to color in this figure legend, the reader is referred to the Web version of this article.)

4.4.1 Outcrop scale sedimentological analysis

Detailed analysis of the four stratigraphic logs (Fig. 4.3) allowed identification of five carbonate facies based on the dominant textures (e. g., packstones, grainstones and minor mudstones-bindstones, and crystalline). Karst dissolution along sedimentary discontinuities is mainly localized along bedding surfaces which refers to both the original depositional surfaces (including planar cross-bedding) and super- imposed bed-parallel stylolites, as well as along horizontal planar laminations (Fig. 4.5).

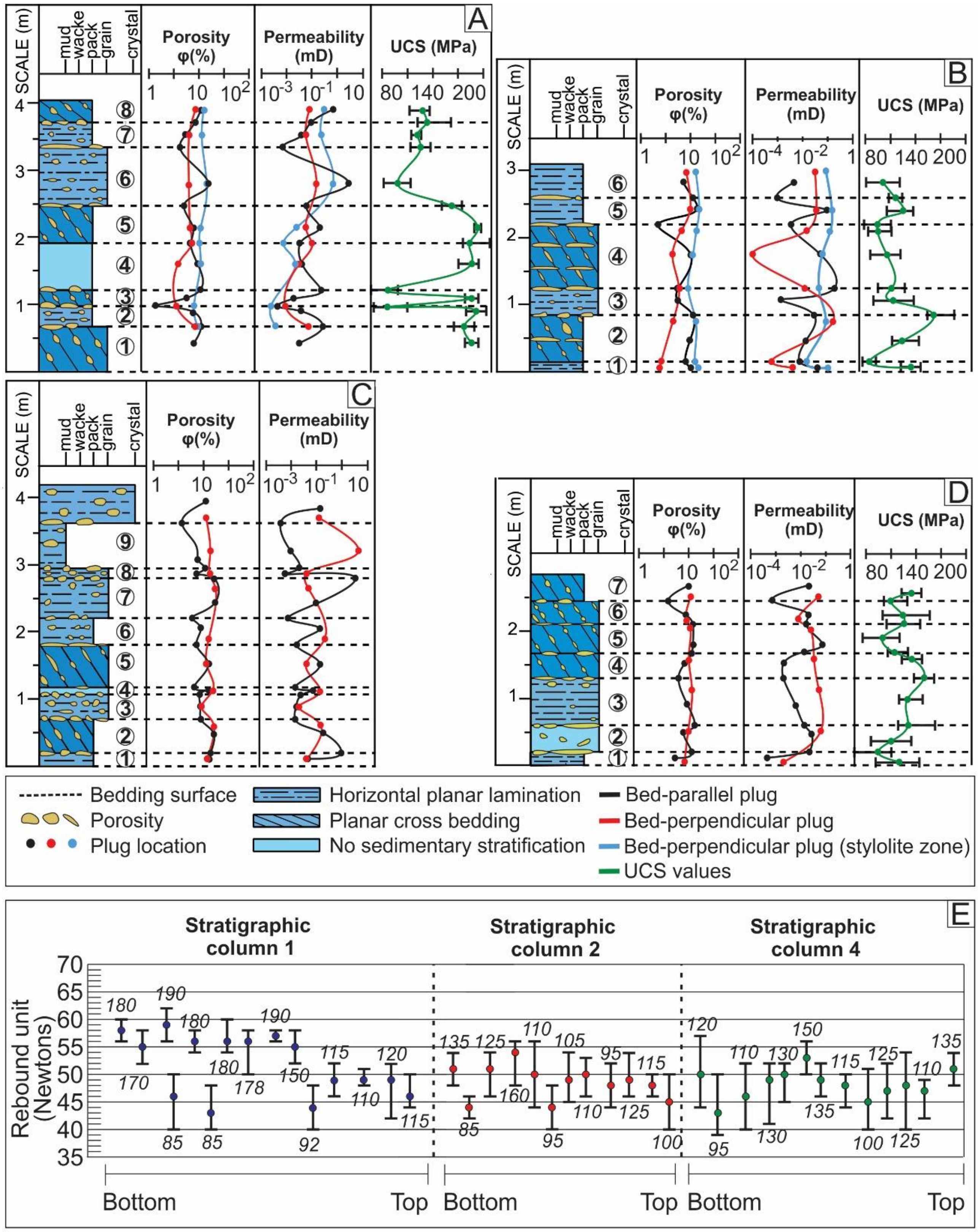

Fig. 4.3 - Stratigraphic columns showing plug directions and positions. (A), (B), (C), and (D) corresponds to columns 1, 2, 3, and 4, respectively; (E) vertical error bars indicate the ranges of the hammer rebound measurements. Numbers in each rebound range represent the converted UCS (MPa) values.

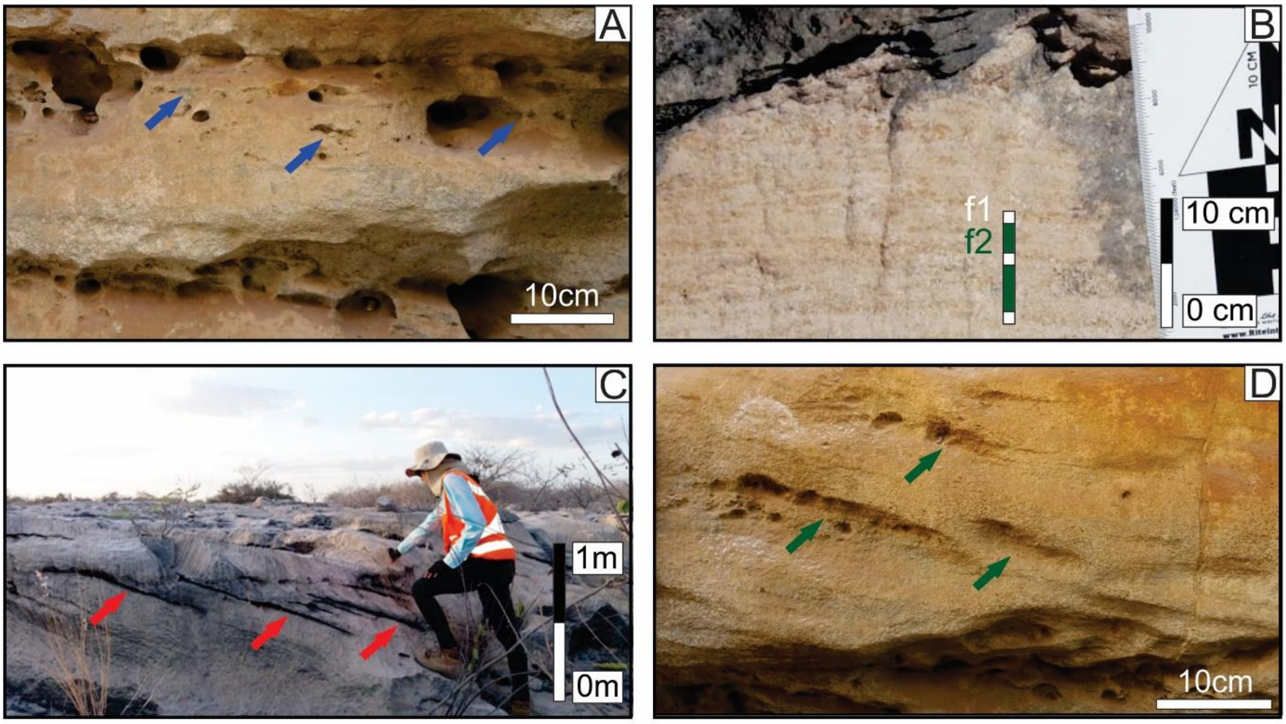

Fig. 4.4 - Sedimentary discontinuities at the mesoscale view showing: (A) dissolution following horizontal planar lamination (blue arrows); (B) close up view on outcrop showing horizontal planar lamination presenting alternate foresets, characterized by different colors associated with a change in the grain size range (f1 = dark yellow thinner foreset, f2 = light yellow thicker foreset); (C) outcrop view of dissolution features following planar cross bedding that reach a few meters in length (red arrows); (D) close up view on outcrop displaying how dissolution follows planar cross bedding in a layer zoom (green arrows). (For interpretation of the references to color in this figure legend, the reader is referred to the Web version).

Stratifications consist of beds ranging from centimeters to a few meters in thickness and millimeters thick laminae and show color differences that correspond to alternating foresets. These alternations are controlled by grain size changes and/or variations in cementation grade (Fig. 4.4B).

Bed-parallel stylolites are isolated or anastomosing along bedding surfaces (Fig. 4.5A–F). These stylolites can be partially dissolved and different levels of dissolution can follow them such as vuggy pores, channel pores, and/or cavern pores (Fig. 4.5G and H).

4.4.2 Outcrop-scale structural analysis

Structural mapping revealed the following fracture sets:

i. bed-perpendicular stylolites striking ENE-WSW (Fig. 4.6A and B);

ii. bed-perpendicular, stratabound and non-stratabound fractures, mostly joints, striking NNW-SSE or ENE-WSW (Fig. 4.1B, Fig. 4.6C and Fig. 4.6D);

iii. bed-perpendicular stratabound or non-stratabound fractures and veins striking N–S to NNE-SSW, which either crosscut or abut against ENE-WSW-striking bed-perpendicular stylolites (Fig. 4.6B, C and D);

iv. and bed-perpendicular stratabound or non-stratabound stylolites striking N–S to NNE-SSW (Fig. 4.6E and F) which abut against ENE- WSW-striking bed-perpendicular stylolites (Fig. 4.6G and H).

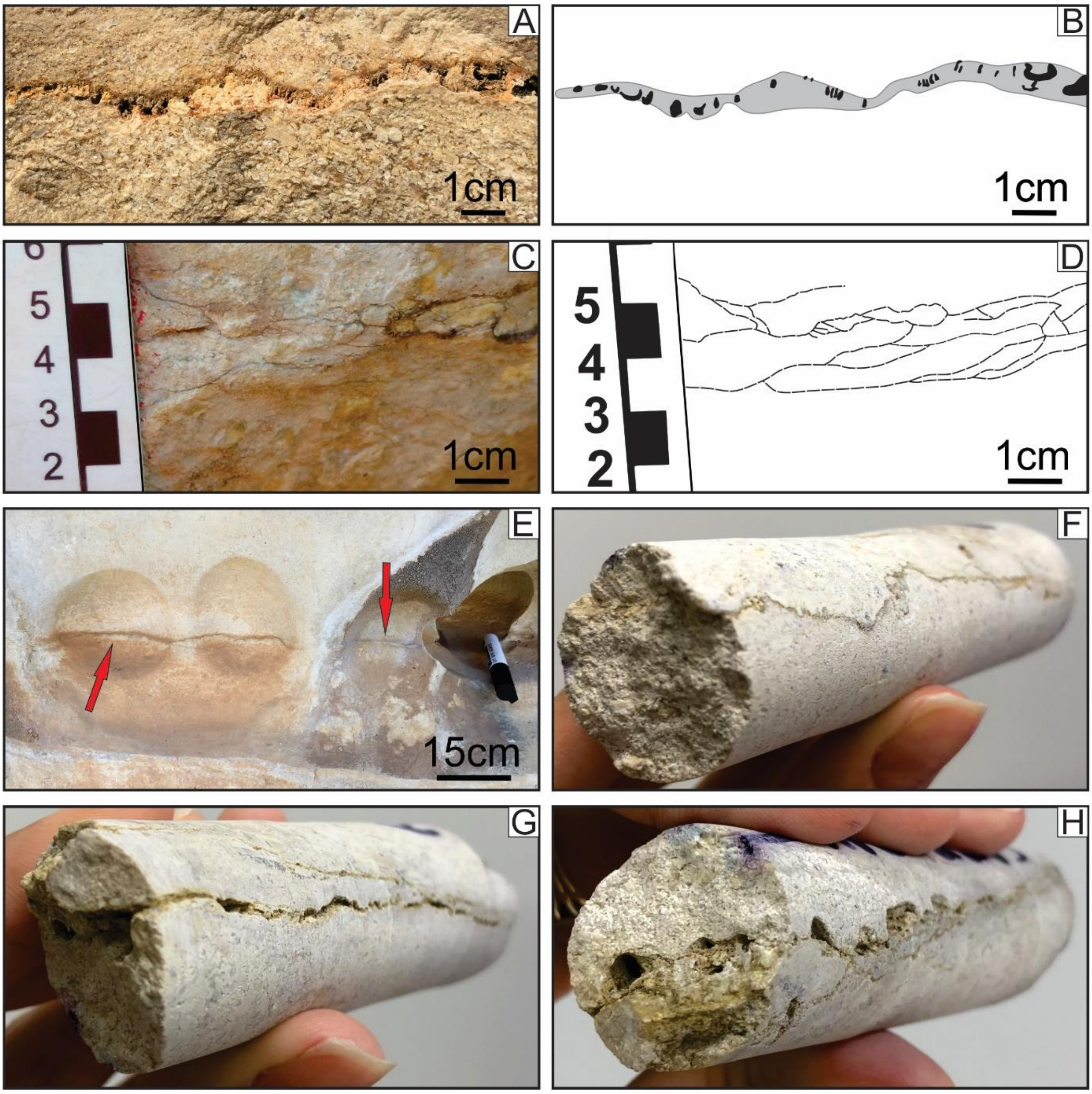

Fig. 4.5 - Millimetric bed-parallel stylolites along bedding surfaces: (A) and (B) isolated stylolite; (C) and (D) branched stylolites partially filled with ferruginous material; (E) stylolite (red arrows) at an outcrop view; (F) stylolite shape in a 3D view; (G) dissolved stylolite characterized by vuggy pore space in a 3D view; (H) vuggy pore space well developed along stylolite. Plugs from F, G, and H

are 1-inch (~2.5 cm) in diameter. (For interpretation of the references to color in this figure legend, the reader is referred to the Web version of this article.)

Dissolution features such as vuggy, channel, or cavern pores are more pronounced when they are close to dissolved bed-perpendicular fractures or bed-perpendicular stylolites and along bed interfaces on the tops of the analyzed carbonate rock walls.

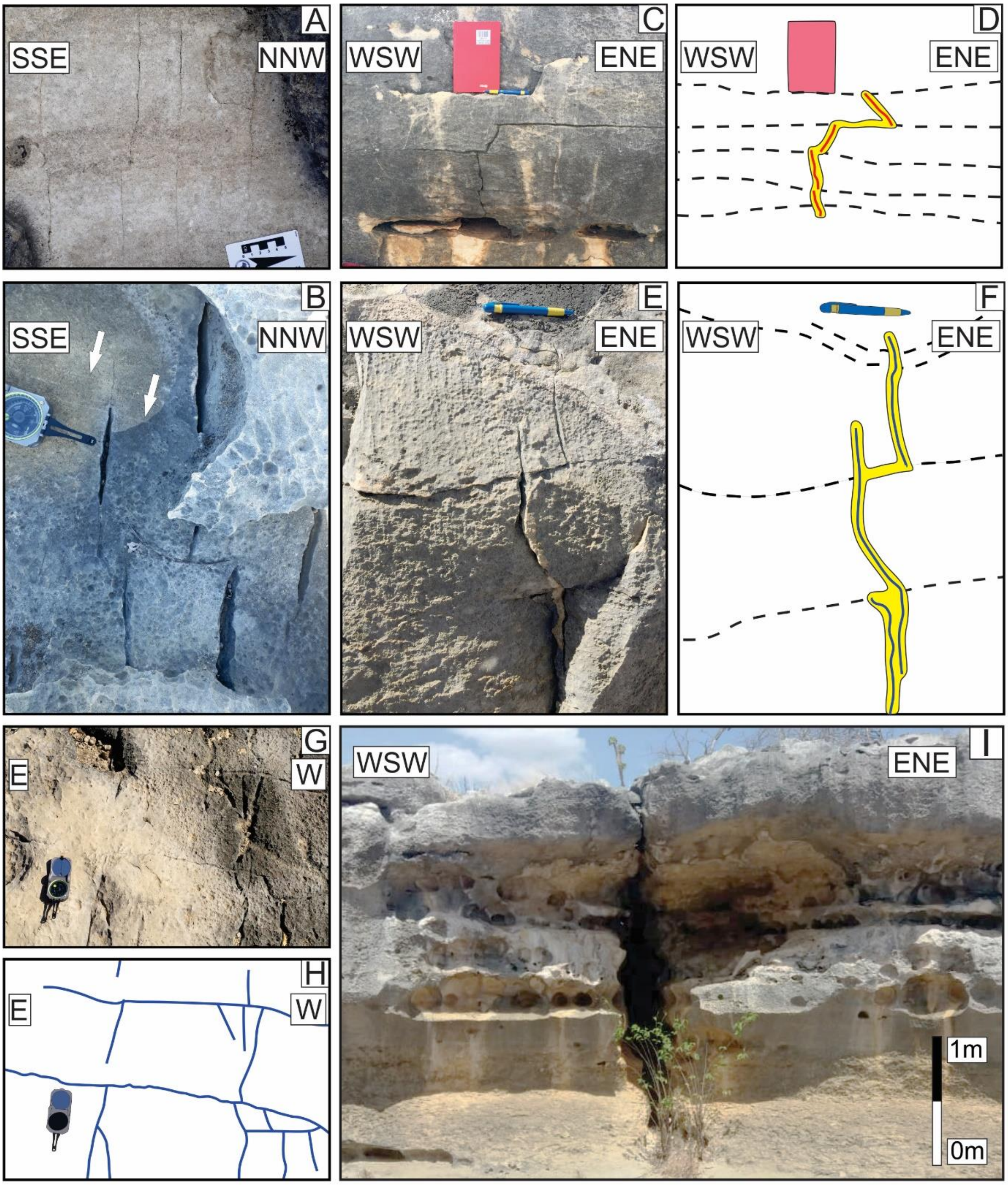

Fig. 4.6 - Stylolite and fracture occurrence at the outcrop scale: (A) bed-perpendicular stylolites; (B) dissolved bed-perpendicular stylolites. Bed-perpendicular veins (white arrows); (C) and (D) bed-

parallel stylolites (black dashed lines), bed-perpendicular stratabound, and non-stratabound fractures (red lines) are linked to form dissolved portion around fractures (yellow contour); (E) and (F) bed-parallel stylolites (black dashed lines), bed-perpendicular stratabound, and non-stratabound stylolites (blue lines) are linked to form dissolved portion around stylolites (yellow contour); (G) and (H) N–S to NNE-SSW bed-perpendicular stylolites abut against ENE-WSW bed-perpendicular stylolites; (I) dissolved sub-vertical fractures and stylolites cutting across the carbonate multilayers, forming narrow caverns. Note that vuggy pore space follows a rectilinear tendency along layers and contact layers. (For interpretation of the references to color in this figure legend, the reader is referred to the Web version of this article.)

Bed-perpendicular stylolites are up to a few decimeters to a few meters in length (Fig. 4.6). Some stylolites are isolated and exhibit clear terminations and show no connections to other stylolites or fractures (Fig. 4.6A and B). Isolated bed-perpendicular stylolites can be connected to other bed-perpendicular isolated stylolites and/or fractures by increased dissolution and form narrow caverns (Fig. 4.6I).

4.4.3 Uniaxial compressive strength (UCS) measurements

In columns 1, 2, and 4, UCS values range from 80 to 200 Mpa. In general, column 1 displays measurements with the greatest variation among all analyzed columns (from 80 to 200 Mpa). Columns 2 and 4 (from 80 to 160 Mpa) show the lowest to intermediate measurements. Column 4 shows measurements with the least variation among all analyzed columns (from 100 to 140 Mpa). Column 1 (Fig. 4.3A): layers 1, 2, 3, 4, and 5 show high UCS values (approximately 200 Mpa), although the bedding surfaces between layers 2–3 and layers 3–4 show low UCS values (e.g., approximately 80 Mpa). Uniaxial compressive strengths are high in layers 4 and 5 but decrease toward the top of the stratigraphic column. Column 2 (Fig. 4.3B): layers 1, 2, and the bedding surface between layers 2–3 show intermediate uniaxial compressive strengths (from 120 to 160 Mpa). The UCS values calculated on the bedding surfaces between layers 1–2 are approximately 80 Mpa and represent the lowest values. In Column 4 (Fig. 4.3D), uniaxial compressive strengths are higher in the layers than in the bedding surfaces.

4.4.4 Petrographic analysis

Microfacies are mostly represented by laminated microbial bindstones (Fig. 4.7A), peloid-bearing mudstones (Fig. 4.7B), both peloidal and skeletal packstones, and skeletal grainstones (Fig. 4.7C and D), all of which indicate shallow marine depositional environments with variable water depths and water energy conditions. Some fossil-free crystalline carbonates consisting of calcite and/or dolomite are also documented (Fig. 4.7E and F).

In the thin sections, porosity types were determined based on the principles in Lucia (2007): no evident dissolution of grains (Fig. 4.7D), vuggy pore spaces (separate vugs) (Fig. 4.8A), vuggy pore spaces (touching vugs) (Fig. 4.8A), interparticle pore spaces (Fig. 4.8B and C), interparticle pore spaces forming channel porosity (Fig. 4.7F), undissolved stylolites filled with brown-dark clay minerals (Fig. 4.7E), partially dissolved stylolites (Fig. 4.8D), isolated fully dissolved stylolites showing channel porosity (Fig. 4.8E), and branched stylolites associated with microfractures showing channel porosity (Fig. 4.8F).

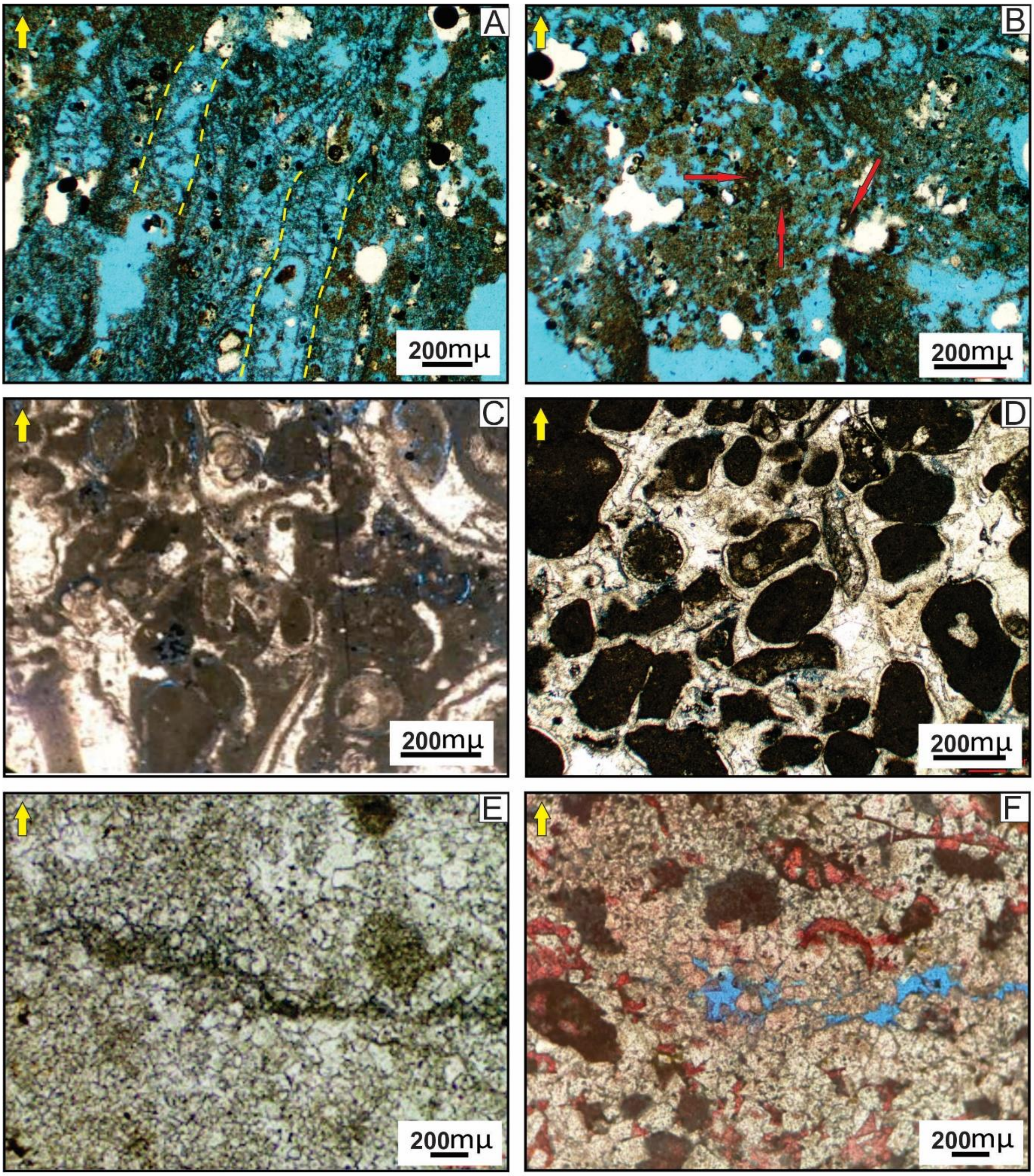

Fig. 4.7 - Porosity at the microscopic scale: (A) laminated microbial bindstones (some laminae are evidenced by yellow dashed lines). Vuggy porosity is more developed in some laminae than others; (B) peloid-bearing mudstones (red arrows); (C) skeletal packstone; (D) grainstone; (E) non-dissolved stylolite in crystalline carbonate; (F) interparticle porosity in dolomite cement arranged as forming channel porosity. Yellow arrows display stratigraphic up. (For interpretation of the references to color in this figure legend, the reader is referred to the Web version of this article.)

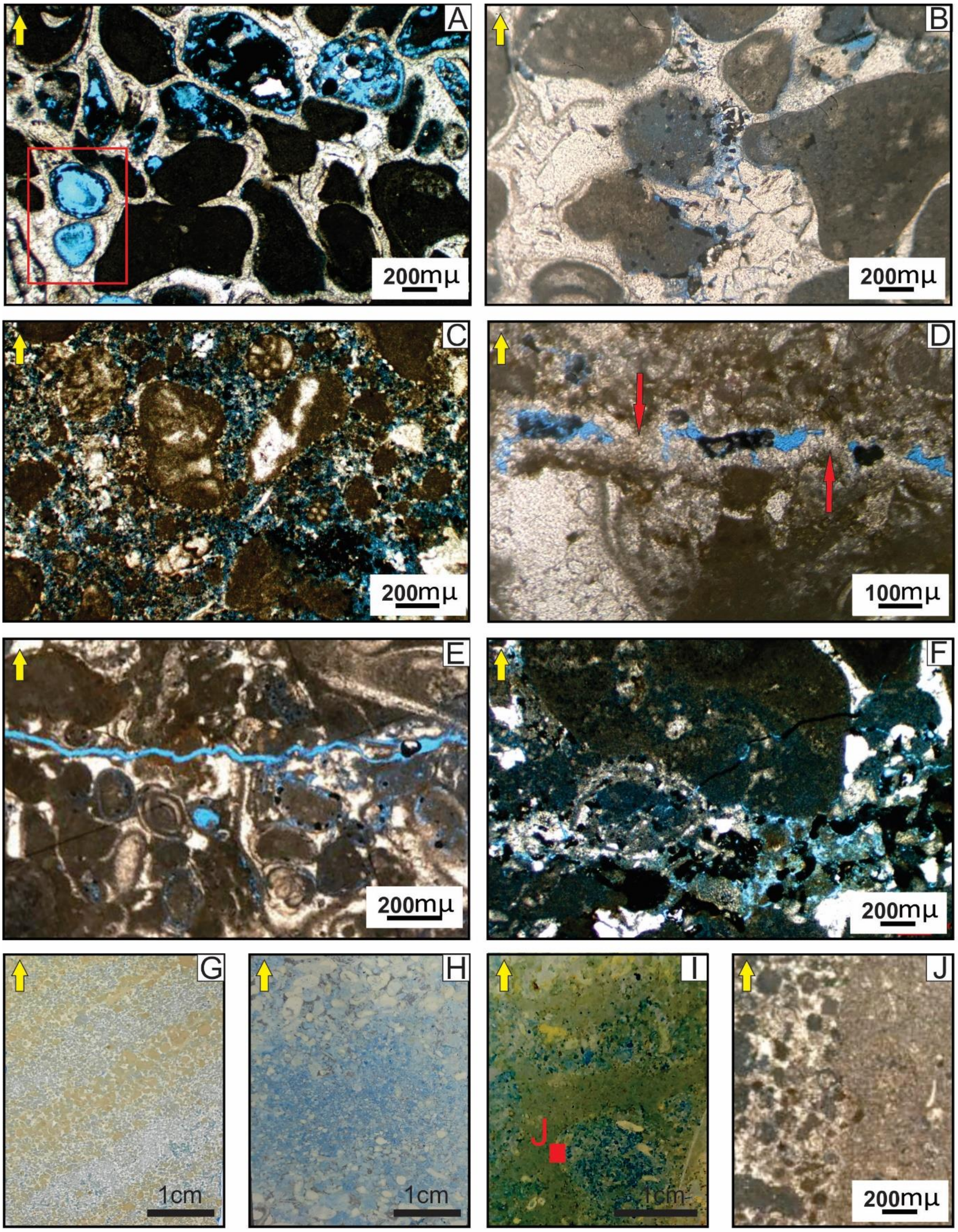

Fig. 4.8 - Porosity and dissolution features at the thin-section scale: (A) separate vugs inside grains and touching vugs in red rectangle; (B) beginning of interparticle pore space; (C) Interparticle pore space; (D) stylolite partially dissolved and separate vugs evolving touching vugs. Red arrows indicate non-dissolved portions of stylolite; (E) stylolite fully dissolved shows a single channel porosity; (F) stylolites (red arrows) and microfractures (white arrows) from compaction are dissolved and form branched channel porosity; (G) planar cross bedding in a thin section view showing alternate foresets separated in larger grain portions (yellow) and partially dissolved smaller grain portions (blue); (H) alternate foresets of smaller grains with more dissolution evidence than larger grains; (I) and (J) dissolution due to different types of cementation. Yellow arrows display stratigraphic up.

Dissolution following sedimentary discontinuities such as planar cross-bedding and horizontal planar laminations is focused on calcite cements that filled portions and laminae in the carbonate rocks which are characterized by small grain sizes and seem to be enhanced in some cement generations relative to others (Fig. 4.8G–J).

Microstructural analysis from thin sections reveals: bed- perpendicular stylolites filled with blocky calcite striking ~ NNE-SSW (Fig. 4.9A), bed-perpendicular stylolites filled with microsparry calcite striking ~ E-W (Fig. 4.9B), bed-perpendicular shear veins filled with blocky calcite striking ~ N–S (Fig. 4.9C), bed-perpendicular disrupted veins filled with fibrous calcite striking ~ ENE-WSW to WNW-ESE (Fig. 4.9D), randomly distributed microfractures (Fig. 4.9E), and moldic pores connected by N–S microfractures and filled with calcite (Fig. 4.9F).

4.4.5 Three-dimensional porosity and permeability tests in the laboratory

Bed-parallel plugs show porosity variations between 5% and 16% except for the bedding surface between layers 2 and 3 in column 1 (Fig. 4.3A) and the bedding surface between layers 4 and 5 in column 2 (Fig. 4.3B), which show porosities near 1%. Permeabilities vary considerably in all columns.

Bed-perpendicular plugs without stylolite zones exhibit a 5–16% porosity range with an average close to 10%. In column 1, the porosity values are approximately 5% along the sampled bedding surfaces between layers 2–3 and layer 4 (Fig. 4.3A). Porosity is near 5% at the bottom of column 2 (Fig. 4.3B) and increases to 10% on the top. Permeabilities show greater variations when compared to porosities. In column 1 (Fig. 4.3A), permeabilities are lower (near 10—2 mD) in the bottom portions and are linear from the bedding surface between layers 4 and 5 to the top of the column (near 10—1 mD). In column 4 (Fig. 4.3D), permeabilities are lower in layer 1 (near 10—3 mD) and are linear up to the top of the column (near 10—2 mD). The permeabilities vary much more in columns 2 and 3, the lowest values are near 10—4 mD, and the largest values are near 10 mD.

The bed-perpendicular plugs in stylolite zones collected in columns 1 and 2 (Fig. 4.3A and B) show that porosity is nearly linear for all layers and bedding surfaces for which the porosity values are close to 10%. Permeabilities increase from the bottom to top of column 1, which are different from column 2, in which the permeabilities follow a linear trend.

Porosities in the carbonate facies range from 1.42% to 16.64% (Table 4.2). For the dominant facies, grainstone porosities range from 2.1% to 16.64%, whereas they range from

1.42% to 15.47% in packstones. Stratigraphic log analysis highlighted a single mudstone layer with 6.85% porosity in bed-parallel plug, 13.14% porosity in bed-perpendicular plug, and another layer of crystalline carbonate that displays a porosity range between 3.44% and 10.19%. Porosities along bedding surfaces vary from 1.42% to 15.61% and inside layers, vary from 5.23% to 16.64% (Table 4.2). The grainstones generally show porosity values that are slightly higher than in packstones. Moreover, the middle portions of layers show somewhat higher porosity than bedding surfaces, independent of the carbonate facies.

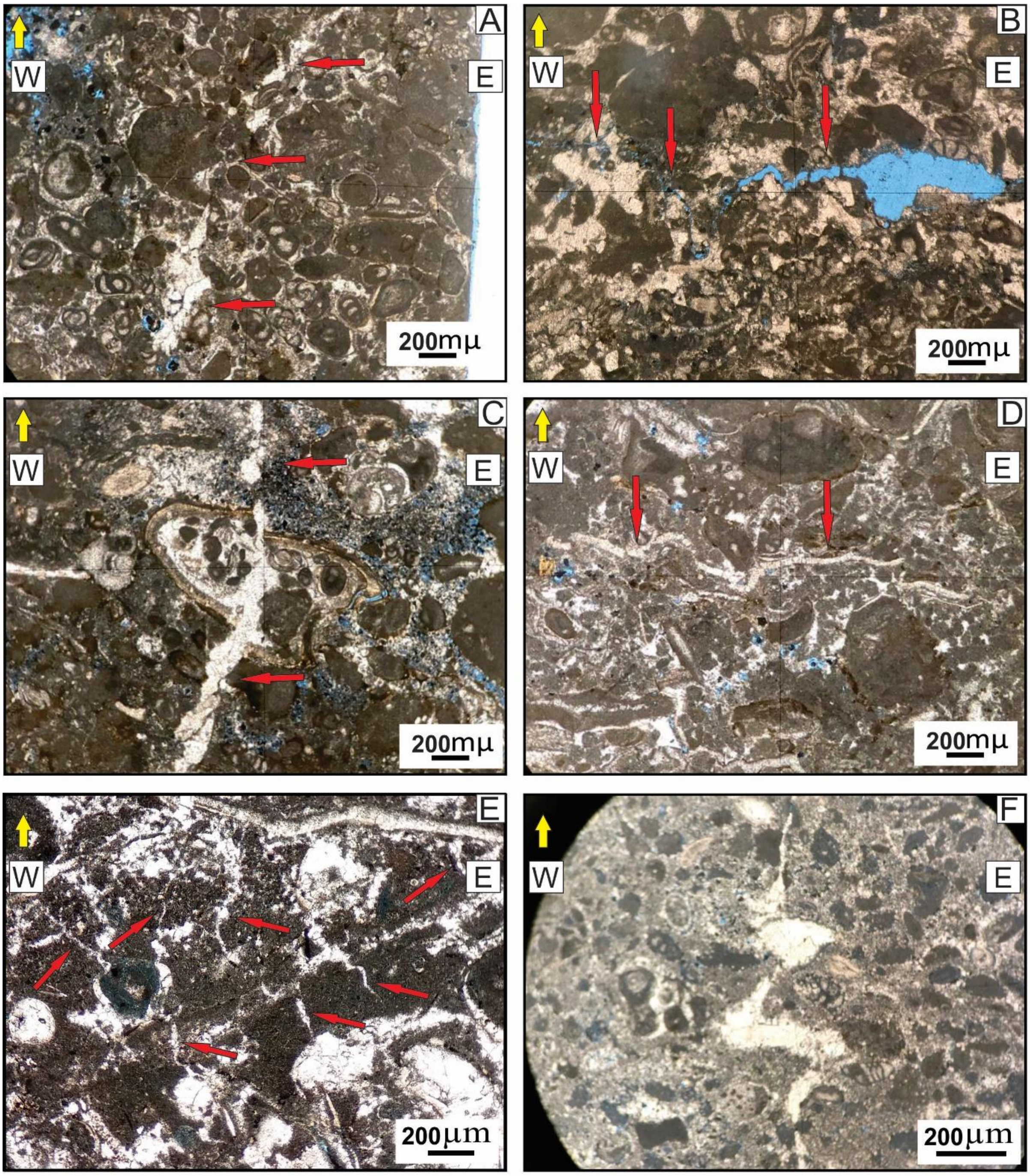

Fig. 4.9 - Microstructural analyses display bed-perpendicular features: (A) stylolites filled with blocky calcite striking ~ NNE-SSW; (B) stylolite filled with microsparry calcite striking ~ E-W; (C) shear veins filled with blocky calcite striking ~ N–S; (D) Disrupted veins filled with fibrous calcite striking ~ ENE-WSW to WNW-ESE; (E) randomly distributed microfractures; (F) moldic pores

connected by N–S microfractures and filled with calcite. Yellow arrows display stratigraphic up. (For interpretation of the references to color in this figure legend, the reader is referred to the Web version of this article.)

Carbonate texture	**Porosity (%)**			**Permeability (mD)**			**Volume of pores at confinant pressure (cm3)**		
	Min.	**Max.**	**Avg.**	**Min.**	**Max.**	**Avg.**	**Min.**	**Max.**	**Avg.**
Mudstone	6.85	13.14	9.99	0.013	4.040	2.020	1.63	1.16	1.39
Packstone	1.42	15.47	8.23	0.00045	2.22	0.11	0.35	12.25	2.25
Grainstone	2.1	16.64	9.1	0.00078	10.57	0.41	0.42	12.25	1.98
Crystalline carbonate	3.44	10.2	6.82	0.005	0.32	0.16	0.83	2.58	1.71
Inside layers	5.23	16.64	9.53	0.009	0.79	0.1	0.84	3.92	1.88
Contact layers	1.42	15.61	8.21	0.00045	10.57	0.5	0.35	12.15	2.16

Table 4.2 - Porosity, permeability, and volume of pores at confining pressure in each carbonate facies, middle portion layers and bedding surfaces in 107 measured plugs

The permeabilities in all carbonate facies range from 0.00078 mD to 10.57 mD (Table 4.2). The permeabilities range from 0.00078 mD to 10.57 mD in grainstones, from 0.00045 mD to 2.22 mD in packstones, from 0.013 mD to 4.04 in mudstones, and range from 0.005 mD to 0.318 mD in crystalline carbonates. The permeabilities along bedding surfaces vary from 0.00045 mD to 10.57 mD and from 0.009 mD to 0.79 mD in the middle portions of layers. On average, grainstones have higher ermeability than packstones while bedding surfaces display higher permeability than the middle portions of layers. Pore volume variations are nearly the same in packstones and grainstones and range from 0.35 to 12.25 cm^3 (Table 4.2). However, the measured pore volume variations along bedding surfaces are much higher than in the middle portions of layers and range from 0.35 to 12.15 cm^3 compared to the values in the middle portions of layers which range from 0.84 to 3.92 cm^3. In all carbonate facies, the average pore volumes along bedding surfaces and in the middle portions of layers are not higher than 3 cm^3.

In the four stratigraphic logs from the Soledade outcrop, porosity (%) versus Klinkenberg permeability (mD) graphs were constructed for each log (Fig. 4.10A) in each bedding surface and in each middle portion the layers in all logs (Fig. 4.10B).

R-squared values indicate that the model explains all the variations in the data around their means. The best trendline option for both parameters is the power law. However, the R-squared value on the chart is below 60% in column 2 (Fig. 4.10A) and along bedding surfaces (Fig. 4.10B) which means that for both cases, less than 60% of the response variation is explained by a linear model. However, the averages of the porosities and permeabilities related to carbonate facies, middle portions of layers, and bedding surfaces range within a few units of each other (Table 4.2).

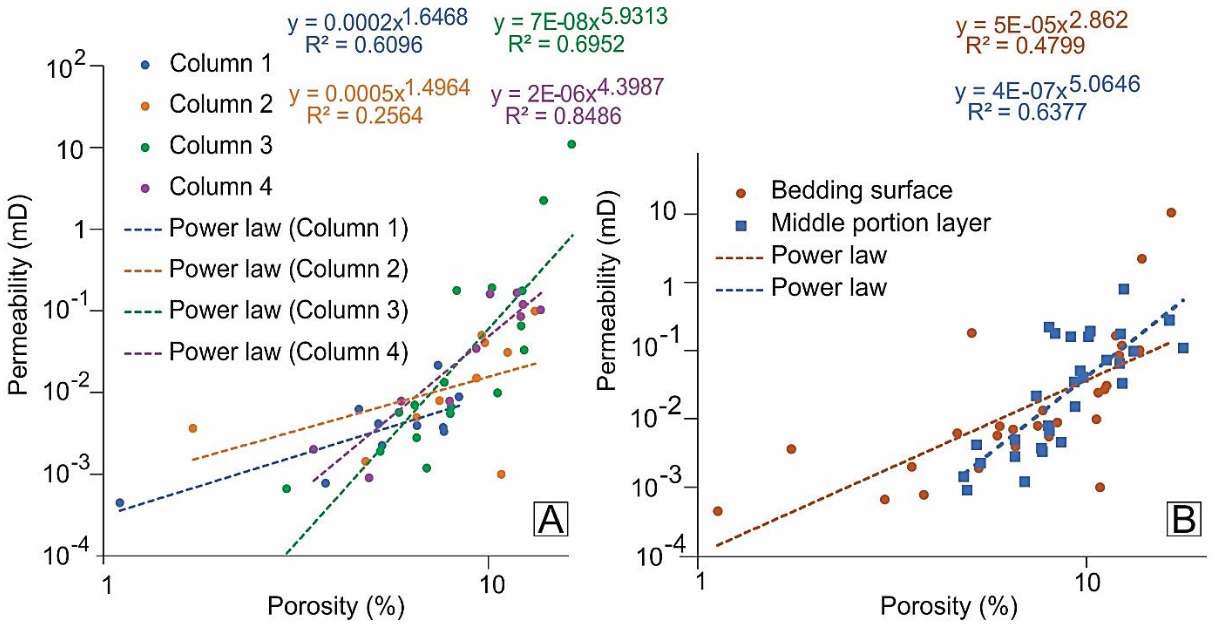

Fig. 4.10 - Log-log diagrams showing the relationship between sample porosity and Klinkenberg corrected permeability of (A) each stratigraphic column and (B) middle portion layers versus bedding surfaces. These two plots show trendlines corresponding to the best fit, power law distribution.

4.4.6 Three-dimensional porosity estimated by plug tomography

Calculated porosities from plugs are divided into four subtypes: stylolite zones (Fig. 4.11A, B, C), microstylolites/fractures (Fig. 4.11D, E, F, and Fig. 4.12A), intragranular dissolution (Fig. 4.12B), and intergranular dissolution (Fig. 4.12C and D).

In all plugs, total porosity ranges from 5% to 32%, connected porosity ranges from 3% to 32%, and isolated porosity ranges from 0.5% to 5%. Isolated porosities are generally constant in all plugs. According to the computed graphs, total porosities are linked to connected porosities and follow the same trend but with different porosity values. Three dissolution types along stylolites are documented (Fig. 4.11A, B and C):

- Plug 1 (Fig. 4.11A): a longitudinal plug view shows an isolated stylolite all along the plug. Total porosity is directly associated with connected porosity because the dissolution along the stylolite and isolated porosity follows a constant trend line.
- Plug 2 (Fig. 4.11B): a longitudinal plug view shows that branched stylolites are very dispersed all along the plug and that the connected porosity is directly associated with dissolution along these stylolite ramifications. At the bottom of the plug, isolated and connected porosities exhibit nearly the same values and the isolated porosity exhibits a constant value toward the top of the plug.
- Plug 3 (Fig. 4.11C): stylolites are concentrated on the left and right sides of the plug without connections between them. At the bottom of the plug, connected

porosity corresponds to total porosity. However, isolated porosities are higher than connected porosities near the top of the plug.

- Plug 4 (Fig. 4.11D): connected porosity is concentrated at the bottom of the plug. In the middle portion of the plug, isolated porosity percentages are lower and increase toward the top.
- Plug 5 (Fig. 4.11E): branched stylolites are dispersed and surround grains all along the plug. The total porosity corresponds to connected porosity along the stylolite ramifications.
- Plug 6 (Fig. 4.11F): connected porosity is related to dissolved stylolites which are evident in the diagonal view. Only the bottom of the plug shows isolated porosity which corresponds to total porosity.
- Plug 1 (Fig. 4.12A): thinner stylolites in the diagonal-longitudinal plug view are connected due to thinner stylolite branches and/or cement dissolution zones. The total porosity is directly associated with connected porosity.
- Plug 2 (Fig. 4.12B): isolated porosity is related to dissolution inside grains, which is called intragranular dissolution. Few intragranular dissolutions are connected and form touching vugs which become connected porosity.
- Plug 3 ((Fig. 4.12C) and plug 4 (Fig. 4.12D): connected porosity is related to dissolution inside cement, which is called intergranular dissolution. Plug 3 is characterized by coarser grain sizes than plug 4, which is the most homogeneous examined plug.

4.4.7 Two-dimensional porosity from drone imagery segmentation

The three-column segments, sections S1, S2 and S3, from the same drone wall images (Fig. 4.1B) show different karstification levels (Fig. 4.13A). Observing Fig. 4.13A, all subsections display different ranges of dissolution. from 2% to 98%. The analyzed subsections showing more than 70% porosity are associated with high-permeability layers (super-k). This interval is displayed in the following subsections: 4 (Fig. 4.13B), 3 (Fig. 4.13C), 5 (Fig. 4.13C), 4 (Fig. 4.13D), and 7 (Fig. 4.13D).

Portions showing touching vugs in different dimensions present porosity ranges from 10% to 55% within sections 1.1 and 1.2 (Fig. 4.13B). These values increase to 70% for sections 2.1, 2.2, 3.1, and 3.2 (Fig. 4.13C and D). Moreover, we documented portions that were characterized by separate vugs. These features show a wide porosity range from 20%

to 40% in sections 1.1 and 1.2 (Fig. 4.13B), approximately 20% in sections 2.1 and 2.2 (Fig. 4.13C), and ~3% in sections 3.1 and 3.2 (Fig. 4.13D).

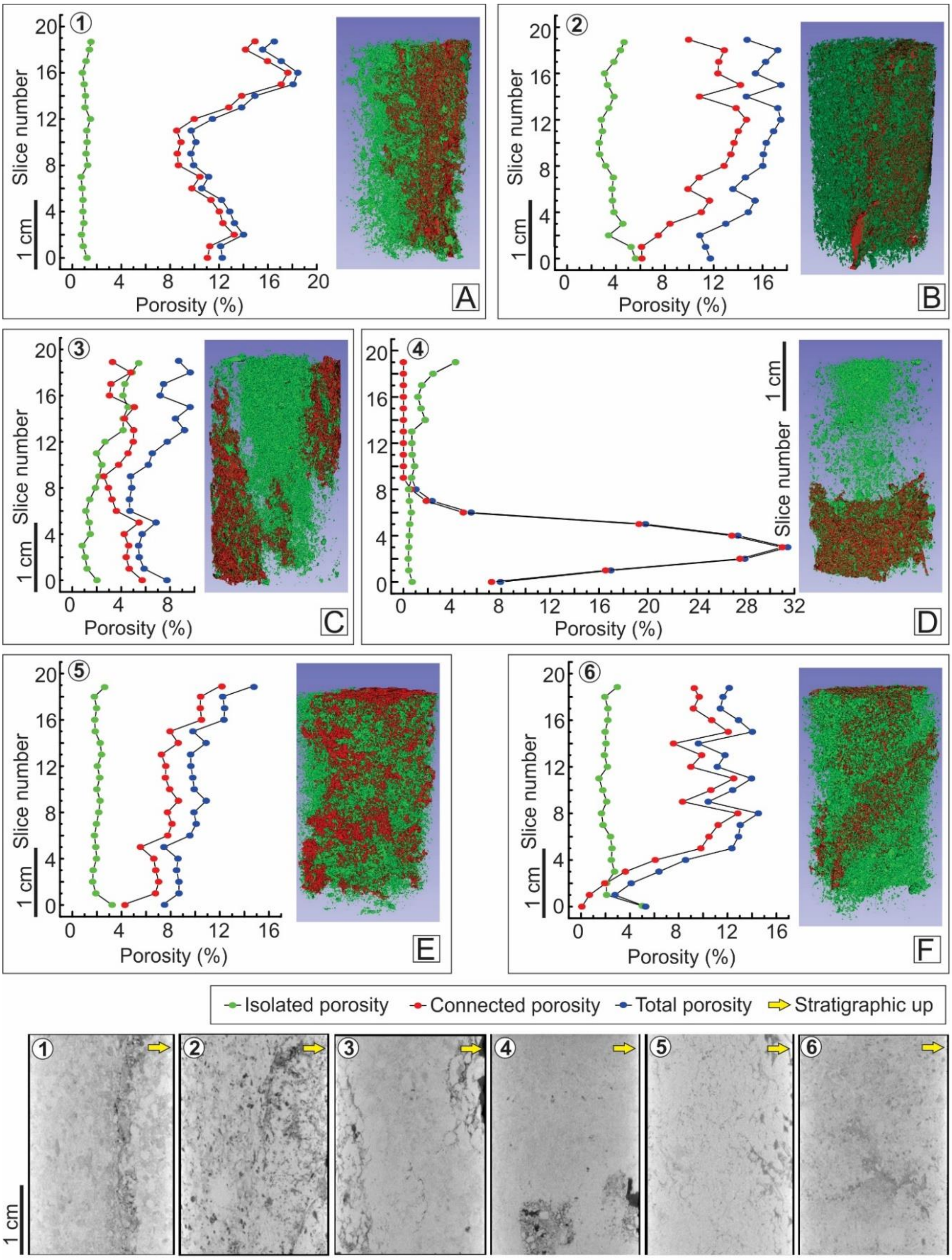

Fig. 4.11 - Plots associated with segmented porosity (isolated, connected, and total pores in green, red, and blue, respectively) from Micro CT longitudinal section image analyses. Stylolite behavior descriptions is associated to different levels of dissolution: (A) stylolite zones; (B) stylolite zone thicker than (A); (C) branched stylolites supporting connected pores on both sides of the plug; (D) very thin branched stylolites concentrated on the bottom of the analyzed plug; (E) branched stylolites surrounding grains; (F) oblique stylolite. (1) to (6) Micro CT images indicate the

corresponding plug above. (For interpretation of the references to color in this figure legend, the reader is referred to the Web version of this article.)

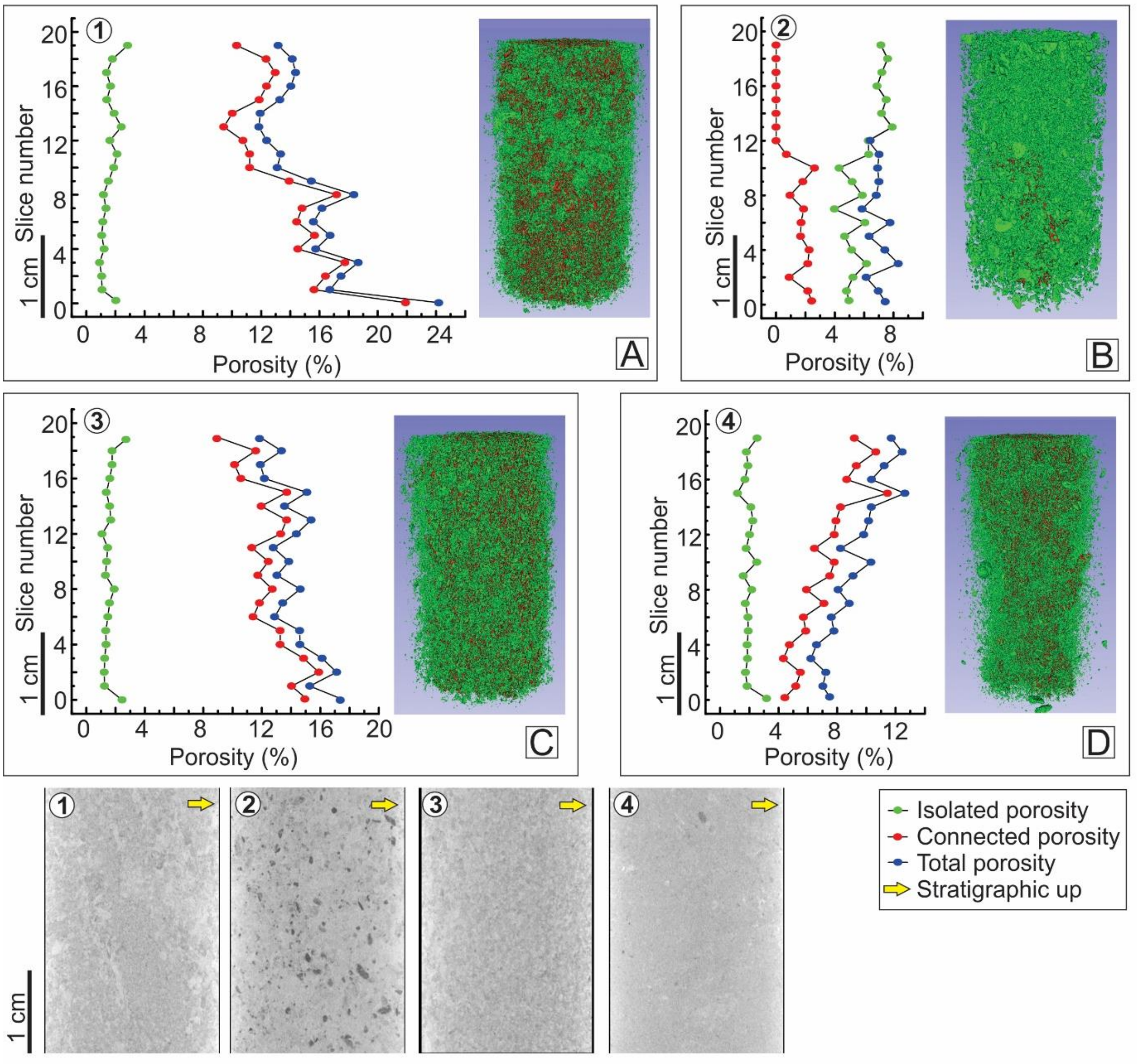

Fig. 4.12 - Plots associated with segmented porosity (isolated, connected, and total pores in green, red and blue, respectively) from Micro CT longitudinal section image analyses. Stylolite behaviors description is associated to different levels of dissolution: (A) very thin stylolite on a diagonal-longitudinal position; (B) dissolution inside grains (intragranular); (C) and (D) dissolution inside cement. (1) to (4) Micro CT images indicate the corresponding plug above. (For interpretation of the references to color in this figure legend, the reader is referred to the Web version of this article.)

4.5 Discussion

Both field and laboratory data obtained for the carbonates that outcrop in the Soledade area are hereafter considered in light of the existing bibliography to discuss the development of stylolites, fractures, and subsequent karstification processes along sedimentary and structural discontinuities.

4.5.1 Classification and organization of stylolites and fractures

a) Bed-parallel stylolites

Ben-Itzhak et al. (2014) categorized bed-parallel stylolites into three connection/percolation geometries which were also observed in our study area: (i) isolated stylolites (Fig. 4.5A, B, E and F); (ii) long stylolite populations with 2D percolation (Fig. 4.5C and D); and (iii) inter-connected stylolite networks characterized by three-dimensional connectivity (Fig. 4.5H). Several studies have reported bed-parallel stylolites, or solution seams, (e.g., Park and Schot, 1968; Renard et al., 2004; Safaricz and Davison, 2005; Schmittbuhl et al., 2004) and inter-connected stylolite networks three-dimensional connectivity (e.g., Eren, 2005; Peacock and Sanderson, 1995; Rye and Bradbury, 1988; Smith, 2000; Rustichelli et al., 2015). Bed-parallel stylolites in the Jandaíra Formation were documented in mudstones (Bertotti et al., 2017), packstones (Fig. 4.5C), grainstones ((Fig. 4.5A), and crystalline carbonates (Fig. 4.7E).

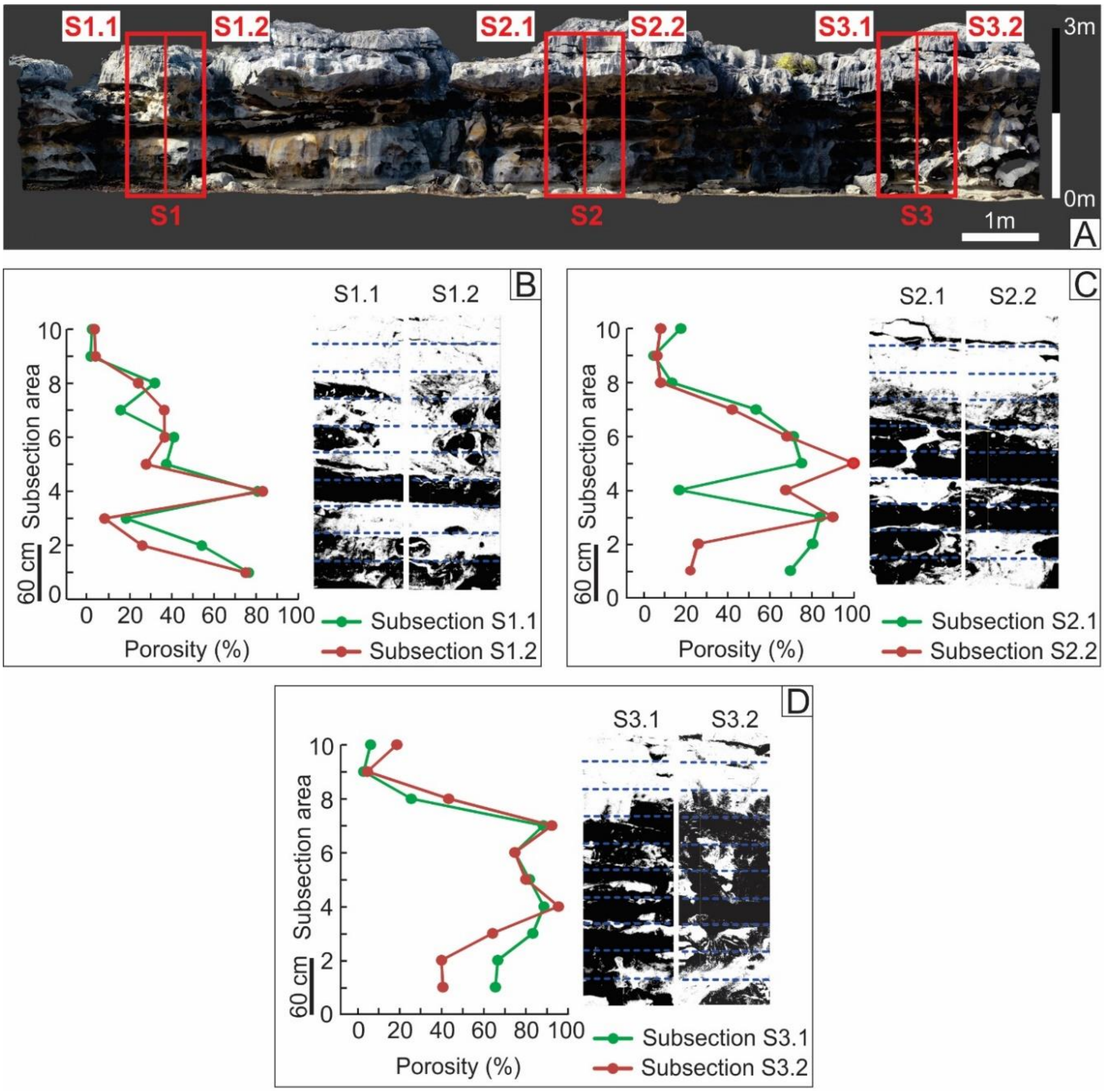

Fig. 4.13 - Drone imagery digital model showing different levels of karst dissolution in three different column segments (S1, S2, and S3): (A) few high permeability layers and more isolated vug pore spaces; (B) intermediate high permeability layers and intermediate isolated vug pore spaces; (C) additional high permeability layers and not isolated vug pore spaces.

According to a new classification based on numerical models and stylolite growth dynamics (Koehn et al., 2016), stylolites from the Soledade outcrop in the Jandaíra Formation can be subdivided into two categories: suture/sharp peak types (Fig. 4.5F and Fig. 4.7E) and mainly simple wave-like types (e.g., Fig. 4.5G and Fig. 4.8E). Simple-wave-like stylolites can represent dissolution seams, and this class could function well as barriers becausethey are not rough and not being offset (Koehn et al., 2016). However, Bagni et al. (2020), Bertotti et al. (2017), and de Graaf et al. (2017) have already documented the above features in the Jandaíra Formation. There, we recorded the association between stylolites and dissolution. This process causes karst dissolution at different scales such as vugular and channel porosity which allow passage of meteoric water along these sub-horizontal conduits (Fig. 4.2 and Fig. 4.6). Moreover, the increase in layer dissolution decreases in layer pinning. However, Beaudoin et al. (2020, 2019) proposed that the suture and sharp peak stylolite types are the most common when approaching the maximum paleo-depth.

b) Bed-perpendicular stylolites and fractures

Bed-perpendicular stylolites, a type of tectonic stylolite which has also been widely documented in the literature (e.g., Bertotti et al., 2017; Nenna and Aydin, 2011; Swennen et al., 2000; Toussaint et al., 2018), are common in the Jandaíra Formation. According to the Koehn et al. (2016) classification, the stylolites in our study area are wave-like type stylolites. Bed-perpendicular stylolites formed and were subsequently reactivated as shear-fractures (Petit and Mattauer, 1995; Salvini et al., 1999; Thomas et al., 2012; Watkinson and Geraghty Ward, 2006) in a mixed dip-slip/strike-slip regime (Rabelo et al., 2020) (e.g., Fig. 4.2B). In addition, two main sets of cross-orthogonal, bed-perpendicular fractures and veins strike ~ N–S and ENE-WSW to WNW-ESE, respectively (Fig. 4.6E and Fig. 4.9C, D). These structures resulted from opening mode fractures which occurred parallel to the principal stress axis (Pollard and Aydin, 1988). Based on their orientation and abutting/crosscutting relationships, we interpret the two fractures/veins sets as having formed under two different stress fields characterized by compression oriented N–S and E-W, respectively (Bezerra et al., 2020; Bezerra and Vita-Finzi, 2000).

4.5.2 Dissolution along sedimentary and structural discontinuities

a) Bed-parallel stylolites

The different porosity types associated with bed-parallel stylolites determined in tomography image segmentation were also documented in thin sections, such as channel and intergranular porosity. Nevertheless, dissolved stylolites are not the only features related to connected porosity. In fact, intergranular porosity sometimes is not detected well in tomography images (Fig. 4.12C and D) because the cements can be less dissolved (Fig. 4.8B). However, some portions that are affected by cement dissolution (Fig. 4.8C) can become pathways for fluid percolation.

As seen in thin sections, channel porosity due to stylolite dissolution takes place progressively through the following processes (Fig. 4.13): (1) stylolites are formed (Fig. 4.7E), (2) isolated vug pores are formed along stylolites, (3) isolated vug pores are still dissolving and reach other isolated pores to create touching vug pores (Fig. 4.8D), (4) touching vug pores are dissolved and linked with other touching vug pores to form channel porosity which represents complete dissolution along these stylolites (Fig. 4.8E), and (5) new, larger isolated pores are generated and form vugular porosity along the dissolved stylolites (Fig. 4.5H). Finally, these processes form high horizontal-permeability (super-k) layers and enlarged vertical conduits and caverns which are observed in outcropping layers (Fig. 4.2 and Fig. 4.13).

The same features were also documented in this area by Bagni et al. (2020), Fernandes et al. (2015), Menezes et al. (2020), Rabelo et al. (2020) and Silva et al. (2017). Nevertheless, none of these studies explained the dissolution along stylolites from the microscale to the outcrop scale. In general, we documented that sedimentary stylolites and structural stylolites are both mainly dissolved at similar grades. However, cementation mainly occurs along structural stylolites playing a fundamental role on the subsequent dissolution processes. In fact, structural stylolites usually display fewer dissolution evidence due to the cement mineralization.

Different karstification levels are observed along the same wall only a few meters distant from each other (Fig. 4.13). Dissolution along sedimentary stylolites, as channel porosity shapes, can appear with different cavity thicknesses. Super permeability (super-k) layers (e.g., Al-Ajmi et al., 2001; Al-Shaalan et al., 2003; Alklih et al., 2014; Cosentino et al., 2001; Meyer et al., 2000; Phelps and Strauss, 2002), which are evident in subsection area 4 (Fig. 4.13A), subsection area 3 and 5 from S2.2 (Fig. 4.13B) and subsection areas 4 to 7 (Fig. 4.13C), are related to dissolution along sedimentary stylolites that become thick-channel porosity (also seen in Fig. 4.2C and D). Differently, thinner channel porosities are observed along bedding surfaces (Fig. 4.2A and B). Finally, vug pore space (for example, on the top of columns S1.1 and S1.2, Fig. 4.13A) along stylolites can be related to intergranular and intragranular porosities. Both porosities are seen, for example, in Fig. 4.8B and A, respectively.

b) Bed-perpendicular stylolites and sedimentary discontinuities

Stratabound and non-stratabound bed-perpendicular stylolites are present in stratigraphic columns 1 and 2 (Fig. 4.3A and B, respectively). Three-dimensional porosity in laboratory tests of plugs shows no significant variations and ranges around 10%. According to several possible mechanisms for the formation of interconnected stylolites (Ben-Itzhak et al., 2014), stratabound and non-stratabound bed-perpendicular isolated stylolites can be connected by increased dissolution and/or connection by bed-parallel stylolites (Fig. 4.6E and F). The same proposed linkage is also possible between bed-perpendicular stylolites and fractures. Both linkage and dissolution processes can cause the formation of narrow caverns (Fig. 4.6I).

The stratifications in the Soledade outcrop includes planar cross-bedding and horizontal planar laminations (Fig. 4.4). These stratifications are related to planar tabular cross-stratification with nontangential foresets (Fig. 4.4C). Observations at the outcrop scale demonstrate how the dissolution processes follows these stratifications (Fig. 4.4A, C, D). This process occurs along planar cross bedding and horizontal planar laminations.

4.5.3 Determination of pore network characteristics based on UCS, 3D porosity, and permeability tests in the laboratory and thin section analysis

Generally, grainstones display slightly higher porosities than packstones. All the stratigraphic logs with their own UCS, porosity and permeability data do not exhibit a definite bedding surface trend because of the following processes: (1) stylolites cannot be dissolved or fully cemented (lower porosity and lower permeability) (Fig. 4.7E); (2) stylolites can be partially dissolved with unconnected pores along their shapes (i.e., separate vugs along stylolites can show high porosity but low permeability and touching vugs along stylolites can show higher permeability but lower porosity) (Fig. 4.8D); (3) stylolites can be fully dissolved to form channel porosity (i.e., high porosity and high permeability) (Fig. 4.8E).

Moreover, UCS, porosity, and permeability values have complex distributions in the studied carbonate succession because (1) there is an absence or very few dissolution of grains in some rock portions (i.e., lower porosity and permeability) (Fig. 4.7D); (2) the non-uniform presence of separate vugs or interparticle vug pores (i.e., high porosity and low permeability) (Fig. 4.8A and C); (3) non-uniform presence of touching vugs (i.e., high porosity with low permeability or low porosity with high permeability) (Fig. 4.8B); and (4) presence of interparticle pore space forming channel porosity (i.e., high porosity and high permeability) (Fig. 4.8F).

The computed power-law distributions of porosity versus permeability in the four stratigraphic logs at the Soledade outcrop imply four trend lines (Fig. 4.10). This does not depend on increases or decreases of porosity and permeability values from their bases to their tops. This aleatory distribution shows that porosity and permeability are mainly related to a secondary dissolution origin, which was also observed in thin sections with different sizes and shapes.

4.5.4 Formation of structural and sedimentary discontinuities and dissolution history

The Jandaíra Formation experienced post-rift tectonics. Since the Campanian, the Potiguar Basin has been affected by two major stress fields (Bezerra et al., 2008; Bezerra and Vita-Finzi, 2000). The results reported in this paper, which were previously discussed on the light of the current bibliography, are now considered to propose the following conceptual model (Fig. 4.14A):

1) Layered carbonates are affected by randomly distributed micro-fractures (Fig. 4.9E) which could be associated with the earliest burial stages or with sporadic desiccation cracks. During this phase, the carbonate rocks were commonly affected by early diagenetic modifications (Anselmetti and Eberli, 1993) which may have increased their stiffness which caused rapid lithification and early embrittlement (La Bruna et al., 2020). At progressively increasing burial depths, these features evolved in both stratabound and non-stratabound opening-mode and shear fractures. In the meantime, the studied carbonates were affected by bed-parallel stylolites (Fig. 4.7E) due to chemical compaction which was associated with more pronounced vertical loading. Previous studies (Bathurst, 1972; Buxton and Sibley, 1981; Dunnington, 1967; Tada and Siever, 1989) have suggested that bed-parallel stylolites in carbonate rocks can form very early during the diagenetic process and can occur at burial depths less than 100 m. Moreover, stylolites can develop continuously with depth (Berger et al., 1993). Rolland et al. (2014) observed stylolites at depths from 150 to 800 m.

2) The stress field, which was characterized by N–S-oriented compression and an E-W-oriented extension (Bezerra et al., 2020; Bezerra and Vita-Finzi, 2000), was associated with sub-horizontal σ_1 and sub-vertical σ_2 (Fig. 4.14A) which generated bed-perpendicular stylolites striking E-W (Fig. 4.9B) and N–S bed-perpendicular fractures (Fig. 4.9C) (Bertotti et al., 2017; de Graaf et al., 2017).
3) The stress field, which consisted of E-W-oriented compression with sub-horizontal σ_1 and sub-vertical σ_2 (Fig. 4.14A), generated N–S bed-perpendicular stylolites (Fig. 4.6E, F, G and Fig. 4.9A) and E-W bed-perpendicular fractures (Fig. 4.9D). These features are often difficult to discern because both features are enlarged by dissolution and lose their distinctive attributes (Fig. 4.6C, D, E and F). Bed-perpendicular fractures and bed-perpendicular stylolites are frequently linked by dissolution and cut across carbonate layers (Fig. 4.14A) (Rabelo et al., 2020). According to Bertotti et al. (2017), the documented fractures were formed at depths ranging from 400 to 500 m.
4) Subsequently, a second sub-vertical compaction (Fig. 4.14A) allowed another formation of randomly distributed micro- fractures, bed-parallel stylolites, and progressive development of both stratabound and non-stratabound opening-mode and shear fractures. At this stage, Bertotti et al. (2017) ascribed the formation of bed-parallel stylolites at depths ranging from ca. 600–850 m based on the Fourier power spectrum method proposed by Schmittbuhl et al. (2004). However, this analysis was done mainly on a few mudstone samples in suture and sharp peak type stylolites. Differently, in our study area, bed-parallel stylolites are present in all carbonate facies except for wackestones, which were not documented on the studied carbonate rocks. The observed stylolites correspond mainly to the simple wave-like type. Based on the stylolite roughness inversion technique, recent work has shown that suture and sharp peak type stylolites affecting packstones could form up to c.a 2200 m depth (Beaudoin et al., 2019).
5) All stylolite and fracture sets were linked by progressive dissolution which was focused along these features and acted across rock layers. Then, dissolution propagated along stylolites, fractures, and sedimentary surfaces (Fig. 4.14A). Mesoscale structures, such as stylolites, veins, and open fractures, can be first-order indicators of primary fluid flow which trended N–S to NNE-SSW and E-W to ENE-WSW in the carbonate rocks of the Jandaíra Formation (Rabelo et al., 2020). Analyses performed on calcite veins and host rock cements, for the

aforementioned fluid flow passages, suggest a depth formation ranging between 400 and 900 m during the Late Cretaceous to Early Cenozoic (de Graaf et al., 2017).

6) Dissolution along bed-perpendicular fractures, stylolites, and cross stratifications expanded progressively over time (Fig. 4.14A). Stylolite enlargement by acidic meteoric waters generated karst dissolution features such as vugs, channels, and caverns. By analyzing stylolites at microscales, channel porosity due to stylolite dissolution occurred in the following process (Fig. 4.14B): (1) stylolites formed due to pressure solution on grain contacts; (2) isolated pores formed along stylolites; (3) isolated pores, still dissolving, reached other isolated pores to form touching pores and after that, channel porosity; (4) channel porosity expanded progressively to represent completely dissolved stylolites; and (5) new or enlarged pores formed along channel porosity overprinted on former stylolites.

Moreover, dissolution along planar cross bedding and horizontal planar laminations was controlled by differences in grain size and/or cementation (Fig. 4.14C). Different cementation grades can also be related to grain size which suggests that meteoric water can percolate along most dissolved cements and fine-grained portions of rocks while less dissolved cement which is coarse-grained, act as barriers to fluid percolation. This process can explain why dissolution along stratifications, which was also observed in thin sections, can form channel porosity up to a few meters thick.

Both structural discontinuities (e.g.,bed-perpendicular stylolites and bed-perpendicular fractures) and sedimentary discontinuities (e.g., bed-parallel stylolites and cross stratifications) controlled the localization of dissolution cavities since (1) bed-parallel stylolites formed along bedding surfaces, (2) bed-parallel stylolites dissolved due to water percolation along bedding surfaces, and (3) bed-perpendicular fractures and bed-perpendicular stylolites dissolved together and cut across layers and contributed to water percolation into the underlying rock layers and bed-parallel and bed-perpendicular discontinuities.

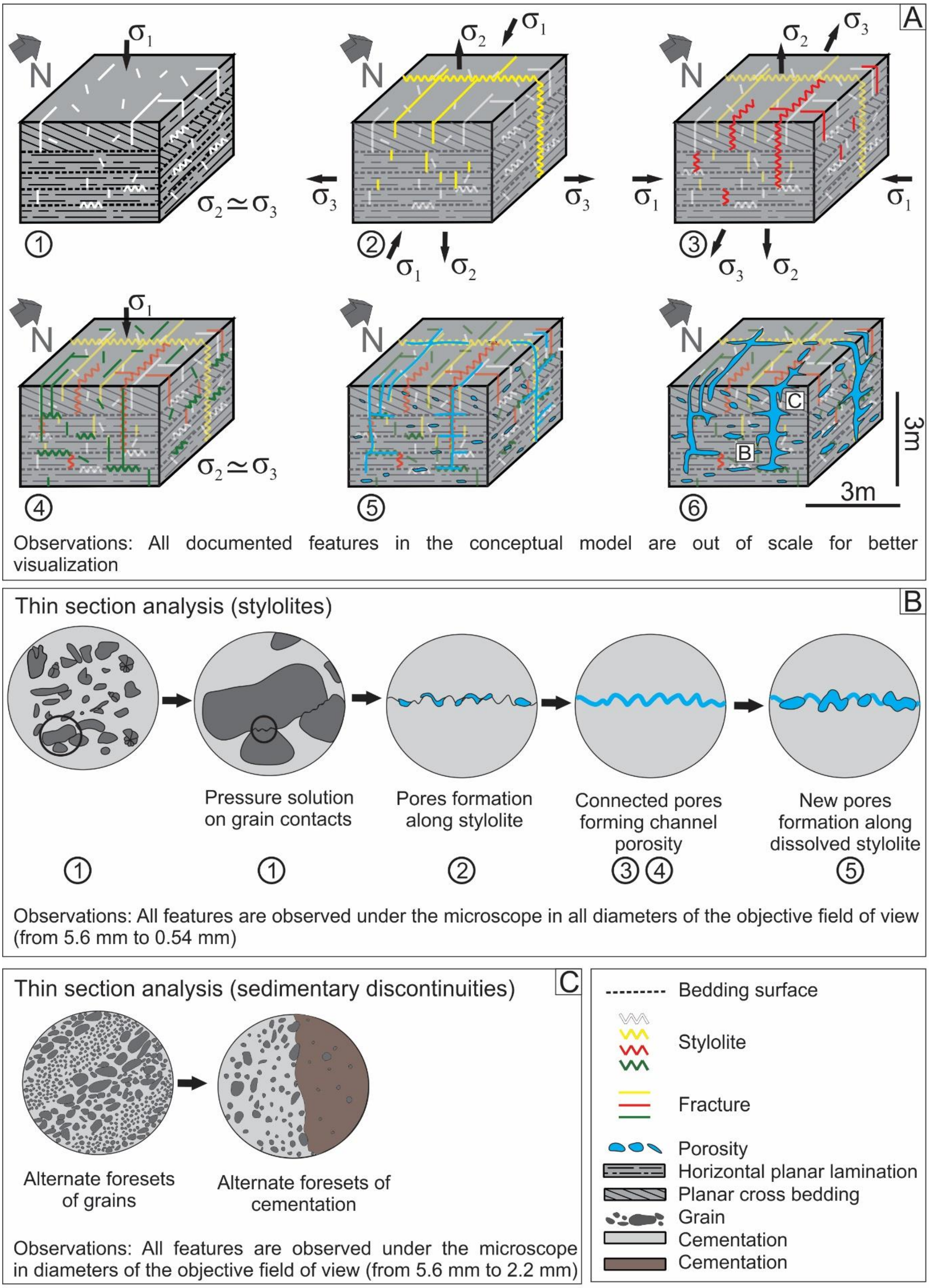

Fig. 4.14 - Evolutionary conceptual model showing the origin and evolution of vuggy pore space and karst features during and following subsidence: (1) carbonates layers showing stratifications were deposited; bed-perpendicular fractures and bed-parallel stylolites were formed by a sub-vertical compaction; (2) N–S bed- perpendicular fractures and E-W bed-

perpendicular stylolites were formed under sub-horizontal compression; (3) N–S bed-perpendicular stylolites and E-W fractures were formed by a sub-horizontal compression; (4) sub-vertical compaction generate bed-perpendicular fractures and bed-parallel stylolites, which were connected along bed boundaries; (5) bed-perpendicular fractures and stylolites were linked by dissolution cross cutting all the layers; dissolution also occurred along cross stratifications. (6) Dissolution along fractures, stylolites, and cross stratifications were expanded. (B) Analyzing stylolites at microscale, channel porosity due to stylolite dissolution takes place in the following process: (1) stylolite are formed due to pressure solution on grain contacts; (2) isolated pores are formed along stylolite; (3) isolated pores, still dissolving, reach another isolated pore to form touching pores and thereafter channel porosity; (4) channel porosity expands progressively up to represent completely dissolved stylolites; (5) new or enlarged pores are formed along channel porosity overprinted on former stylolites. (C) Dissolution along planar cross-bedding and horizontal planar lamination are related to alternate foresets of grains or cementation.

4.6 Conclusions

The present study combined field and laboratory analyses to characterize the nature, distribution, and development of stylolites, fractures, and primary discontinuities and focused on the karst dissolution processes that affected the Cretaceous carbonate rocks of the Jandaíra Formation at the Soledade outcrop, Potiguar Basin, northeastern Brazil.

Specifically, we reached the following conclusions:

1) Karst dissolution cavities (vugs, channels, and caverns) follow both structural discontinuities (e.g., bed-perpendicular stylolites and bed-perpendicular fractures) and sedimentary discontinu- ities (e.g., cross stratifications and superimposed bed-parallel stylolites). The evidence of dissolution processes affecting cross stratification proves the absence of paleo-water levels control.
2) Bed-perpendicular stylolites are either stratabound or not stra- tabound. Both stylolite types are enlarged by dissolution and can crosscut layers and thereby form vertical narrow caverns.
3) The absence of dissolution along some bed-parallel stylolites can provide barriers to horizontal fluid flow. However, bed-parallel dissolved stylolites can contribute to fluid percolation and form channel porosity along with them.
4) Stylolites can be isolated or branched. Both stylolite types can form stylolite zones and the total porosity is therefore related to a higher percentage of connected dissolution porosity along the stylolite zone.
5) Thin sections show isolated pore space formation along non-dissolved stylolites. These isolated pores were, in some cases, enlarged to form channel porosity along some stylolites. New pores can originate along channel porosity which becomes larger. This process explains the genesis of karst dissolution features which evolve into vertical conduits (bed-perpendicular enlarged fractures and stylolites), high

permeability layers (bed-parallel stylolite enlargements) and, in the advanced stage, caverns.

6) Dissolution along stratifications such as horizontal planar laminations and planar cross bedding is a function of different grain sizes and/or cementation grades in different foresets.

The results above led to the formulation of an evolutionary conceptual model of dissolution along structural and sedimentary discontinuities.

Layered carbonates were affected by bed-parallel stylolites and randomly distributed microfractures originated from compaction and were associated with vertical upload (overburden); E-W and N–S bed- perpendicular stylolites and fractures were formed by sub-horizontal compression. Both stylolite sets were linked by dissolution which cut across layers and then by dissolution along sedimentary stylolites and cross stratifications began; dissolution along cross stratifications, bed- parallel stylolites, bed-perpendicular stylolites, and fractures progressively expanded.

These complex and articulated dissolution processes affected the study area, profoundly modified, and partially obliterated the original rock sequence configuration. However, the results presented in this work shed new light on the control exerted by structural and primary sedimentary discontinuities which affects carbonate rocks for the formation of dissolution cavities that frequently affect currently exploited carbonate reservoirs.

Further analysis focused on diagenetic sequence characterization of the studied carbonate sequence is required to better understand the role played by dissolution processes along cements and grains.

Credit authorship contribution statement

Renata E.B. Araújo: Conceptualization, Methodology, Writing - original draft, Writing - review & editing, Software, Data curation, Investigation, Validation. **Vincenzo La Bruna:** Conceptualization Methodology, Writing - original draft, Writing - review & editing, Data curation, Investigation, Validation, Supervision. **Andrea Rustichelli:** Writing - original draft, Writing - review & editing, Data curation, Validation. **Francisco H.R. Bezerra:** Conceptualization, Methodology, Writing - original draft, Writing - review & editing, Data curation, Investigation, Validation, Funding acquisition, Supervision. **Milton M. Xavier:** Writing - review & editing, Software, Data curation, Investigation, Validation. **Philippe Audra:** Writing - review & editing, Data curation, Validation. **José**

A. Barbosa: Writing - review & editing, Investigation, Validation. **Antônio C.D. Antonino:** Writing - review & editing, Investigation, Validation.

Declaration of competing interest

The authors declare that they have no known competing financial interests or personal relationships that could have appeared to influence the work reported in this paper.

Acknowledgements

We thank two anonymous reviewers and the associate editor, Nicolas Beaudoin, for their detailed and constructive reviews, which significantly improved the quality of the present work. This research was carried out in association with the ongoing R&D project registered as ANP 20502–1, “Processos e Propriedades em Reservartórios Carbonáticos Fraturados e Carstificados – POROCARSTE 3D” (UFRN / UNB / UFRJ / UFC / Shell Brasil / ANP) – Porokarst – Processes and Properties in Fractured and Karstified Carbonate Reservoirs, sponsored by Shell Brasil under the ANP R&D levy as “Compromisso de Investimento com Pesquisa e Desenvolvimento”.

Appendix A. Supplementary data

Supplementary data to this article can be found online at https://doi.org/10.1016/j.marpetgeo.2020.104753.

References

Agosta, F., Alessandroni, M., Antonellini, M., Tondi, E., Giorgioni, M., 2010. From fractures to flow: A field-based quantitative analysis of an outcropping carbonate reservoir. Tectonophysics 490, 197–213. https://doi.org/10.1016/j.tecto.2010.05.005

Angelim, L.D.A., Nesi, J.R., Torres, H. H. F., Medeiros, V.C., Santos, C.A., Veiga Junior, J.P., Mendes, V.A., 2006. Geologia e recursos minerais do Estado do Rio Grande do Norte-Escala 1: 500.000, Recife: CPRM-Serviço Geológico do Brasil.

Anselmetti, F.S., Eberli, G.P., 1999. The Velocity-Deviation Log: A Tool to Predict Pore Type and Permeability Trends in Carbonate Drill Holes from Sonic and Porosity or Density Logs. Am. Assoc. Pet. Geol. Bull. 83, 450–466. https://doi.org/10.1306/00AA9BCE-1730-11D7-8645000102C1865D

Anselmetti, F.S., Eberli, G.P., 1993. Controls on sonic velocity in carbonates. Pure Appl. Geophys. PAGEOPH 141, 287–323. https://doi.org/10.1007/BF00998333

Aquilina, L., Ladouche, B., Doerfliger, N., Bakalowicz, M., 2003. Deep water circulation, residence time, and chemistry in a karst complex. Ground Water 41, 790–806.

Araújo, R.E.B., La Bruna, V., Rustichelli, A., Bezerra, F.H.R., Xavier, M.M., Audra, P., Barbosa, J.A., Antonino, A.C.D., 2021. Structural and sedimentary discontinuities control the generation of karst dissolution cavities in a carbonate sequence, Potiguar Basin, Brazil. Mar. Pet. Geol. 123. https://doi.org/10.1016/j.marpetgeo.2020.104753

Aydin, A., 2008. ISRM suggested method for determination of the Schmidt hammer rebound hardness: revised version, in: The ISRM Suggested Methods for Rock Characterization, Testing and Monitoring: 2007-2014. Springer, Cham, pp. 25–33. https://doi.org/10.1007/978-3-319-07713-0_2

Aydin, A., Basu, A., 2005. The Schmidt hammer in rock material characterization. Eng. Geol. 81, 1–14. https://doi.org/10.1016/j.enggeo.2005.06.006

Back, W., Hanshaw, B.B., Pyle, T.E., Plummer, L.N., Weidie, A.E., 1979. Geochemical significance of groundwater discharge and carbonate solution to the formation of Caleta Xel Ha, Quintana Roo, Mexico. Water Resour. Res. 15, 1521–1535. https://doi.org/10.1029/WR015i006p01521

Bagni, F.L., Bezerra, F.H., Balsamo, F., Maia, R.P., Dall'Aglio, M., 2020. Karst dissolution along fracture corridors in an anticline hinge, Jandaíra Formation, Brazil: Implications for reservoir quality. Mar. Pet. Geol. 115, 104249. https://doi.org/10.1016/j.marpetgeo.2020.104249

Bagni, F.L., Erthal, M.M., Tonietto, S.N., Maia, R.P., Bezerra, F.H., Balsamo, F., Córdoba, V.C., de Souza, F.G., Brod, J.A., Fernandes, C.P., Fonseca, J.P.T., 2022. Karstified layers and caves formed by superposed epigenic dissolution along subaerial unconformities in carbonate rocks – Impact on reservoir-scale permeability. Mar. Pet. Geol. 138, 105523. https://doi.org/10.1016/j.marpetgeo.2022.105523

Balsamo, F., Bezerra, F.H.R., Klimchouk, A.B., Cazarin, C.L., Auler, A.S., Nogueira, F.C., Pontes, C., 2020. Influence of fracture stratigraphy on hypogene cave development and fluid flow anisotropy in layered carbonates, NE Brazil. Mar. Pet. Geol. 114, 104207. https://doi.org/10.1016/j.marpetgeo.2019.104207

Bergen, D.V., Carozzi, A.V., 1990. Experimentally-simulated stylolitic porosity in carbonate rocks. J. Pet. Geol. 13, 179–192. https://doi.org/10.1111/j.1747-5457.1990.tb00838.x

Bertotti, G., de Graaf, S., Bisdom, K., Oskam, B., Vonhof, H.B., Bezerra, F.H.R., Reijmer, J.J.., Cazarin, C.L., 2017. Fracturing and fluid-flow during post-rift subsidence in carbonates of the Jandaíra Formation, Potiguar Basin, NE Brazil. Basin Res. 29, 836–853. https://doi.org/10.1111/bre.12246

Bezerra, F.H.R., Brito Neves, B.B., Corrêa, A.C.B., Barreto, A.M.F., Suguio, K., 2008. Late Pleistocene tectonic-geomorphological development within a passive margin - The Cariat?? trough, northeastern Brazil. Geomorphology 97, 555–582. https://doi.org/10.1016/j.geomorph.2007.09.008

Bezerra, F.H.R., de Castro, D.L., Maia, R.P., Sousa, M.O.L., Moura-Lima, E.N., Rossetti, D.F., Bertotti, G., Souza, Z.S., Nogueira, F.C.C., 2020. Postrift stress field inversion in the Potiguar Basin, Brazil – Implications for petroleum systems and evolution of the equatorial margin of South America. Mar. Pet. Geol. 111, 88–104. https://doi.org/10.1016/j.marpetgeo.2019.08.001

Bezerra, F.H.R., Vita-Finzi, C., 2000. How active is a passive margin? Paleoseismicity in northeastern Brazil. Geology 28, 591. https://doi.org/10.1130/0091-7613(2000)28<591:HAIAPM>2.0.CO;2

Bloch, S., 1994. Secondary porosity in sandstones: significance, origin, relationship to subaerial unconformities, and effect on predrill reservoir quality prediction. Soc. Sediment. Geol. 137–159.

Boggs, S.J., 1992. Petrology of Sedimentary Rocks. New York, Macmillan Publishing Co.

Byrnes, A.P., 1994. Measurement of Dependent Variables –Petrophysical Variables, in: Reservoir Quality Assessment and Prediction in Clastic Rocks. SEPM (Society for Sedimentary Geology), pp. 231–246. https://doi.org/10.2110/scn.94.30.0231

Carlotto, M.A., Da Silva, R.C.B., Yamato, A.A., Trindade, W.L., Moreira, J.L.P., Fernandes, R.A.R., Ribeiro, O.J.S., Gouveia, W.P., Carminati, J.P., Qicai, D., Junfeng, Z., Da Silva-Telles, A.C., 2017. Libra: A newborn giant in the brazilian presalt province, in: AAPG Memoir. American Association of Petroleum Geologists, pp. 165–176. https://doi.org/10.1306/13572006M1133685

Carneiro, M.A., Bezerra, F.H.R., Silva, C.C.N. da, Maia, R.P., Cazarin, C.L., 2015. Controle estrutural do sistema cárstico epigenético na Formação Jandaíra, Bacia Potiguar. Geociências (São Paulo) 34, 199–209.

Carozzi, A. V., Bergen, D. Von, 1987. Stylolitic porosity in carbonates: a critical factor for deep hydrocarbon production. J. Pet. Geol. 10, 267–282. https://doi.org/10.1111/j.1747-5457.1987.tb00946.x

Cazarin, C. L., Bezerra, F.H.R., Borghi, L., Santos, R. V., Favoreto, J., Brod, J.A., Auler, A.S., Srivastava, N.K., 2019. The conduit-seal system of hypogene karst in Neoproterozoic carbonates in northeastern Brazil. Mar. Pet. Geol. 101, 90–107. https://doi.org/10.1016/j.marpetgeo.2018.11.046

Cazarin, Caroline L., Bezerra, F.H.R., Borghi, L., Santos, R. V., Favoreto, J., Brod, J.A., Auler, A.S., Srivastava, N.K., 2019. The conduit-seal system of hypogene karst in Neoproterozoic carbonates in northeastern Brazil. Mar. Pet. Geol. 101, 90–107. https://doi.org/10.1016/j.marpetgeo.2018.11.046

Chafetz, H., Barth, J., Cook, M., Guo, X., Zhou, J., 2018. Origins of carbonate spherulites: Implications for Brazilian Aptian pre-salt reservoir. Sediment. Geol. 365, 21–33. https://doi.org/10.1016/j.sedgeo.2017.12.024

Choquette, P.W., James, N.P., 1987. Diagenesis# 12. Diagenesis in Limestones -3. The deep burial environment. Geosci. Canada 14, 3–35.

Choquette, P.W., Pray, L.C., 1970. Geologic Nomenclature and Classification of Porosity in Sedimentary Carbonates. Am. Assoc. Pet. Geol. Bull. 54, 207–250. https://doi.org/10.1306/5D25C98B-16C1-11D7-8645000102C1865D

de Castro, D.L., Bezerra, F.H.R., Sousa, M.O.L., Fuck, R.A., 2012. Influence of Neoproterozoic tectonic fabric on the origin of the Potiguar Basin, northeastern Brazil and its links with West Africa based on gravity and magnetic data. J. Geodyn. 54, 29–42. https://doi.org/10.1016/J.JOG.2011.09.002

de Graaf, S., Reijmer, J.J.G., Bertotti, G. V., Bezerra, F.H.R., Cazarin, C.L., Bisdom, K., Vonhof, H.B., 2017. Fracturing and calcite cementation controlling fluid flow in the shallow-water carbonates of the Jandaíra Formation, Brazil. Mar. Pet. Geol. 80, 382–393. https://doi.org/10.1016/j.marpetgeo.2016.12.014

Dunham, R.J., 1962. Classification of Carbonate Rocks According to Depositional Textures, in: Classification of Carbonate Rocks According to Depositional Textures. AAPG Special Volumes, pp. 108–121.

Embry, A.F., Klovan, J.E., 1971. A Late Devonian reef tract on north-eastern Banks Island. Bull. Can. Pet. Geol. 19, 730–781. https://doi.org/10.35767/gscpgbull.19.4.730

Esteban, M., Wilson, J.L., 1993. Introduction to Karst Systems and Paleokarst Reservoirs, in: Introduction to Karst System and Paleokarst Reservoirs. Special Publications of

SEPM, pp. 1–9.

Fairbridge, R.W., 1967. Phases of Diagenesis and Authigenesis, in: Developments in Sedimentology. pp. 19–89. https://doi.org/10.1016/S0070-4571(08)70841-0

Fernandes, A.L., Medeiros, W.E., Bezerra, F.H.R., Oliveira, J.G., Cazarin, C.L., 2015. GPR investigation of karst guided by comparison with outcrop and unmanned aerial vehicle imagery. J. Appl. Geophys. 112, 268–278. https://doi.org/10.1016/j.jappgeo.2014.11.017

Flügel, E., 2010. Microfacies of Carbonate Rocks, Second edi. ed. Springer Berlin Heidelberg, Berlin, Heidelberg. https://doi.org/10.1007/978-3-642-03796-2

Folk, R.L., 1974. The Natural History Of Crystalline Calcium Carbonate: Effect of Magnesium Content And Salinity. J. Sediment. Res. 44, 40–53. https://doi.org/10.1306/74D72973-2B21-11D7-8648000102C1865D

Folk, R.L., 1965. Some aspects of recrystallization in ancient limestones. SEPM Spec. Publ. 13, 14–48.

Ford, D., 1988. Characteristics of Dissolutional Cave Systems in Carbonate Rocks, in: Paleokarst. Springer New York, New York, NY, pp. 25–57. https://doi.org/10.1007/978-1-4612-3748-8_2

Ford, D., Williams, P., 2007. Karst Hydrogeology and Geomorphology. John Wiley & Sons Ltd,., West Sussex, England. https://doi.org/10.1002/9781118684986

Ford, D.C., Williams, P.W., 2013. Karst geomorphology and hydrology, Second edi. ed. John Wiley & Sons.

Friedman, G.M., 1964. Early Diagenesis and Lithification in Carbonate Sediments. SEPM J. Sediment. Res. 34, 777–813. https://doi.org/10.1306/74D71195-2B21-11D7-8648000102C1865D

Fu, Q., 2006. Paleokarst in Middle Devonian Winnipegosis mud mounds, subsurface of south-central Saskatchewan, Canada. Bull. Can. Pet. Geol. 54, 22–36. https://doi.org/10.2113/54.1.22

Ganai, J.A., Rashid, S.A., Romshoo, S.A., 2018. Evaluation of terrigenous input, diagenetic alteration and depositional conditions of Lower Carboniferous carbonates of Tethys Himalaya, India. Solid Earth Sci. 3, 33–49. https://doi.org/10.1016/j.sesci.2018.03.002

Garcia, G., 2014. Modelagem estratigráfica do intervalo cenomaniano-turoniano, formações Açu e Jandaíra, na borda sudoeste da Bacia Potiguar. Universidade Estadual Paulista.

Giuffrida, A., Agosta, F., Rustichelli, A., Panza, E., La Bruna, V., Eriksson, M., Torrieri, S., Giorgioni, M., 2020. Fracture stratigraphy and DFN modelling of tight carbonates, the case study of the Lower Cretaceous carbonates exposed at the Monte Alpi (Basilicata, Italy). Mar. Pet. Geol. 112, 104045. https://doi.org/10.1016/j.marpetgeo.2019.104045

Giuffrida, A., La Bruna, V., Castelluccio, P., Panza, E., Rustichelli, A., Tondi, E., Giorgioni, M., Agosta, F., 2019. Fracture simulation parameters of fractured reservoirs: Analogy with outcropping carbonates of the Inner Apulian Platform, southern Italy. J. Struct. Geol. 123, 18–41. https://doi.org/10.1016/j.jsg.2019.02.007

Goldberg, K., Kuchle, J., Scherer, C., Alvarenga, R., Ene, P.L., Armelenti, G., De Ros, L.F., 2017. Re-sedimented deposits in the rift section of the Campos Basin. Mar. Pet. Geol. 80, 412–431. https://doi.org/10.1016/j.marpetgeo.2016.11.022

Goldscheider, N., Drew, D., 2007. Methods in Karst Hydrogeology, in: IAH: International Contributions to Hydrogeology, 26. CRC Press/Balkema, Taylor & Francis Group. pp.

9–23.

Gutiérrez, F., Fabregat, I., Roqué, C., Carbonel, D., Zarroca, M., Linares, R., Yechieli, Y., García-Arnay, Á., Sevil, J., 2019. Sinkholes in hypogene versus epigene karst systems, illustrated with the hypogene gypsum karst of the Sant Miquel de Campmajor Valley, NE Spain. Geomorphology 328, 57–78. https://doi.org/10.1016/j.geomorph.2018.12.003

Hackspacher, P.C., Corsino, A.R., Srivastava, N.K., Tiriba, V.F., 1985. A Falha de Afonso Bezerra como evidência de significativo tectonismo frágil NW-SE, na Bacia Potiguar emersa – RN. Bol. do Dep. Geol. 10, 33–44.

Hajikazemi, E., Al-Aasm, I.S., Coniglio, M., 2010. Subaerial exposure and meteoric diagenesis of the Cenomanian-Turonian Upper Sarvak Formation, southwestern Iran. Geol. Soc. London, Spec. Publ. 330, 253–272. https://doi.org/10.1144/SP330.12

Hallenberger, M., Reuning, L., Schoenherr, J., 2018. Dedolomitization Potential of Fluids from Gypsum-to-Anhydrite Conversion: Mass Balance Constraints from the Late Permian Zechstein-2-Carbonates in NW Germany. Geofluids 2018, 1–9. https://doi.org/10.1155/2018/1784821

Hanshaw, B.B., Back, W., Deike, R.G., 1971. A geochemical hypothesis for dolomitization by ground water. Econ. Geol. 66, 710–724. https://doi.org/10.2113/gsecongeo.66.5.710

Hayer, J.B., 1979. Sandstone diagenesis - The hole truth. Soc. Econ. Paleontol. Mineral. 26, 127–139.

He, L., Zhao, L., Li, J., Ma, J., Lui, R., Wang, S., Zhao, W., 2014. Complex relationship between porosity and permeability of carbonate reservoirs and its controlling factors: A case study of platform facies in Pre-Caspian Basin. Pet. Explor. Dev. 41, 225–234. https://doi.org/10.1016/S1876-3804(14)60026-4

Heald, M.T.H., Larese, R.E., 1973. The Significance of the Solution of Feldspar in Porosity Development. SEPM J. Sediment. Res. 43, 458–460. https://doi.org/10.1306/74D72798-2B21-11D7-8648000102C1865D

Heap, M., Reuschlé, T., Baud, P., Renard, F., Iezzi, G., 2018. The permeability of stylolite-bearing limestone. J. Struct. Geol. 116, 81–93. https://doi.org/10.1016/j.jsg.2018.08.007

Herlinger, R., Zambonato, E.E., De Ros, L.F., 2017. Influence of Diagenesis On the Quality of Lower Cretaceous Pre-salt Lacustrine Carbonate Reservoirs from Northern Campos Basin, Offshore Brazil. J. Sediment. Res. 87, 1285–1313. https://doi.org/10.2110/jsr.2017.70

Heward, A.P., Chuenbunchom, S., Mäkel, G., Marsland, D., Spring, L., 2000. Nang Nuan oil field, B6/27, Gulf of Thailand: Karst reservoirs of meteoric or deep-burial origin? Pet. Geosci. 6, 15–27. https://doi.org/10.1144/petgeo.6.1.15

Hill, C.A., 1995. H2S-Related Porosity and Sulfuric Acid Oil-Field Karst. Am. Assoc. Pet. Geol. Bull. 74, 1685–1694.

Hopkins, J.C., 1999. Characterization of Reservoir Lithologies within Subunconformity Pools: Pekisko Formation, Medicine River Field, Alberta, Canada. Am. Assoc. Pet. Geol. Bull. 83, 1855–1870. https://doi.org/10.1306/E4FD4283-1732-11D7-8645000102C1865D

James, N.P., Choquette, P.W., 1988. Paleokarst. Springer-Verlag New York. https://doi.org/10.1007/978-1-4612-3748-8

James, N.P., Choquette, P.W., 1984. Limestones - the meteoric diagenetic environment.

Geosci. Canada 11, 161–194. https://doi.org/10.1029/sc004p0045

James, N.P., Choquette, P.W., 1983. Diagenesis 6. Limestones — The Sea Floor Diagenetic Environment. Geosci. Canada 10, 162–179.

Jiu, B., Huang, W., Mu, N., Li, Y., 2021. Types and controlling factors of ordovician paleokarst carbonate reservoirs in the southeastern Ordos Basin, China. J. Pet. Sci. Eng. 198, 108162. https://doi.org/10.1016/j.petrol.2020.108162

Jonas, E.C., McBride, E.F., 1977. Diagenesis of sandstone and shale: application to exploration for hydrocarbons: Continuing Education Program Publication 1. Dep. Geol. Sci. Univ. Texas Austin, Austin, Texas. 165.

Klimchouk, A., 2012. Speleogenesis, hypogenic, in: Encyclopedia of Caves. pp. 748–765.

Klimchouk, A., Palmer, A.N., Waele, J. De, Auler, A.S., Audra, P., 2017. Hypogene karst regions and caves of the world. Springer.

Klimchouk, A.B., Ford, D.C., 2000. Types of karst and evolution of hydrogeologic setting, Speleogenesis. Evolution of Karst Aquifers. Huntsville: National Speleological Society.

La Bruna, V., Agosta, F., Lamarche, J., Viseur, S., Prosser, G., 2018. Fault growth mechanisms and scaling properties in foreland basin system: The case study of Monte Alpi, Southern Apennines, Italy. J. Struct. Geol. 116, 94–113. https://doi.org/10.1016/J.JSG.2018.08.009

La Bruna, V., Agosta, F., Prosser, G., 2017. New insights on the structural setting of the Monte Alpi area, Basilicata, Italy. Ital. J. Geosci. 136, 5–22.

La Bruna, V., Bezerra, F.H.R., Souza, V.H.P., Maia, R.P., Auler, A.S., Araujo, R.E.B., Cazarin, C.L., Rodrigues, M.A.F., Vieira, L.C., Sousa, M.O.L., 2021. High-permeability zones in folded and faulted silicified carbonate rocks – Implications for karstified carbonate reservoirs. Mar. Pet. Geol. 128, 105046. https://doi.org/10.1016/j.marpetgeo.2021.105046

La Bruna, V., Lamarche, J., Agosta, F., Rustichelli, A., Giuffrida, A., Salardon, R., Marié, L., 2020. Structural diagenesis of shallow platform carbonates: Role of early embrittlement on fracture setting and distribution, case study of Monte Alpi (Southern Apennines, Italy). J. Struct. Geol. 131. https://doi.org/10.1016/j.jsg.2019.103940

Lamarche, J., Lavenu, A.P.C., Gauthier, B.D.M., Guglielmi, Y., Jayet, O., 2012. Relationships between fracture patterns, geodynamics and mechanical stratigraphy in Carbonates (South-East Basin, France). Tectonophysics 581, 231–245. https://doi.org/10.1016/j.tecto.2012.06.042

Land, L.S., 1980. The isotopic and trace element geochemistry of dolomite: the state of the art, in: Concepts and Models of Dolomitization. SEPM Special Publication No 28. pp. 87–110.

Li, H., Bai, H., Wu, J., Zhao, H., Ma, K., 2017. A method for prevent water inrush from karst collapse column: a case study from Sima mine, China. Environ. Earth Sci. 76, 1–10. https://doi.org/10.1007/s12665-017-6831-2

Liu, H., Ma, T., Tan, X., Zeng, W., Hu, G., Xiao, D., Luo, B., Shan, S., Su, C., 2016. Origin of structurally controlled hydrothermal dolomite in epigenetic karst system during shallow burial: An example from Middle Permian Maokou Formation, central Sichuan Basin, SW China. Pet. Explor. Dev. 43, 1000–1012. https://doi.org/10.1016/S1876-3804(16)30117-3

Liu, H., Tan, X., Li, L., Ding, X., Cao, J., Yang, G., Ma, T., 2019. Eogenetic Karst in Interbedded Carbonates and Evaporites and Its Impact on Hydrocarbon Reservoir: A

New Case from Middle Triassic Keikoupo Formation in Sichuan Basin, Southwest China. J. Earth Sci. 30, 908–923. https://doi.org/10.1007/s12583-019-0888-7

Liu, Z.B., Gao, S.L., Huang, X.R., Yue, Y., Liu, S.L., Wu, S.Q., Zhang, Z.P., Yang, S.B., 2014. Formation and distribution of the Ordovician reservoir in Maigaiti Slope, Tarim basin. Acta Pet. Sin. 35, 654–663.

Liu, Z.B., Wu, S.Q., Liu, S.L., 2013. Reservoir types and main controlling factors of Ordovician in Yubei area, Tarim Basin. Acta Pet. Sin. 34, 638–646.

Lopes, J.A.G., Medeiros, W.E., La Bruna, V., de Lima, A., Bezerra, F.H.R., Schiozer, D.J., 2022. Advancements towards DFKN modelling: Incorporating fracture enlargement resulting from karstic dissolution in discrete fracture networks. J. Pet. Sci. Eng. 209, 109944. https://doi.org/10.1016/j.petrol.2021.109944

Loucks, R. G. Handford, C.R., 1992. Origin and recognition of fractures, breccias, and sediment fills in paleocave-reservoir networks. Permian Basin Sect. SEPM Publ. 92, 31–44.

Loucks, R.G., 1999. Paleocave Carbonate Reservoirs: Origins, Burial-Depth Modifications, Spatial Complexity, and Reservoir Implications. Am. Assoc. Pet. Geol. Bull. 83, 1795–1834. https://doi.org/10.1306/E4FD426F-1732-11D7-8645000102C1865D

Lucia, F.J., 2007. Carbonate reservoir characterization: An integrated approach, 2nd ed. Springer-Verlag Berlin Heidelberg. https://doi.org/10.1007/978-3-540-72742-2

Mádl-Szőnyi, J., Erőss, A., Tóth, Á., 2017. Fluid Flow Systems and Hypogene Karst of the Transdanubian Range, Hungary—With Special Emphasis on Buda Thermal Karst, in: Hypogene Karst Regions and Caves of the World. pp. 267–278. https://doi.org/10.1007/978-3-319-53348-3_17

Matos, R.M.D., 2000. Tectonic evolution of the equatorial South Atlantic, in: Mohriak, W., Taiwani, M. (Eds.), Geophysical Monograph Series. American Geophysical Union (AGU), pp. 331–354. https://doi.org/10.1029/GM115p0331

Matos, R.M.D., 1992. The Northeast Brazilian Rift System. Tectonics 11, 766–791. https://doi.org/10.1029/91TC03092

Matsuda, N.S., Viviers, M.C., 1989. Caracterizaçao do marco radioativo da parte superior da Formacao Jandaıra na Bacia Potiguar, in: In Anais Do XI Congresso Brasileiro de Paleontologia. p. Vol. 2, pp. 1029–1041.

Matthews, R.K., 1974. A process approach to diagenesis of reefs and reef associated limestones. Soc. Econ. Paleontol. Mineral. 18, 234–256.

McBride, E.F., 1977. Secondary porosity-importance. Gulf Coast Assoc. Geol. Soc. Trans. 27, 121–122.

Melo, A.C.C., de Castro, D.L., Bezerra, F.H.R., Bertotti, G., 2016. Rift fault geometry and evolution in the Cretaceous Potiguar Basin (NE Brazil) based on fault growth models. J. South Am. Earth Sci. 71, 96–107. https://doi.org/10.1016/j.jsames.2016.07.006

Menezes, D.F., Bezerra, F.H., Balsamo, F., Arcari, A., Maia, R.P., Cazarin, C.L., 2020. Subsidence rings and fracture pattern around dolines in carbonate platforms – Implications for evolution and petrophysical properties of collapse structures. Mar. Pet. Geol. 113, 104113. https://doi.org/10.1016/j.marpetgeo.2019.104113

Monroe, W.H., 1970. A glossary of Karst terminology. https://doi.org/10.3133/wsp1899K

Moore, C., 2001. Carbonate reservoirs: Porosity, Evolution and Diagenesis in a Sequence Stratigraphic Framework.

Moore, C.H., 1989. Carbonate diagenesis and porosity. Elsevier.

Moore, C.H., Wade, W.J., 2013. Carbonate reservoirs: Porosity and diagenesis in a sequence stratigraphic framework. Newnes.

Morais Neto, J.M., Hegarty, K., Alkmin, F., Matos, R., Karner, G., 2000. Uplift and erosion in the Borborema Province, Northeast Brazil: Insights from Apatite Fission Track Analysis, in: 31st International Geological Congress. Rio de Janeiro.

Morais Neto, J.M., Hegarty, K.A., Karner, G.D., Alkmim, F.F., 2009. Timing and mechanisms for the generation and modification of the anomalous topography of the Borborema Province, northeastern Brazil. Mar. Pet. Geol. 26, 1070–1086. https://doi.org/10.1016/j.marpetgeo.2008.07.002

Morse, J.W., Mackenzie, F.T., 1990. Geochemistry of sedimentary carbonates. Elsevier Scientific Publication Co., New York, USA.

Nader, F.H., Swennen, R., Keppens, E., 2008. Calcitization/dedolomitization of Jurassic dolostones (Lebanon): results from petrographic and sequential geochemical analyses. Sedimentology 55, 1467–1485. https://doi.org/10.1111/j.1365-3091.2008.00953.x

Palmer, A.N., 1991. Origin and morphology of limestone caves. Geol. Soc. Am. Bull. 103, 1–21.

Palmer, T.J., Hudson, J.D., Wilson, M.A., 1988. Palaeoecological evidence for early aragonite dissolution in ancient calcite seas. Nature 335, 809–810.

Panza, E., Agosta, F., Rustichelli, A., Vinciguerra, S.C., Ougier-Simonin, A., Dobbs, M., Prosser, G., 2019. Meso-to-microscale fracture porosity in tight limestones, results of an integrated field and laboratory study. Mar. Pet. Geol. 103, 581–595. https://doi.org/10.1016/j.marpetgeo.2019.01.043

Pessoa Neto, O.C., Soares, U.M., Silva, J.G.F., Roessner, E.H., Florêncio, C.P., Souza, C.A.V., 2007. Bacia Potiguar. Bol. Geociências da Petrobras 15, 357–369.

Pisani, L., Antonellini, M., Bezerra, F.H.R., Carbone, C., Auler, A.S., Audra, P., La Bruna, V., Bertotti, G., Balsamo, F., Pontes, C.C.C., De Waele, J., 2022. Silicification, flow pathways, and deep-seated hypogene dissolution controlled by structural and stratigraphic variability in a carbonate-siliciclastic sequence (Brazil). Mar. Pet. Geol. 139, 105611. https://doi.org/10.1016/j.marpetgeo.2022.105611

Pontes, C.C.C., Bezerra, F.H.R., Bertotti, G., La Bruna, V., Audra, P., De Waele, J., Auler, A.S., Balsamo, F., De Hoop, S., Pisani, L., 2021. Flow pathways in multiple-direction fold hinges: Implications for fractured and karstified carbonate reservoirs. J. Struct. Geol. 146, 104324. https://doi.org/10.1016/j.jsg.2021.104324

Porpino, K.O., Junior, V.S., Santos, M.F.C.F., 2009. Lajedo de Soledade, Apodi, RN. Ocorrência peculiar de megafauna fóssil quaternária no Nordeste do Brasil., in: Sítios Geológicos e Paleontológicos Do Brasil. CPRM, pp. 403–412.

Rabelo, J.G., Maia, R.P., Bezerra, F.H.R., Silva, C.C.N., 2020. Karstification and fluid flow in carbonate units controlled by propagation and linkage of mesoscale fractures, Jandaíra Formation, Brazil. Geomorphology 357, 107090. https://doi.org/10.1016/j.geomorph.2020.107090

Rabelo, J.G., Silva, A.T., Bezerra, F.H.R., Moraes, A., 2015. Modelagem numérica da deformação em carbonatos e implicações na formação de carste. Geol. USP. Série Científica 15, 99. https://doi.org/10.11606/issn.2316-9095.v15i2p99-110

Rajaram, H., Cheung, W., Chaudhuri, A., 2009. Natural analogs for improved understanding of coupled processes in engineered earth systems: examples from karst system evolution. Curr. Sci. 97, 1162–1176.

Raynaud, S., Carrio-Schaffhauser, E., 1992. Rock matrix structures in a zone influenced by a stylolite. J. Struct. Geol. 14, 973–980. https://doi.org/10.1016/0191-8141(92)90028-U

Reis, J.A. dos, de Castro, D.L., de Jesus, T.E.S., Filho, F.P.L., 2014. Characterization of collapsed paleocave systems using GPR attributes. J. Appl. Geophys. 103, 43–56. https://doi.org/10.1016/j.jappgeo.2014.01.007

Renard, F., Bernard, D., Desrues, J., Ougier-Simonin, A., 2009. 3D imaging of fracture propagation using synchrotron X-ray microtomography. Earth Planet. Sci. Lett. 286, 285–291. https://doi.org/10.1016/j.epsl.2009.06.040

Ronchi, P., Jadoul, F., Savino, R., 2004. Quaternary dedolomitization along fracture systems in a late triassic Dolomitized platform (Western Southern Alps, Italy). Carbonates and Evaporites 19, 51–66. https://doi.org/10.1007/BF03175195

Rustichelli, A., Agosta, F., Tondi, E., Spina, V., 2013. Spacing and distribution of bed-perpendicular joints throughout layered, shallow-marine carbonates (Granada Basin, southern Spain). Tectonophysics 582, 188–204. https://doi.org/10.1016/J.TECTO.2012.10.007

Rustichelli, A., Iannace, A., Tondi, E., Di Celma, C., Cilona, A., Giorgioni, M., Parente, M., Girundo, M., Invernizzi, C., 2017. Fault-controlled dolomite bodies as palaeotectonic indicators and geofluid reservoirs: New insights from Gargano Promontory outcrops. Sedimentology 64, 1871–1900. https://doi.org/10.1111/sed.12378

Sampaio, A. V., Schaller, H., 1968. Introdução à estratigrafia cretácea da Bacia Potiguar. Bol. Técnico da Petrobrás 11, 19–44.

Santos Filho, M.A.B., Piovesan, E.K., Fauth, G., Srivastava, N.K., 2015. Paleoenvironmental interpretation through the analysis of ostracodes and carbonate microfacies: study of the Jandaíra Formation, Upper Cretaceous, Potiguar Basin. Brazilian J. Geol. 45, 23–34. https://doi.org/10.1590/23174889201500010002

Schmidt, V., Mcdonald, D.A., 1979. The role of secondary porosity in the course of sandstone diagenesis. SEPM Spec. Publ. 26, 175–207.

Schmidt, V., McDonald, D.A., 1979. The role of secondary porosity in the course of sandstone diagenesis. Soc. Econ. Paleontol. Mineral. 26, 175–207.

Schoenherr, J., Reuning, L., Hallenberger, M., Lüders, V., Lemmens, L., Biehl, B.C., Lewin, A., Leupold, M., Wimmers, K., Strohmenger, C.J., 2018. Dedolomitization: review and case study of uncommon mesogenetic formation conditions. Earth-Science Rev. 185, 780–805. https://doi.org/10.1016/j.earscirev.2018.07.005

Scholle, P.A., Ulmer-Scholle, D.S., 2003. A color guide to the petrography of carbonate rocks : grains, textures, porosity, diagenesis. AAPG.

Silva, O.L., Bezerra, F.H.R., Maia, R.P., Cazarin, C.L., 2017. Karst landforms revealed at various scales using LiDAR and UAV in semi-arid Brazil: Consideration on karstification processes and methodological constraints. Geomorphology 295, 611–630. https://doi.org/10.1016/J.GEOMORPH.2017.07.025

Stafford, K.W., Nance, R., Rosales-Lagarde, L., Boston, P.J., 2008. Epigene and hypogene karst manifestations of the Castile Formation: Eddy County, New Mexico and Culberson County, Texas, USA. Int. J. Speleol. 37, 83–98.

Stoessell, R.K., Moore, C.H., 1983. Chemical Constraints and Origins of Four Groups of Gulf Coast Reservoir Fluids. Am. Assoc. Pet. Geol. Bull. 67, 896–906. https://doi.org/10.1306/03B5B6C8-16D1-11D7-8645000102C1865D

Sujkowski, Z.L., 1958. Diagenesis. Am. Assoc. Pet. Geol. Bull. 42, 2692–2717. https://doi.org/10.1306/0BDA5C09-16BD-11D7-8645000102C1865D

Sun, C., Yu Hong-feng, Wang Huai-sheng, Liu Hu, Zhang Zheng-hong, Han Jie, Luo Xin-sheng, 2012. Vugular Formation of Carbonates in Ordovician Yingshan Reservoir in Tazhong Northern Slope of Tarim Basinn. Nat. Gas Geosci. 23, 230–236.

Tang, Z., Zhai, C., Zou, Q., Qin, L., 2016. Changes to coal pores and fracture development by ultrasonic wave excitation using nuclear magnetic resonance. Fuel 186, 571–578. https://doi.org/10.1016/j.fuel.2016.08.103

Taylor, J.M., 1950. Pore-Space Reduction in Sandstones. Am. Assoc. Pet. Geol. Bull. 34, 701–716. https://doi.org/10.1306/3D933F47-16B1-11D7-8645000102C1865D

Tian, F., Di, Q., Jin, Q., Cheng, F., Zhang, W., Lin, L., Wang, Y., Yang, D., Niu, C., Li, Y., 2019. Multiscale geological-geophysical characterization of the epigenic origin and deeply buried paleokarst system in Tahe Oilfield, Tarim Basin. Mar. Pet. Geol. 102, 16–32. https://doi.org/10.1016/j.marpetgeo.2018.12.029

Tibana, P., Terra, G.J.S., 1981. Seqüências carbonáticas do cretáceo na Bacia Potiguar. Bol. Técnico da Petrobrás 24, 174–183.

Tucker, M.E., 2001. Sedimentary petrology : an introduction to the origin of sedimentary rocks, 3rd ed. Blackwell Science.

Tucker, M.E., Wright, V.P., 1990. Diagenetic Processes, Products and Environments, in: Carbonate Sedimentology. Blackwell Publishing Ltd., Oxford, UK, pp. 314–364. https://doi.org/10.1002/9781444314175.ch7

Upchurch, S., Scott, T.M., Alfieri, M.C., Fratesi, B., Dobecki, T.L., 2019. Epigene and Hypogene Karst, in: The Karst Systems of Florida. Springer, Cham., pp. 359–441. https://doi.org/10.1007/978-3-319-69635-5_8

Vacher, H.L., Mylroie, J.E., 2002. Eogenetic karst from the perspective of an equivalent porous medium. Carbonates and Evaporites 17, 182–196. https://doi.org/10.1007/BF03176484

Vahrenkamp, V.C., Swar, P.K., 1994. Late Cenozoic dolomites of the Bahamas: metastable analogues for the genesis of ancient platform dolomites, in: Special Publications of Internacional Association of Sedimentologists. pp. 133–153.

Wang, B., Al-Aasm, I.S., 2002. Karst-controlled diagenesis and reservoir development: Example from the Ordovician main-reservoir carbonate rocks on the eastern margin of the Ordos basin, China. Am. Assoc. Pet. Geol. Bull. 86, 1639–1658.

Weidlich, O., 2010. Meteoric diagenesis in carbonates below karst unconformities: Heterogeneity and control factors. Geol. Soc. Spec. Publ. 329, 291–315. https://doi.org/10.1144/SP329.12

White, W.B., 1977. Role of solution kinetics in the development of karst aquifers. Int. Assoc. Hydrogeol. 12, 503–517.

Wilson, M.D., Stanton, P.T., 1994. Diagenetic mechanisms of porosity and permeability reduction and enhancement. Soc. Sediment. Geol. 3–44.

Worden, R.H., Burley, S.D., 2003. Sandstone diagenesis: the evolution of sand to stone. Sandstone Diagenes. Recent Anc. 4, 3–44.

Xavier Neto, P., Medeiros, W.E., 2006. A practical approach to correct attenuation effects in GPR data. J. Appl. Geophys. 59, 140–151. https://doi.org/10.1016/j.jappgeo.2005.09.002

Yang, Y., Zheng, K., Li, Zhiwei, Li, Zenghua, Si, L., Hou, S., Duan, Y., 2019. Experimental study on pore-fracture evolution law in the thermal damage process of coal. Int. J. Rock Mech. Min. Sci. 116, 13–24. https://doi.org/10.1016/j.ijrmms.2019.03.004

Youssef, A.A.A., Awotunde, A.A., 2019. Modelling fluid flow in karst reservoirs using Darcy Model with estimated permeability distribution. Comput. Geosci. 133, 104311. https://doi.org/10.1016/j.cageo.2019.104311

Zang, H., Zheng, X., Jia, Z., Chen, J., Qin, Z., 2015. The impact of hydrogeochemical processes on karst groundwater quality in arid and semiarid area: a case study in the Liulin spring area, north China. Arab. J. Geosci. 8, 6507–6519. https://doi.org/10.1007/s12517-014-1679-1

Zhang, J., Zhou, J., Fu, L., Li, H., Lou, D., 2020. Karstification of Ordovician carbonate reservoirs in Huanghua depression and its control factors. Carbonates and Evaporites 35, 42. https://doi.org/10.1007/s13146-020-00572-x

Zhiqian, G., Zhongbao, L., Shanlin, G., Qunan, D., Shiqiang, W., Shilin, L., 2016. Characteristics and genetic models of Lower Ordovician carbonate reservoirs in southwest Tarim Basin, NW China. J. Pet. Sci. Eng. 144, 99–112. https://doi.org/10.1016/j.petrol.2016.03.007

Zoback, M.D., 2007. Reservoir Geomechanics. Cambridge University Press.

5. ARTIGO 2

Pore network characteristics as a function of diagenesis: implications for epigenic karstification in shallow-water carbonates

Renata E. B. Araújo[a*], Vincenzo La Bruna[a,b], Andrea Rustichelli[c], Francisco H. R. Bezerra[a,b], Milton Xavier[d], Fabrizio Agosta[e]

[a] PostGraduation Program on Geodynamics and Geophysics, Federal University of Rio Grande do Norte, Brazil
[b] Department of Geology, Federal University of Rio Grande do Norte, Brazil
[c] Geology Division, School of Sciences and Technology, University of Camerino, Italy
[d] Department of Geophysics, Federal University of Rio Grande do Norte, Brazil
[e] Department of Sciences, University of Basilicata, Italy

*Corresponding author:
Email address: renataaa.brito@gmail.com (R.E.B. Araújo)

Journal of Petroleum and Marine Geology
Submissão: 30 de julho de 2022

Abstract

Karst processes may be critical for developing secondary porosity and permeability within carbonate reservoirs and aquifers. Karstification can significantly influence reservoir storage capacity and subsurface fluid flow. This study investigates the interplay between fluid-flow pathways and diagenesis in an epigenic karst setting in Cretaceous shallow-water carbonate rocks, Potiguar Basin, Brazil. The results indicate that dissolution occurred at all diagenetic stages within an epigenic karst system, but the last stage is the most important because it has the most recent subaerial exposure. Dissolution produced during the last karst stage occurred in the vadose and phreatic environments, leading to precipitation of isopachous, blocky and syntaxial cements. Dissolution affected the pristine matrix pore network and localized on preexisting discontinuities such as stylolites, fractures, and bedding surfaces. The resulting karst cavities are classified as vugs, channels and caverns, varying from a few millimeters to hundreds of meters in size. In epigenic karst systems, high microporosity percentages are commonly due to moldic, intragrain/intrafossil and intercrystal porosities. The results of our study show how such porosities can be connected to fractures, veins and stylolites at the microscale. Karst dissolution can further increase porosity and the overall rock permeability.

Keywords: dissolution; diagenesis; vuggy porosity; Potiguar Basin

5.1 Introduction

Epigenic karst occurs in carbonates exposed to subaerial conditions and often enhances the flow and storage of geofluids (*e.g.*, hydrocarbons, groundwater, geothermal fluids, etc.) of subsurface reservoirs (Fu, 2006; Hajikazemi et al., 2010; Jiu et al., 2021; Liu et al., 2016; Loucks, 1999; Wang and Al-Aasm, 2002; Zhang et al., 2020). During epigenic karstification, meteoric waters dissolve part of the carbonate successions, generating a vuggy pore space depending upon lithofacies, the geometry of the microfracture network, and water chemistry (Araújo et al., 2021; Rustichelli et al., 2017; Sun et al., 2012). In the epigenic karst-related pore networks, vuggy pore space might have developed during the three following main diagenetic stages (Hajikazemi et al., 2010; Wang and Al-Aasm, 2002): (1) eodiagenesis, contributing to the early generation of vuggy pore spaces in near-surface carbonate rocks due to periodic influxes of meteoric water during sea-level lowstands; (2) mesodiagenesis, contributing to partial rock dissolution and fracture widening in buried carbonate rocks due to deeper circulation of meteoric water in concert with acidic formation waters; and (3) telodiagenesis, when late longstanding subaerial exposure (meteoric environment) after rock exhumation can form new dissolution features and enlarge those already existing (Bagni et al., 2022; Cazarin et al., 2019; Pisani et al., 2022).

In this regard, identifying karst-related pore networks in carbonate rocks is challenging due to their irregular patterns and geometries (Hopkins, 1999; James and Choquette, 1988).

Several models were thought to explain epigenic karst in carbonate reservoirs and its impact on reservoir quality (e.g., Ganai et al., 2018; Jiu et al., 2021; Liu et al., 2019; Tian et al., 2019; Wang and Al-Aasm, 2002). Among those, Tian et al. (2019) proposed a genetic classification model that could improve the understanding of complex paleokarst systems, guiding several hydrocarbon exploration phases. Liu et al. (2019) documented the influence of residual weathered and solution-collapse breccia, solution pores, silicification and dedolomitization on reservoir quality. Jiu et al. (2021) reported different dissolution pores and cement types associated with karst reservoirs, setting up a time-space karst evolutionary model. In addition to this information, several studies on karstified carbonates showed how microfractures and stylolites acted as primary conduits for fluid percolation and that matrix porosity, even those made up of micropores, might also play an essential role in fluid flow when connected by microfractures (e.g., He et al., 2014; Liu et al., 2019; Panza et al., 2019).

However, even if karst-related dissolution features such as vugs, channels, and caves are considered of primary importance in controlling reservoir quality (e.g., Choquette and

Pray, 1970), only a few studies have thus far addressed the factors controlling their spatial distribution (e.g., Hajikazemi et al., 2010; Wang and Al-Aasm, 2002). Since karst features can form during all diagenetic stages, a more comprehensive understanding of the microscale dissolution processes occurring during the whole diagenetic history of carbonates is needed to shed new light on the origin of epigenic karst cavities.

In this regard, the present study aims to explain how the individual carbonate rock components (grains, matrix, cement, and pores), sedimentary structures (planar and cross-lamination), and microstructural elements (fractures, veins, and stylolites) influence epigenic karst. In particular, the present work focuses on the aforementioned dissolution features in Cretaceous shallow-water carbonates of the Jandaíra Formation (Potiguar Basin, Brazil), which represent a surface analog of mixed karstified and fractured carbonate reservoirs (Araújo et al., 2021; Bagni et al., 2020; Balsamo et al., 2020; Bertotti et al., 2017; de Graaf et al., 2017; Giuffrida et al., 2019; Menezes et al., 2020; Rabelo et al., 2020).

5.2 Geological setting

The Potiguar Basin (Fig. 5.1A) is located in the eastern part of the Brazilian equatorial margin and was formed due to the breakup of South American and African tectonic plates during the Mesozoic Pangea rifting (e.g., Matos, 2000; de Castro et al., 2012; Melo et al., 2016). Sedimentary rocks have accumulated within the Potiguar Basin since the Early Cretaceous (Pessoa Neto et al., 2007), forming three main supersequences: (1) rift supersequence, deposited during the Early Cretaceous; (2) mid-Cretaceous (Aptian – Albian) postrift supersequence; and (3) drift supersequence, Albian age to the present.

The Jandaíra Formation belongs to the Drift Supersequence. It comprises shallow marine limestone facies formed in the Late Cretaceous (Sampaio and Schaller, 1968) at water depths less than 50 m, according to biotic assemblages (ostracods, green/red algae, planktonic to benthonic foraminifers, and Echinoidea) (Matsuda and Viviers, 1989; Tibana and Terra, 1981). The dominant carbonate facies are bioclastic packstones to wackestones deposited under low-energy water settings and bioclastic grainstones to packstones, indicating intermediate-energy water settings (Santos Filho et al., 2015). Additional facies include oolitic carbonate grainstones, mudstones with planktonic and benthonic foraminifera and carbonate mudstones with birds-eyes. The bed interfaces consist of trough-cross beds, planar-cross beds and low-angle cross-strata; bioturbation is diffuse (Porpino et al., 2009). Dolomitization occurs mainly in low water energy facies (Tibana and Terra, 1981).

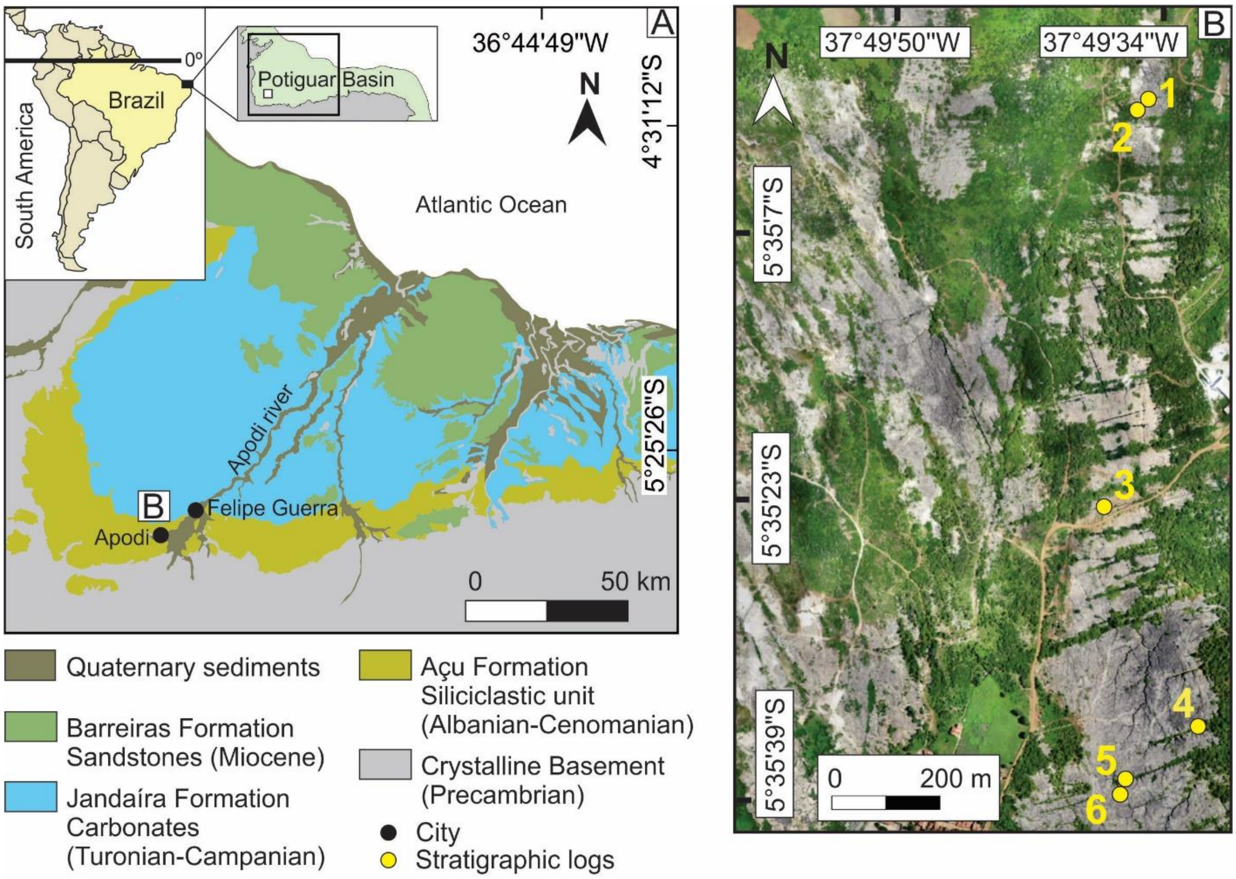

Fig. 5.1 - (A) Simplified geological map of the Potiguar Basin and Soledade outcrop location; (B) drone image from approximately 100 m above the Soledade outcrop, allowing a pixel resolution of 4 cm on the ground, and location of the six detailed stratigraphic logs.

Karstification of the Jandaíra Formation carbonates was due to meteoric water dissolution (Bertotti et al., 2017; de Graaf et al., 2017). The semiarid climate preserved the resulting epigenetic karst system (Xavier Neto and Medeiros, 2006). It hence allowed the study of meso-scale and macroscale karst landforms (Silva et al., 2017), geometry (Reis et al., 2014) and the control exerted by structural elements on dissolution (Araújo et al., 2021; Lopes et al., 2022; Menezes et al., 2020; Rabelo et al., 2020).

5.3 Methodology

5.3.1 Field analysis

We performed field investigations along vertical walls striking NNW–SSE and ENE–WSW of the Soledade outcrop (Fig. 5.1). Preliminary qualitative characterization of bedding, carbonate lithologies, laminations, and karst dissolution-related features was performed. Six representative vertical sections of the outcrops were selected to perform stratigraphic logging and rock sampling using a portable drill. A total of 160 plugs (2.54 cm diameter) were collected and cut to a height of 4 cm for petrographic and petrophysical analyses.

5.3.2 Laboratory analyses

We performed petrographic analysis on 137 thin sections obtained from the rock plugs to document and analyze the diagenetic processes, porosity types and percentages from the micrometer scale (petrographically) to the meter scale (using the outcrops). An Olympus BX41 polarized light microscope with a digital camera was used for the petrographic study. We followed Dunham (1962) and Embry and Klovan (1971) to petrographically classify the rocks based on their textures. The porosity description followed Lucia (2007) because the definition of vug deviates from the restrictive definition of vugs used by Choquette and Pray (1970). Alizarin red-S solution was used to identify the main carbonate minerals (calcite versus dolomite), and colored epoxy impregnation was used to recognize the pore space.

Cathodoluminescence (CL) was performed in 10 thin sections using a CITL MK 5-2 electron source operated at 12 kV and 215 µA in a vacuum (<0.050 mBar) coupled to a Zeiss Scope A1 microscope. Images were collected by a Zeiss Axiocam 705 color camera and processed by Zeiss software ZEN 3.3 lite (blue edition).

Adobe Photoshop CC 2018 software was used in 40 thin sections to determine the percentage of different dissolution pore types of the pore network. We measured the porosity rate in photomicrographs from the blue pixel numbers in the image. This analysis was performed using the color range tool, and gray filter shades were used to discriminate the original blue pixels. Then, ImageJ software was used to calculate the percentage of porosity in the images.

The five most representative samples were analyzed with scanning electron microscopy (SEM) and energy dispersive X-ray spectrometry (EDS) to study dissolution and mineralization features and their diagenetic meaning in detail. SEM analyses were conducted by employing a Shimadzu microscope model SSX-550.

The ten most representative plugs were characterized with Nikon XT H 225 ST computed tomography (CT) equipment. We opted to collect the most homogeneous plugs along a pristine portion of the studied outcrops that showed no visible pores as

vugs or channels for porosity characterization. The procedure followed the already tested workflow presented in Araujo et al. (2020). Afterward, 3D images of the pore space were composed, and scanlines of 27 mm^3 subvolumes were selected. To obtain petrophysics parameters, the following workflow was applied (Fig. 5.2): (1) apparent pore structure analysis based upon the 2D tomography images; (2) selection of representative subvolumes in the regions of interest, and then both horizontal and vertical scanline analysis by means of ImageJ software; (3) build-up of the digital models by using 3DSlicer software;

(4) subdivision of the pore space into single segments; and (5) calculation of the amounts of both total and connected porosity and both size and sphericity parameters of single pores after image segmentation. These data were used to plot pore number versus pore size and sphericity estimation along digital scanlines.

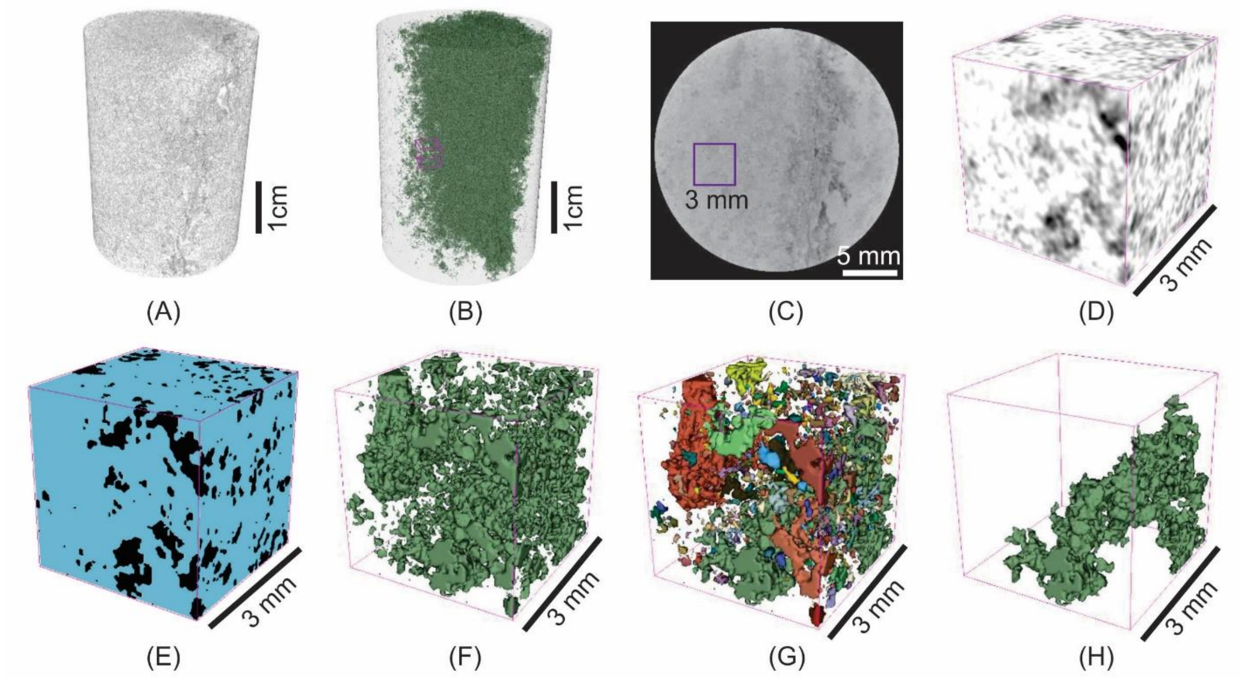

Fig. 5.2 - Analytic procedure of pore structure based on CT scanning: (A) digital model of a plug; (B) and (C) volume selection; (D) pretreatment result; (E) segmentation result; (F) total porosity; (G) splitting islands to segments; (H) isolating the largest connected porosity.

5.4 Results

In the carbonates, karstification ranged from slightly to intensely karstified beds throughout the stratigraphic succession (Fig. 5.3A). Dissolution is localized along bedding surfaces and bed-parallel stylolites (Fig. 5.3A, B, and C), within beds along cross-stratified laminae (Fig. 5.3D) (Araújo et al., 2021), and bed-perpendicular fractures, which are partially or completely filled with calcite cement (Fig. 5.3B and C).

The six stratigraphic logs (Fig. 5.1B and Fig. 5.4) show carbonate units with near white to light gray limestones, which are arranged in beds 14 cm to 95 cm thick. The units are made up of three main facies: carbonate packstones, carbonate grainstones, and crystalline carbonates. The carbonates include karst dissolution cavities such as vugs, channels, and circular-to-elongated caves (Fig. 5.3).

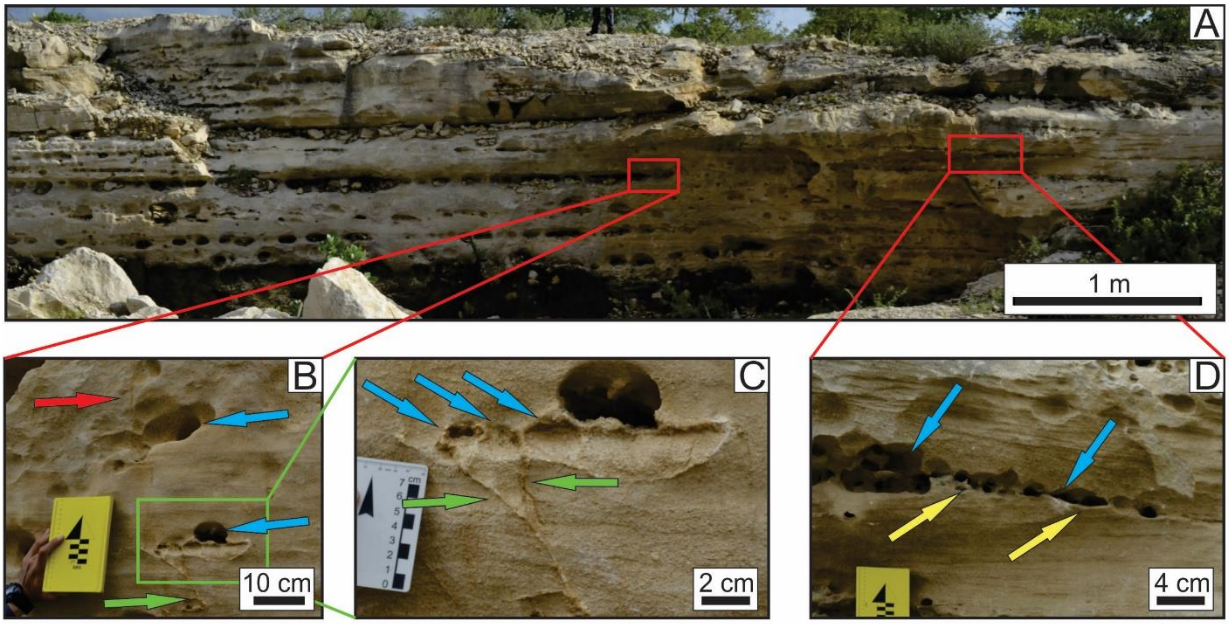

Fig. 5.3 - (A) Karst dissolution features at the mesoscale view; (B) vuggy pore spaces (blue arrows) along layers connected by subvertical fractures (red arrows) and veins (green arrow); (C) close-up view of vuggy pore space (green rectangle) displaying how vugs (blue arrows) can be enlarged and connected by veins (green arrows); and (D) isolated vuggy pore space (blue arrows) along planar cross-bedding connected to form channels.

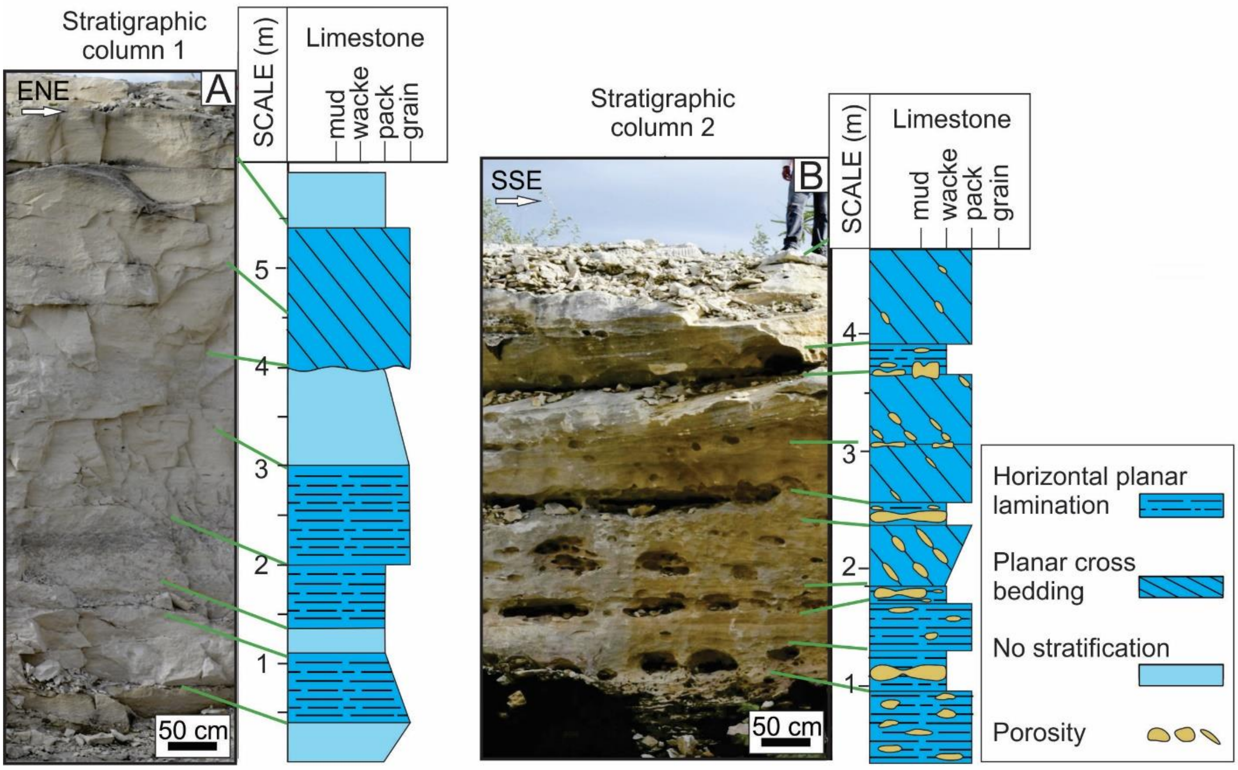

Fig. 5.4 - Examples of stratigraphic columns from the Soledade outcrop showing (A) incipient karst dissolution and (B) more advanced karst dissolution along stratigraphic surfaces.

5.4.1 Petrographic analysis

The results are based on the petrography of 119 thin sections under planar polarized light coupled with cathodoluminescence.

a) Microfacies

The microfacies mainly consist of peloidal and skeletal carbonate packstones and skeletal carbonate grainstones. Carbonate packstones are dominated by benthic foraminifera (e.g., miliolids; Fig. 5.5A), minor echinoderm plates, bivalves, calcareous algae, and ostracods. Within the carbonate packstones, some portions of the micritic matrix are replaced by fabric-selective dolomite (Fig. 5.5B).

Skeletal carbonate grainstones (Fig. 5.5C, Fig. 5.5G and Fig. 5.6A-F) contain bivalves, bryozoans, gastropods, ostracods, benthic foraminifera, echinoderms, worm tubes, and calcareous algae. Allochems such as intraclasts, pellets, oolites and oncoids are also identified. Evidence of fossil-free crystalline carbonates composed of calcite and dolomite (Fig. 5.5D).

b) Diagenetic features

The main diagenetic events recorded by the analyzed carbonates include cementation, neomorphism, recrystallization, dolomitization, compaction (both mechanical and chemical), dedolomitization, and dissolution. The descriptions are according to Flügel (2010), Scholle and Ulmer-Scholle (2003), Tucker (2001), and Tucker and Wright (1990).

i. Cementation

The main types of calcite cement are fibrous cement (Fig. 5.5E), fine-crystalline isopachous rim cement (Fig. 5.5F), and (5) fine- to medium-grained equant calcite cement, also named blocky calcite spar and microspar (Fig. 5.5G). Calcite crystal sizes vary predominantly from fine microcrystalline (4 to 8 µm) to thick mesocrystalline (> 500 µm). Equant calcite crystals, in some cases, fill the original pores due to preexisting dissolution.

Packstone types of cement are mainly equant sparry and calcite microspar. Grainstone types of cement consist of fibrous calcite, isopachous calcite, and equant calcite (Fig. 5.5).

Limestone cement of dolomites was either complete and masked the original rock texture (fabric-destructive, Fig. 5.5D) or partial (fabric-retentive, Fig. 5.5H). This cement can contain two dolomite sizes: (1) fine crystalline (< 40 µm) dolomite (dolomite I) (Fig. 5.5H) and (2) euhedral-subhedral, fine- to medium-crystalline (50-200 µm) dolomites, which have iron-rich cloudy cores surrounded by clear rims (Fig. 5.5H).

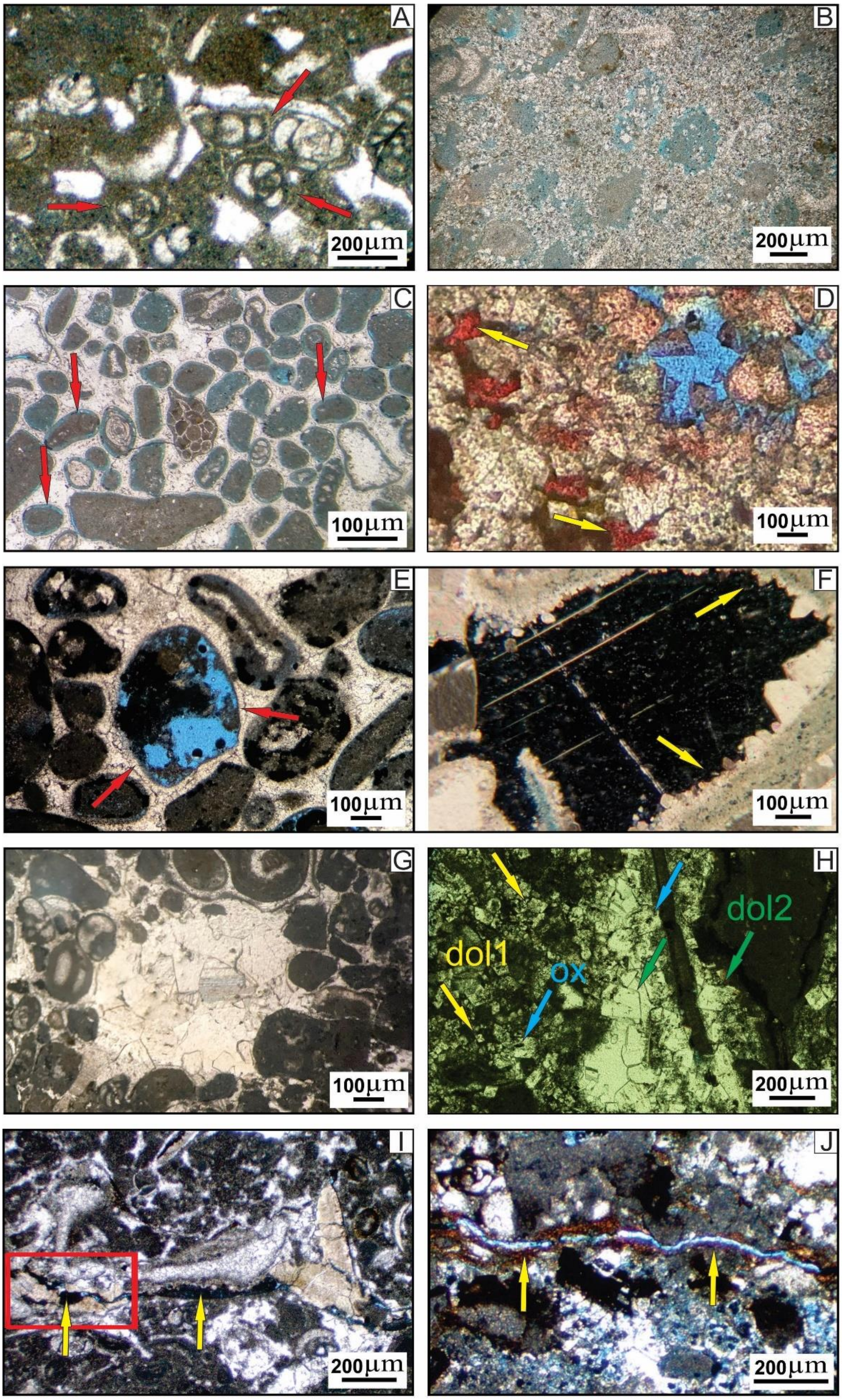

Fig. 5.5 - (A) Packstone dominated by benthic foraminifera showing micritic envelopes around bioclasts and allochems (red arrows); (B) recrystallization of micritic matrix in packstone, replaced by calcite and dolomite; (C) Neomorphism in grainstone as rounded cement-filled bodies (red arrows); (B) grainstone whose porosity system is dominated by moldic pores (red arrows); (D) dolostone exhibiting intercrystalline and moldic porosities. Rhombus-shaped calcite after dolomite records dedolomtization (yellow arrows); calcite is red due to Alizarin Red S staining; (E)

grainstone presenting fibrous calcite cementation around grains (red arrows). Vuggy porosity occurred only within grains; (F) rims of isopachous dog-tooth cement (yellow arrows); (G) complete pore filling by equant calcite; (H) ITwo phases of dolomitization evidenced by different dolomite sizes, evidenced by a green and yellow arrow; (I) crashed and rotated grains showing mechanical compaction fracture (in red rectangle zoom) filled with ferruginous material (yellow arrows); (J) channel porosity (yellow arrows) evidenced by the dissolution of ferruginous material along stylolite.

ii. Neomorphism and recrystallization

Neomorphism features such as calcite crystals mimic the shape of former bioclasts (Fig. 5.5C). These features are pervasive in the carbonate matrix and within some carbonate grains (Fig. 5.5A), resulting in a significant textural change. Recrystallization of the micritic carbonate matrix, replaced by coarser calcite and dolomite crystals, is observed in microfacies formed under low and high water-energy conditions (Fig. 5.5B).

iii. Mechanical compaction

Grains show evidence of translation, rotation, plastic deformation and breakage that changed the depositional grain packing (Fig. 5.5I). Fractures due to mechanical compaction, which run through grains and crystals of early diagenetic calcite, are filled with ferruginous material (Fig. 5.5I).

iv. Chemical compaction

Chemical compaction is evidenced by interpenetrative contacts of sutured and concavo-convex types between the grains, which can be dissolved to form stylolites. Some of them are associated with ferruginous material (Fig. 5.5J).

v. Dedolomitization

Dedolomitization processes are evidenced by rare rhombohedral calcite crystals sparse in dolostones due to dolomite turning into calcite. Dedolomitic calcite crystals show red coloration due to alizarin red S staining (Fig. 5.5D).

5.4.2 Pore types

We identified pore types following the classification by Lucia (2007). The porosity types commonly found in the study area rocks are the following: (I) interparticle pores, consisting of both intergrain (Fig. 5.6A) and intercrystal (Fig. 5.6B); (II) separate-vuggy pores, including moldic (Fig. 5.6C and D) and intraparticle pores. Intraparticle pores are further subdivided into intragrain (Fig. 5.6D), intracrystal (Fig. 5.6E), and intrafossil pores (Fig. 5.6F); (III) touching-vuggy pores, including cavernous pores (Fig. 5.7A), fractures (Fig. 5.7B), partially filled solution-enlarged fractures (Fig. 5.7C), randomly oriented microfractures (Fig. 5.7D), and fractures connecting moldic pores (Fig. 5.7E and F).

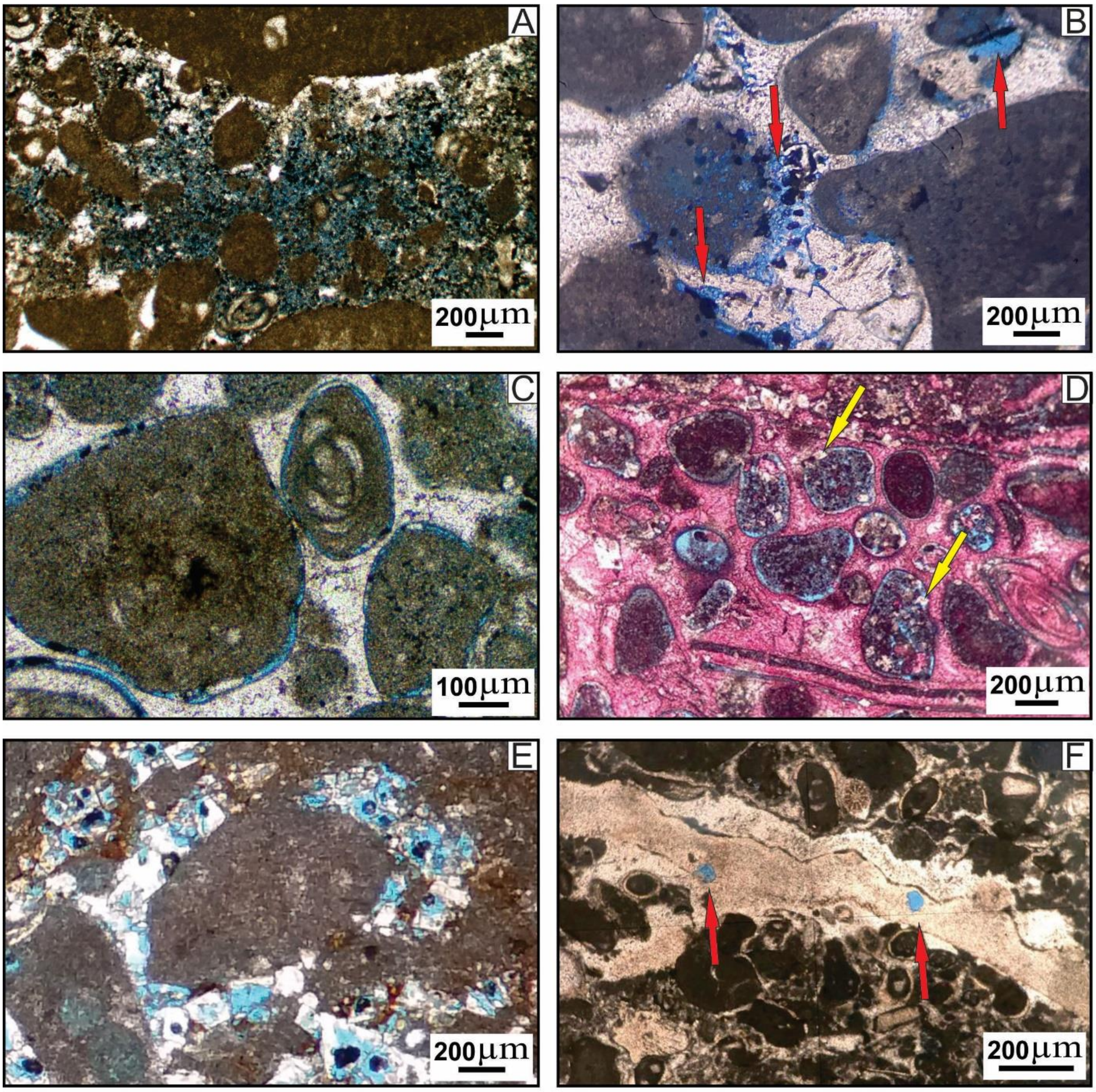

Fig. 5.6 - Interparticle pore space: (A) intergrains and (B) intercrystals (red arrows). Separate-vuggy pores: (C) moldic porosity due to the selective dissolution of cement rims around grains; (D) intragrain development of moldic porosity and early dolomite inside grains (yellow arrows); (E) intracrystal dissolution porosity inside dolomite crystals; and (F) intrafossil dissolution porosity (red arrows).

Molds from which dolomite was leaching are common (Fig. 5.7B). There is evidence of rock components controlling vuggy porosity development. In some parts, intergranular matrix porosity is pervasive (Fig. 5.6A), whereas intragrain matrix porosity predominates in other rock parts (Fig. 5.6D). The enlargement of separate vuggy pores contributed to the generation of touching vuggy pores.

Molds around fine grains (< 200 µm) exhibit dissolution in carbonate packstones and grainstones with planar and cross-stratifications (Fig. 5.7G and H). Intracrystal and intercrystal porosities are more diffuse in dolostones and dolomitized facies portions (Fig. 5.7I and J).

Porosity values in the studied carbonate facies range from 1.74% to 30% (Table 5.1). In detail, porosity varies from 1.74% to 17.67% in carbonate grainstones, from 3.07% to 17.06% in carbonate packstones, and up to ca. 30% in crystalline dolomitized facies.

Carbonate texture	Porosity (%)	
	Minimum	Maximum
Packstone	3.07	17.06
Grainstone	1.74	17.67
Carbonate crystalline	2.8	30.7

Table 5.1 - Porosity percentage in packstones, grainstones and carbonate crystalline (dolomitized facies) in the measured thin sections.

Carbonate grainstones and packstones show the predominance of intragrain porosity, moldic porosity and intercrystal porosity (Fig. 5.8). The porosity associated with stylolites is normally ca. 3% because these structures are rare in these facies, but in a few thin sections, such porosity can reach 70% of the total. In carbonate, crystals related to dolomitized crystalline facies (Fig. 5.8) show the predominance of intercrystal, moldic (porosity mimics the shape of dolomite crystals), intracrystal and cavernous porosities.

5.4.3 Scanning electron microscopy (SEM)

The most representative samples are further studied to investigate the processes of dissolution and dolomitization (Fig. 5.9). In packstones, dolomitization is restricted to micritic rock portions (Fig. 5.9A) and/or replaced preexisting cement crystals. The occurrence of dolomite crystals in grainstone facies is also common. Intracrystal pores are present in dolomites (Fig. 5.9B), but they are less abundant than intercrystal pores (Fig. 5.9C). Different images display variation in dissolution along stylolites crosscutting several portions of the rock. There is a continuous lining of elements along stylolites, such as silica (Si), carbon (C), aluminum (Al), magnesium (Mg), and potassium (K) (Fig. 5.9D), indicating a stylolite comprised of clay minerals or Si-phyllosilicates.

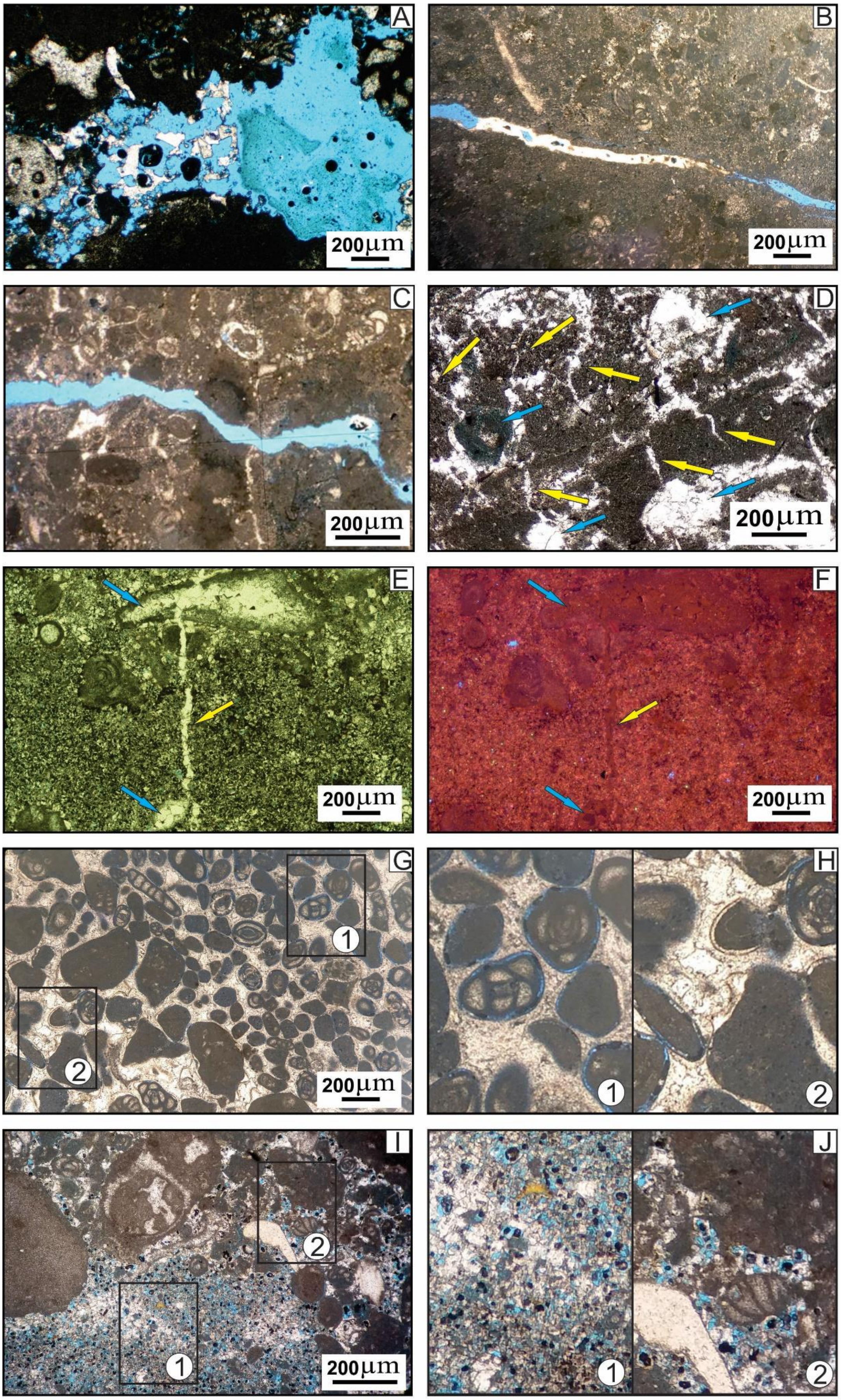

Fig. 5.7 - Touching-vug pores: (A) cavernous; (B) partially dissolved calcite vein; (C) solution-enlarged fracture; (D) microfractures (yellow arrows) connecting moldic pores (blue arrows), currently all filled by the same calcite cement; (E) fracture (yellow arrows) connecting moldic pores

(blue arrows), currently all filled by the same calcite cement; (F) fracture connecting moldic pores under CL; (G) and (H) zoom on alternate foresets boundary showing moldic (surrounding grains) more evident in fine-grained rock portions; (I) and (J) zoom on alternate foreset boundary presenting intracrystalline and intercrystalline porosity more concentrated on finely crystalline dolostone portion than in the coarser packstone portion.

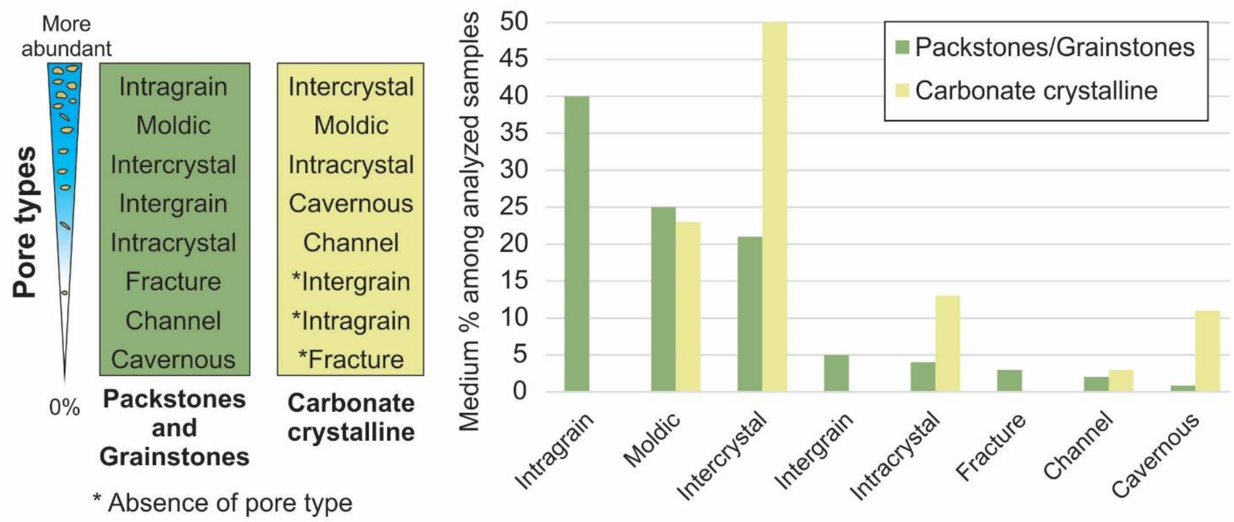

Fig. 5.8 - Percentage of porosity in packstones, grainstones and carbonate crystalline (dolomitized facies) estimated on thin-section imagery. These porosity values were calculated using visual inspection.

5.4.4 Three-dimensional porosity estimated by plug tomography

Three representative plugs (Fig. 5.10, Fig. 5.11 and Fig. 5.12) were analyzed to assess the three-dimensional porosity along the stylolite, intraparticle porosity, and interparticle porosity. To detail the pore space of each plug, scanlines of 27 mm^3 subvolumes were performed in both transversal and longitudinal directions of single plugs. Due to the resolution of the X-ray tomography images (voxel size of 35 µm), the smallest pore size observed is the corresponding individual voxel.

a) Porosity along stylolites

The resulting X-ray tomography images of the pore space of plug 1 (Fig. 5.10A and B) reveal a heterogeneous porosity in plugs containing stylolites. The individual pore sizes in plugs with stylolites range from approximately 10^4 $µm^3$ to 10^{11} $µm^3$. In these plugs, the pore size is smaller than ~10^7 $µm^3$ close to the stylolite (SV2, SV3 and SV5), and the number of pores can be four times that in surrounding regions (SV1, SV4, SV6, SV7, and SV8), as observed in Fig. 5.10C and D. Within stylolites (SV4, SV7 and SV8), pores smaller than approximately 10^7 $µm^3$ are usually connected, whereas they are isolated outside stylolites. Although the curves of the SV1, SV4 and SV6 subvolumes (Fig. 5.10C) are similar in terms of the number of pores, the center of the stylolite (SV4) contains pores up to two orders of magnitude larger than those farther away (SV1 and SV6). The pore distribution of the SV7 and SV8 subvolumes is similar to that of SV4. The number of pores along the stylolite (SV7, SV4, SV8, Fig. 5.10D) is much lower than that observed across the stylolite (SV1-SV6, Fig. 5.10C). This difference in the number of pores indicates that pore connectivity reduces the total amount of pores, increasing the permeability along stylolites.

X-ray tomography shows that the average sphericity of the pores decreases as they approach the center (SV4) of the stylolite. Therefore, the maximum pore size coincides with the minimum sphericity, as highlighted by the blue line in Fig. 5.13. This only occurs in samples with stylolites.

b) Intraparticle porosity

The resulting X-ray tomography images of plug 2 pore space (Fig. 5.11A and B) reveal that plugs containing intraparticle isolated pores are less heterogeneous than those with stylolites. The intraparticle pores are due to bioclast dissolution. The individual pore sizes in plugs with intraparticle porosities range from ~10^4 μm^3 to 10^9 μm^3. The concentration of intraparticle pores has no connection with large porosity structures (stylolites and fractures). The number of pores versus pore size varies randomly across the subvolumes (Fig. 5.11C and D). It is also difficult to establish a correlation between the pore size and its sphericity along the subvolume scanline (Fig. 5.13).

c) Interparticle porosity

The relationship between pore number and pore size using X-ray tomography images in plug 3 indicates that interparticle porosity varies less than interparticle porosity and porosity along stylolites (Fig. 5.12A and B). The interparticle porosity in the plug, representing more isolated than connected porosity, is mostly related to cement dissolution. Interparticle and intrapartcile porosities have no relationship with structural features such as stylolites and fractures. The size of an individual pore in a plug with intraparticle porosity ranges from approximately 10^4 μm^3 to 10^8 μm^3.

5.5 Discussion

According to the documented diagenetic history of the Jandaíra Formation (Bagni et al., 2022), the original data reported in this manuscript are now discussed to assess karstification during the main diagenetic stages that affected the study shallow-water carbonates (Fig. 5.14 and Fig. 5.15).

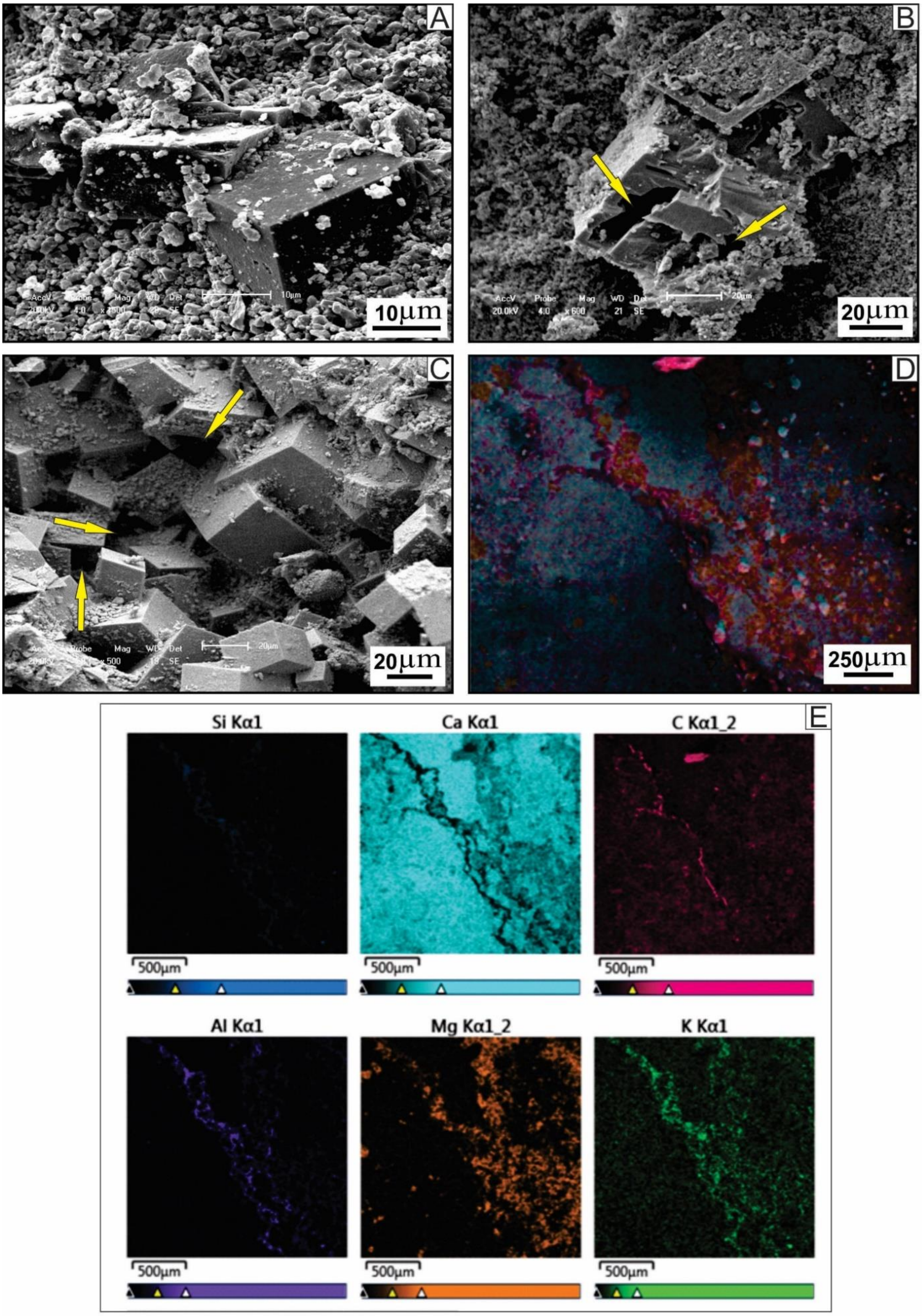

Fig. 5.9 - (A) SEM images of fine dolomite crystals developed in mud matrix; (B) intracrystal porosity inside rhombohedral dolomite crystals; (C) intercrystal porosity between rhombohedral dolomite crystals. (D) Element distribution imaging of stylolite in carbonate rocks, where (E)

brighter hues in the panels indicate an increased concentration of Al, Si, and Ca components. The low Ca level in the dissolution seams is due to calcite dissolution, which is linked to the passive concentration of insoluble species (Al and Si in phyllosilicates).

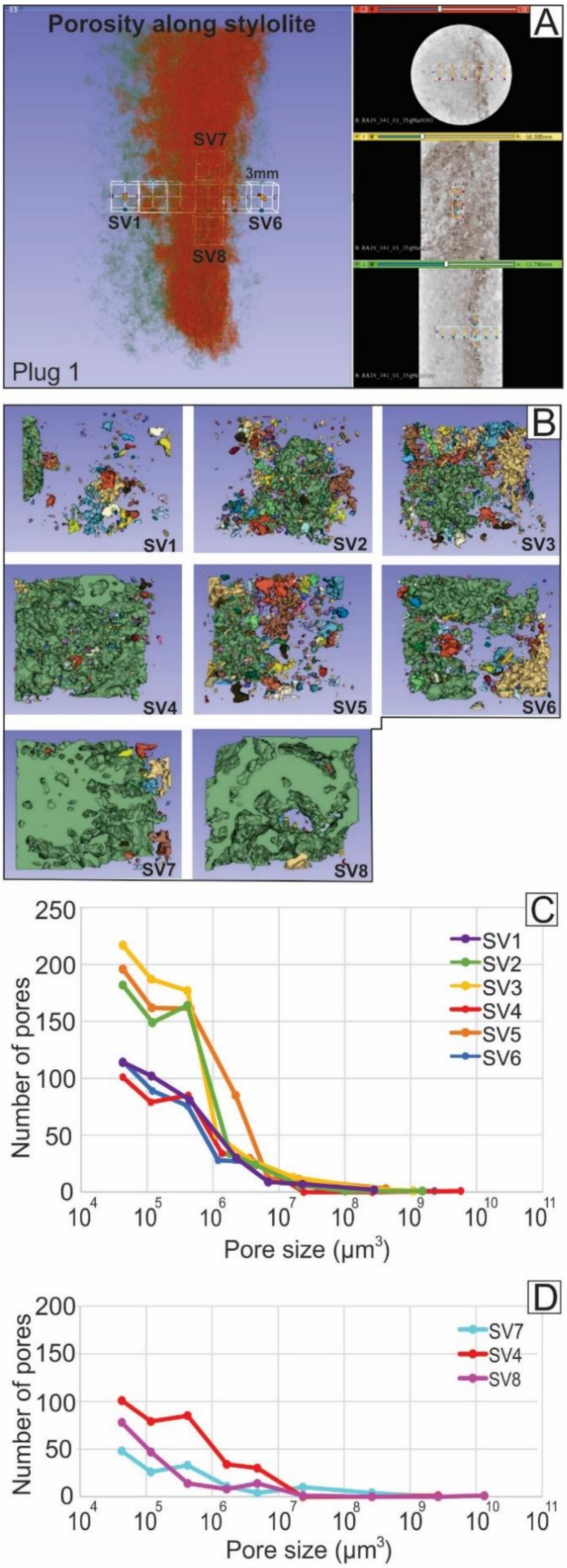

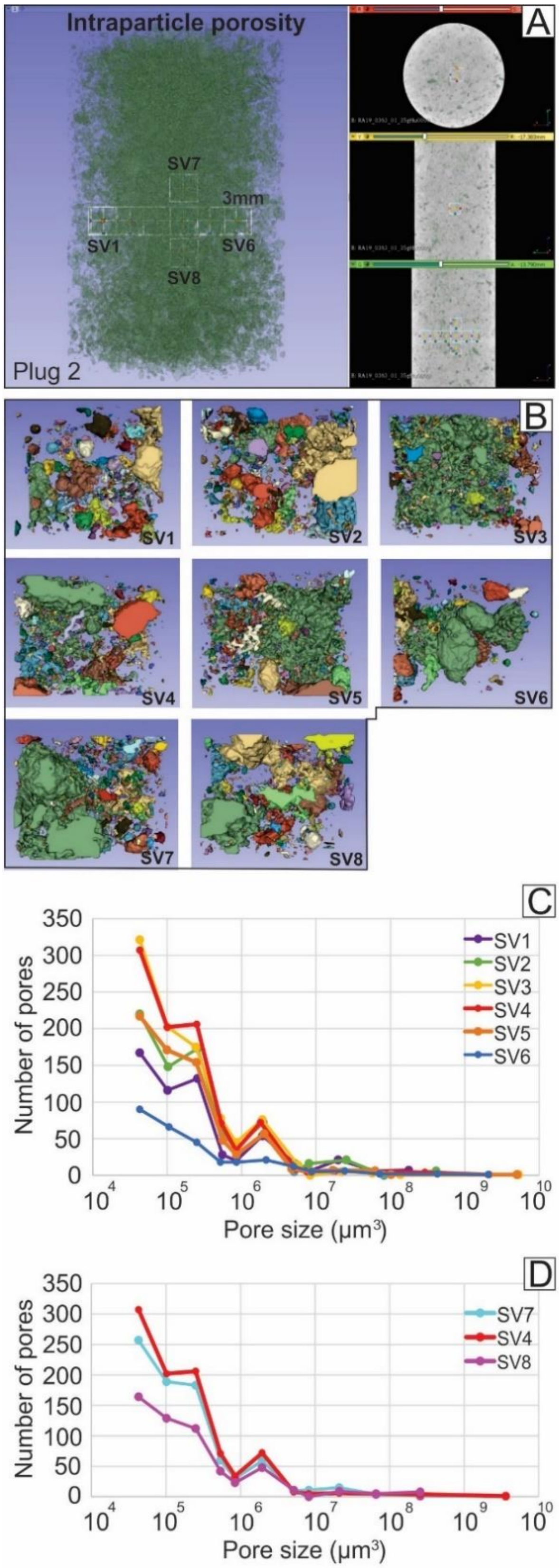

Fig. 5.10 - (A) 27 mm³ scanline cubes through stylolite in plug 1; (B) number of pores vs. pore size for six subvolumes in a scanline across stylolite horizontally; (C)

Fig. 5.11 - A) 27 mm³ scanline cubes through plugs 2; (B) number of pores vs. pore size for six subvolumes in a horizontal scanline; (C) images of pore size distributions of SV1 and

images of pore size distributions of SV1 and SV6 subvolumes in the plug; (D) number of pores vs. pore size for three subvolumes in a scanline across stylolite vertically.

SV6 subvolumes in the plugs; (D) number of pores vs. pore size for three subvolumes in a vertical scanline.

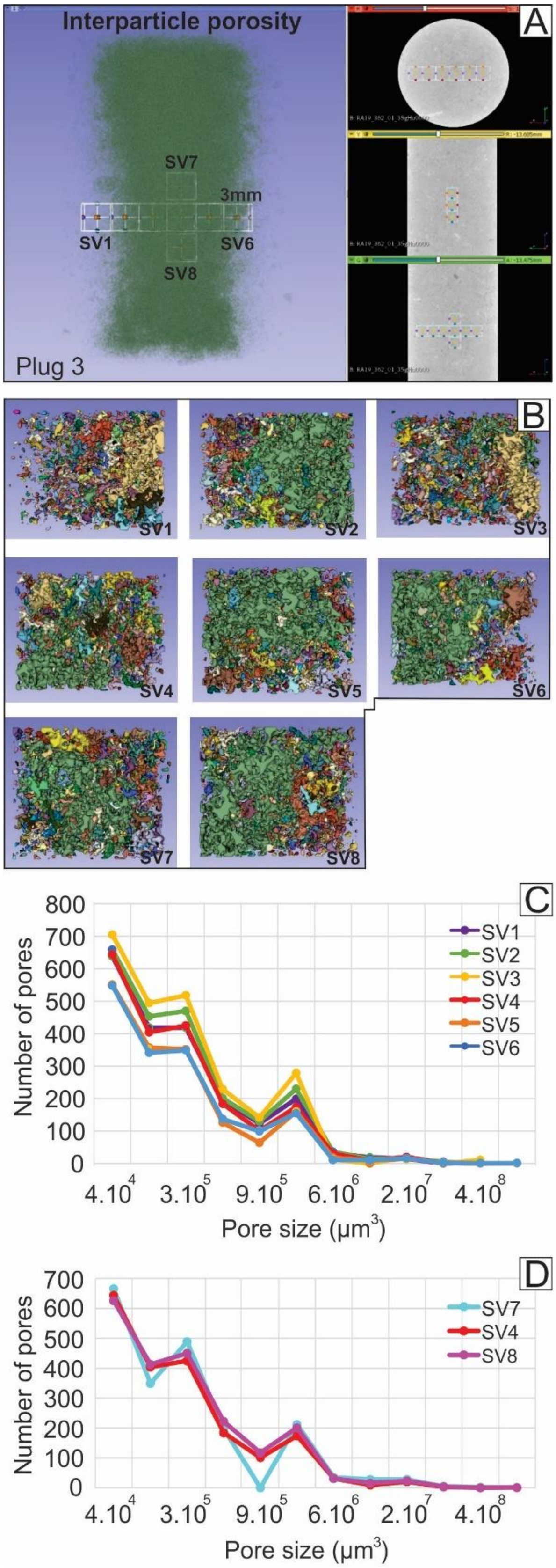

Fig. 5.12 - (A) 27 mm^3 scanline cubes through plugs 3; (B) number of pores vs. pore size for six subvolumes in a horizontal scanline; (C) images of pore size distributions of SV1 and SV6 subvolumes in the plugs; (D) number of pores vs. pore size for three subvolumes in a vertical scanline.

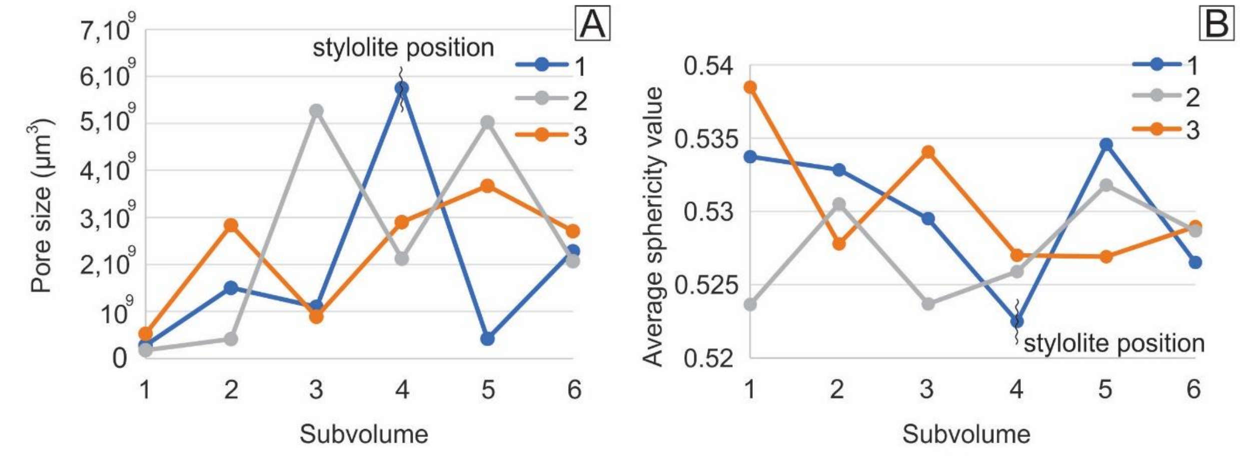

Fig. 5.13 - Diagrams of three-dimensional porosity types by plug tomography in (1) stylolite (channel porosities), (2) intraparticle (intragrain and intracrystal porosities), and (3) interparticle (intergrain and intercrystal porosities) related to (A) pore size versus subvolume scanline; (B) average sphericity value versus subvolume scanline.

5.5.1 Porosity evolution over time during carbonate diagenesis

There is a lack of studies focusing on the types of porosity in distinct stages of diagenesis on epigenic karst systems. According to Wang et al. (2002), karst-controlled diagenesis in the Ordos Basin (China) is mostly related to vuggy porosity associated with dolomite. In the shallow burial stage, new intercrystalline pores or enlarged pores were formed, but there was no specific type of dissolution shown in the early subaerial exposure stage. According to Hajikazemi et al. (2010), early diagenesis is related to the brecciation of carbonates and the presence of cavernous porosity. For Liu et al. (2016), the porosity types are mainly intergranular and intercrystalline pores in dolomites of the late diagenesis stage. For Jiu et al. (2021), the dissolution of the shallow burial period formed breccias and moldic pores, and the deep burial period is related to pore hydrothermal calcite.

In our study area, during the Campanian, the Jandaíra Formation carbonates experienced prolonged subaerial exposure due to marine regression that marked the end of marine carbonate deposition (Sampaio and Schaller, 1968). Connate marine fluids were flushed out by meteoric waters, generating diagenetic alteration of the micrites, calcite recrystallization, and the complete cementation of the carbonates (de Graaf et al., 2017). As a consequence, during this diagenetic stage, the primary porosity that developed in the shallow-water marine environments was destroyed, and the meteoric-derived fluids affected both burial diagenesis and later telogenetic exhumation, as recorded by fluid inclusion and isotopic signatures of the calcite veins (de Graaf et al., 2017). According to (Araújo et al., 2021; Fernandes et al., 2015; Rabelo et al., 2020), meteoric-derived fluids caused diffuse dissolution of carbonates mainly along bedding surfaces, faults, and stylolites.

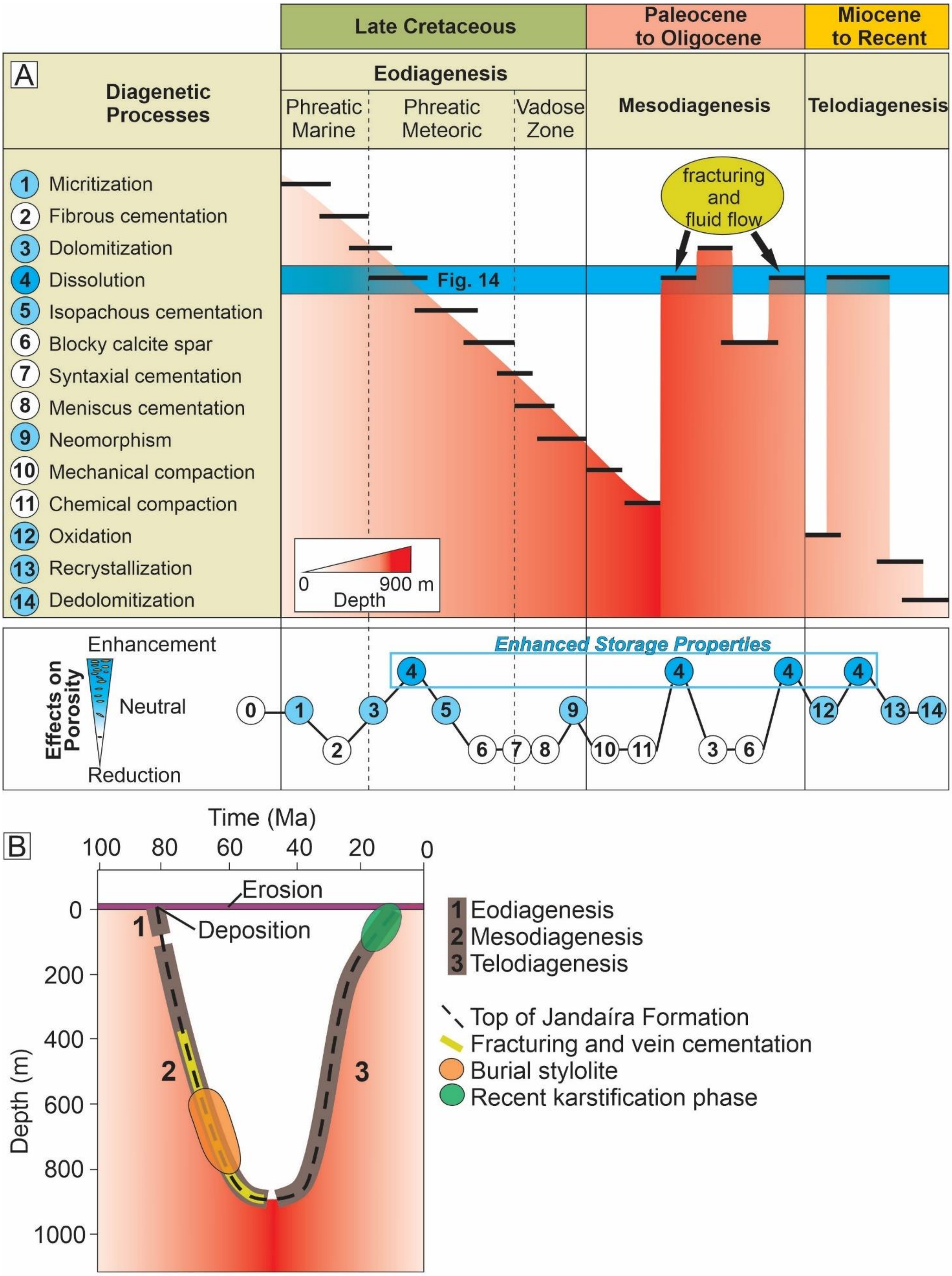

Fig. 5.14 - (A) Paragenetic sequence of the diagenetic processes affecting the carbonate succession of the Jandaíra Formation (modified after Bagni et al., 2022); (B) schematic illustration of the Jandaíra Formation over time showing diagenetic stages (modified after de Graaf et al., 2017).

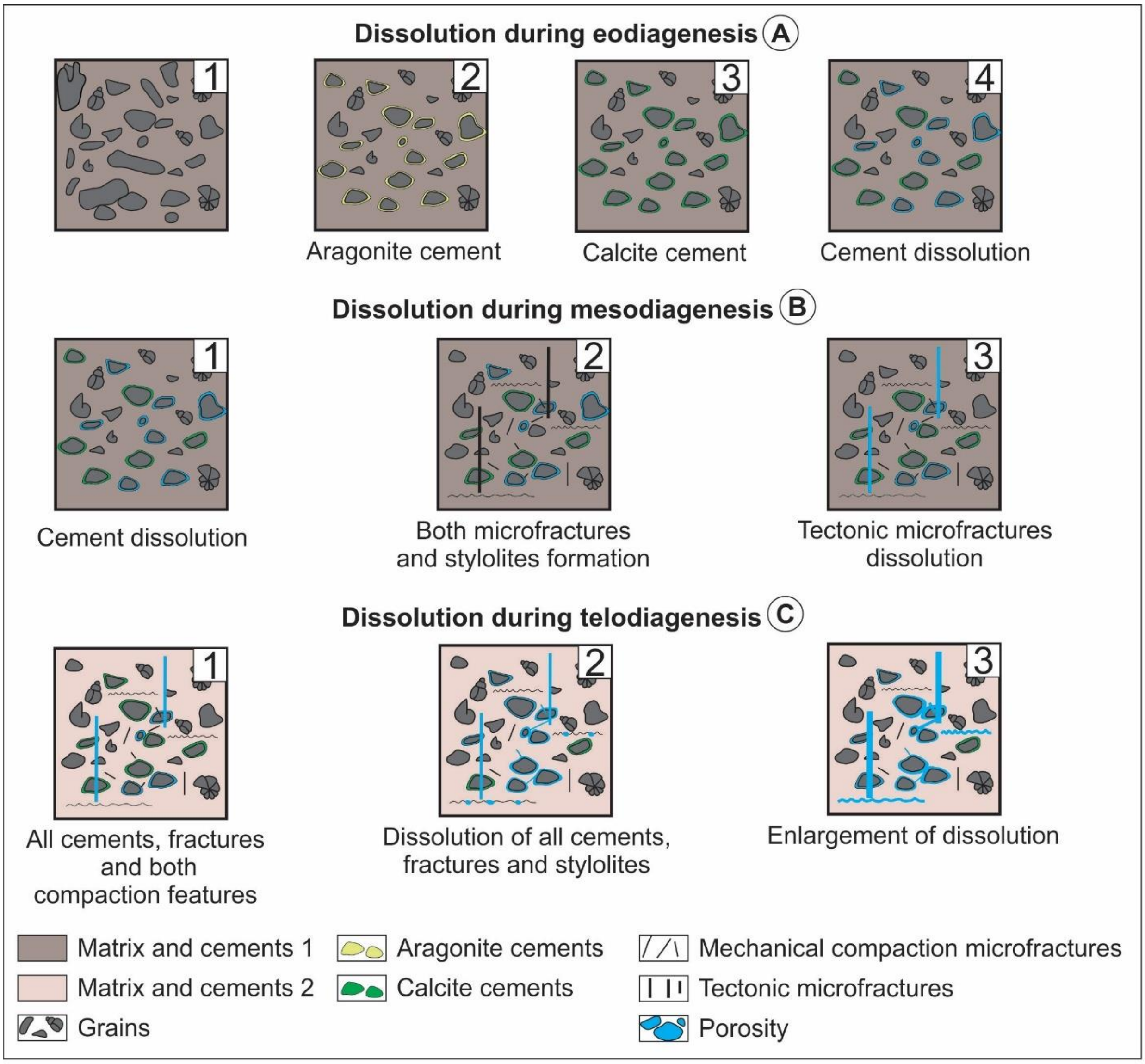

Fig. 5.15 - Evolution conceptual model at the microscale showing the origin and evolution of porosity in the three diagenetic stages: (A) eodiagenesis comprises aragonite rounded cement from the marine phreatic environment that is later recrystallized to form calcite rounded cement; (B) mesodiagenesis is represented by rotation, breakage and microfractures and stylolites formation from both mechanical and chemical compaction; (C) telodiagenesis is related to all dissolution cements from phreatic and vadose environments, fractures, stylolites and their enlargement.

Reminiscent porosity due to eodiagenesis (Fig. 5.15) is documented at the thin section scale, but subsequent diagenetic stages modified most of this porosity. The former aragonite fibrous cements, unstable outside of marine conditions, were later recrystallized to magnesium-rich calcite and retained their original fibrous shape (Flügel, 2010; Scholle and Ulmer-Scholle, 2003). This early embrittlement process (sensu La Bruna et al., 2020) caused precipitation of carbonate cements that were more susceptible to dissolution than those precipitated later in the diagenetic history of the carbonates.

In eodiagenesis, the results of detailed microscale analyses are consistent with the following time-dependent model of diagenetic evolution. Eodiagenetic porosity (Fig. 5.14A and Fig. 5.15A) included some calcite cement-filled bodies due to neomorphism, which were later completely dissolved (Fig. 5.5C). A few bioclasts present fibrous calcite cementation around partially dissolved grains (Fig. 5.5E) and microporosity within the micritic matrix, which could be replaced by calcite and dolomite (Fig. 5.5B).

During the subsequent mesodiagenetic stage, dissolution (Fig. 5.14B and Fig. 5.15B) only occurs along fractures from the strike-slip stress field with maximum N–S trending compression (Bezerra et al., 2020). Under early burial conditions, at 400–900 m depth conditions, fractures controlled the infiltration of meteoric-derived fluids from the porous Açu Formation sandstone (Fig. 5.1A) into the Jandaíra carbonates (Bertotti et al., 2017; de Graaf et al., 2017). This process was likely responsible for the partial-to-total dissolution of carbonate grains and cements (Fig. 5.7C). We documented that most of the carbonate dissolution occurred during telodiagenesis (Fig. 5.14B and Fig. 5.14C), which was likely linked to Miocene-Holocene karstification (de Graaf et al., 2017). This latest dissolution was due to acidic meteoric waters, which affected (1) unfractured carbonates; (2) stylolites; (3) fractures and veins; and (4) both bed-parallel bed interfaces and cross-stratification.

In the telodiagenesis, within the pristine, unfractured carbonates, dissolution mainly occurred on cements precipitated either under vadose or phreatic environments (Fig. 5.5E and F). The effects of dissolution that took place during telodiagenesis are also documented within dolomite (Fig. 5.6E), dedolomite minerals (Fig. 5.5D) and bioclasts (Fig. 5.6F). Evidence of dissolution is also documented along calcite veins (Fig. 5.7B), solution-enlarged fractures (Fig. 5.7C), and patches of channel porosity along stylolites (Fig. 5.7H). Microfractures due to mechanical compaction connected molds (Fig. 5.7D) likely affected the macroscale karstic pore network (Fig. 5.14).

Within stylolites, the relatively thick and continuous linings of undissolved minerals such as clays, phyllosilicates, pyrite, and organic materials are documented. The location of undissolved minerals from pressure solutions to stylolites could determine the behavior of these minerals as fluid barriers or conduits (Toussaint et al., 2018). Field evidence suggests that precipitation of minerals occurs close to stylolites (Ben-Itzhak et al., 2012; Emmanuel et al., 2010; Raynaud and Carrio-Schaffhauser, 1992). Then, the dissolution of stylolites may shut down when no place for precipitation exists (Ben-Itzhak et al., 2012).

Dissolution along planar cross-bedding and horizontal planar lamination (Fig. 5.4) are related to alternating foresets with different grain sizes and calcite cement (Araújo et al., 2021). Telogenetic dissolution along alternate foresets (microscale) is related to moldic porosity more evident in finer grained rock portions (Fig. 5.7G and H) and intracrystalline and intercrystalline porosity more concentrated on finely crystalline dolostone portions than in coarser packstone portions. (Fig. 5.7I and J).

Original microscale cavities could have been enlarged progressively over time up to hundreds of meters during the telogenetic karstification phase. This enlargement caused by meteoric dissolution occurs in pores, fractures and stylolites. The percolation of acidic waters in the vadose zone during telodiagenesis was mainly focused along fractures, which widened over time, generating vertically oriented fluid conduits. Touching vuggy pores, such as cavernous fractures, solution-enlarged fractures and microfractures connecting former moldic pores, were also formed. This dissolution could also have given rise to meter-scale porosity and conduit permeability, such as horizontal and vertical super-K horizons in carbonate successions (Hill, 1995; Klimchouk, 2012; La Bruna et al., 2021).

5.5.2 Implications of karst porosity for fluid flow and storage

Thin section observations show that both moldic and intercrystal porosities developed in the context of epigenic karst (Fig. 8), also observed by Hajikazemi et al. (2010), Jiu et al. (2021), Liu et al. (2016), and Wang and Al-Aasm (2002). The intercrystal pores are mainly localized within dolomitized facies, as also reported by Jiu et al. (2021) and Liu et al. (2016). Skeletal grains, either partially or entirely dissolved, are important to form isolated molds, which are later connected by microfractures due to mechanical compaction and/or tectonic stresses (e.g., Fig. 5.7D, E, F and Fig. 5.14B), as already documented by Panza et al. (2019). Most enlarged microfractures are filled with calcite (Fig. 5.7D), suggesting microscale meteoric water percolation (Fig. 5.14). Tectonic microfractures play a fundamental role in the development of a connected network of dissolution enlarged structural discontinuities (Fig. 5.7E and F), as already reported in the literature (He et al., 2014; Renard et al., 2009; Tang et al., 2016; Yang et al., 2019).

Intercrystal porosity and moldic porosity were caused by the leaching of dolomite (Fig. 5.5D). Araújo et al. (2021) documented that intercrystal porosity in the Jandaira Formation dolomites could have acted as pathways, helping fluid percolation through the carbonate succession. Intercrystal porosity in packstones and grainstones could have played a role during telodiagenesis (Fig. 5.6A). This porosity represents the incipit for a progressive pore enlargement up to cavernous features (e.g., Fig. 5.7A and Fig. 5.11), similar to that documented by Hajikazemi et al. (2010), Liu et al. (2016), and Wang and Al-Aasm (2002). These cavernous porosities are aligned along structural and sedimentary discontinuities at the outcrop scale (e.g., Fig. 5.4B).

The three-dimensional pore observations on rock plugs by CT methodology indicate that the highest number of pores in packstones and grainstones forms intraparticle and interparticle porosities, ranging in size from 10^4 to 107 μm^3 and 10^4 to 10^6 μm^3, respectively (Fig. 5.11C, Fig. 5.11D, Fig. 5.12C and Fig. 5.12D) in a voxel size of 35 µm. The subvolumes from scanline cubes present a higher number of interparticle pores due to isolated intercrystalline porosity than intraparticle pores. According to Bagni et al. (2022), the pore-throat radius average (µm) is less than 10 µm for isolated pores and more than 100 µm for connected pores in the Jandaíra Formation. In isolated pores, the dominant pore types are intracrystalline, intragrain, and moldic pores. The intracrystal pores correspond to the highest mean pore-throat radius. The dominant pore types in the interconnected pores are intercrystal and vug pores, which correspond to a smaller mean pore-throat radius. These observations indicate that the interparticle (intergranular and intercrystalline) porosity in the study area is characterized by well-connected pores, which leads to high permeability, as observed in the jandaíra Formation (Bagni et al., 2022) and other reservoir analogs (e.g., Anselmetti and Eberli, 1999, 1993).

CT images from three-dimensional porosity inside the stylolite zone show fewer and bigger pores than rock portions outside stylolite (Fig. 5.10), also observed in Heap et al. (2018). The sphericity of the pores in the subvolumes decreases to the center of the stylolite, where it is related to the maximum pore size (Fig. 5.13). We infer that such porosity is likely the result of stylolite formation and enlargement since the geometry of pores to the shape of the stylolite (e.g., Carozzi and Bergen, 1987; Heap et al., 2018; Raynaud and Carrio-Schaffhauser, 1992). Partial moldic and intercrystal porosities along dissolved stylolites are observed in the Jandaíra Formation, as already observed elsewhere by Bergen and Carozzi (1990). The partial moldic and intercrystal pores are the first to be formed along stylolites. The enlargement of these pores allows their connectivity and the formation of channel porosity.

Karst dissolution formation in epigenic systems can be completely distinct from that in hypogenic systems, which implies different fluid flow and storage approaches. For example, some carbonate reservoirs composed of hypogenic karst cavities are intensively cemented and have low matrix porosity and permeability (e.g., Cazarin et al., 2019; Liu et al., 2014, 2013), and consequently, storage is mainly concentrated in karst cavities and fractures (Caroline L. Cazarin et al., 2019; La Bruna et al., 2021; Pontes et al., 2021; Zhiqian et al., 2016). In our study area, packstones and grainstones bearing ooids and oncoids showed low porosity percentages unrelated to structural elements, such as fractures, veins and/or stylolites. Our data differ from those reported in Cazarin et al., 2019, which showed that the secondary porosity affecting ooids and oncoids resulted in the formation of vugs and enlarged fractures in the conduit-seal system of hypogene karst carbonates. The study area of Cazarin et al. (2019) on Neoproterozoic carbonates in northeastern Brazil is related to grainstones, microbial carbonates, siliciclastic layers and crystalline carbonate. This study showed that vugs, fractures and interparticle porosity were more abundant than those in our study area in the Jandaíra Formation.

5.5.3 Relationship between microporosity and outcrop karst features

Assessing the formation and evolution of the microporosities is essential to understanding karst dissolution features (vugs, channels, and caverns) at the outcrop scale. Moldic, intrafossil, intragrain and cavernous porosities originated or enlarged mostly during telodiagenesis due to dissolution of different types of grains and diagenetic products (calcite cement, dolomite crystals) formed during eodiagenesis, mesodiagenesis and telodiagenesis (Bagni et al., 2022; Caroline L. Cazarin et al., 2019; Flügel, 2010; Lucia, 2007). Pores in the study area were probably enlarged and linked to form touching vugs (e.g., Fig. 5.10), as observed along horizontal planar lamination and cross-bedding (Fig. 5.3 and Fig. 5.4).

Microfractures and enlarged stylolites (channel porosity) at the thin section scale can be linked to other porosities to form touching vugs but sometimes do not follow visible discontinuities. The channel porosity visible at the outcrop scale is mainly associated with subvertical fractures and, secondarily, subvertical stylolites. Both structures could be stratabound or not stratabound, and their interconnection occurs through dissolved bed-parallel stylolites (Araújo et al., 2021). Small stratabound fractures forming connected networks induced by horizontal fluid flow were also observed (e.g., Balsamo et al., 2020). Fracture and stylolite enlargement pertains to meteoric water percolation and consequent diagenetic modification. For example, fluid percolation along stylolites produces isolated pores that can be progressively linked and subsequently enlarged (Araújo et al., 2021).

Dolomitized facies exhibit the highest porosity and contain mainly intercrystalline and secondarily intracrystalline porosity in the three analyzed facies (Table 1). The dolomitized facies act as conduits of diagenetic fluids (e.g., Montanez et al., 1994), where dissolution can form caverns that strongly impact carbonate reservoir properties. According to some studies focusing on carbonate reservoir quality (e.g., Esteban and Wilson, 1993; Hallenberger et al., 2018), further dissolution and cementation can be associated with dedolomitization, which is documented in our study area, influencing porosity and permeability development (Schoenherr et al., 2018). In subaerially exposed sequences, a close link between dedolomitization and karstic processes has been noted (e.g., Nader et al., 2008; Ronchi et al., 2004; Zang et al., 2015; Rustichelli et al., 2017).

5.6 Conclusions

This study presents the link between diagenetic processes and secondary porosity, leading to epigenic karst dissolution and porosity enlargement. The main conclusions are as follows:

1) Dissolution by meteoric waters occurred at all diagenetic stages (eodiagenesis, mesodiagenesis, telodiagenesis) in an epigenic karst system. The first stage of dissolution occurred during eodiagenesis. It was related to the percolation of meteoric water in a vadose zone and the relatively deeper phreatic zone within the Jandaíra Formation during exposition periods of a Late Cretaceous carbonate platform. The second stage of dissolution occurred during mesodiagenesis, especially along fractures. The third stage of dissolution occurred during telodiagenesis in vadose and phreatic environments from the Cenozoic to recent times. It is responsible for diffuse karst dissolution features in rock grains and matrix, calcite cement and dolomite crystals, stylolites, fractures and planar and cross-stratification. These dissolution features are vugs, channels and caverns, varying from a few millimeters to hundreds of meters in size.
2) In the epigenic system, the main microporosity types are moldic, intragrain/intrafossil and intercrystal. These microporosity types in the epigenic system contrast with micropore systems derived from hypogene karst in carbonates worldwide. The hypogene karst commonly displays vugs, enlarged fractures, and interparticle porosity conduit-seal systems.
3) Fractures and stylolites are major conduits for fluid percolation in karstified carbonate reservoirs. However, our study shows that micropores in the matrix can play a key role in linking burial-related microcracks and stylolites, enhancing their connectivity and resulting in interconnected channel porosity from the microscale to the outcrop scale. Layers with stylolite zones exhibit large pore sizes, reducing pore numbers and sphericity.
4) Three-dimensional porosity indicates that inside the stylolite zone, there are fewer and larger pores than portions outside the stylolite-influenced zone. The sphericity of the pores in the center of the stylolite is related to the maximum pore size. Consequently, stylolites are good conduits for fluid flow.

5) The highest microscale porosity values in carbonate rocks affected by epigenetic dissolution are mainly associated with diagenetic processes such as cementation, compaction, recrystallization, dolomitization, dedolomitization, and dissolution.
6) In weakly deformed carbonate rocks, diagenetic processes and secondary porosity formation at the microscale can strongly influence karst dissolution at the outcrop (1-10 m) and reservoir (50-1000 m) scales. The results of this study showed the importance of studies focused on the interconnections among several diagenetic stages and karst porosity evolution. Furthermore, the outcomes of this work highlight the importance of a surface analog study to comprehend how the storage and flow properties of carbonate reservoirs can be profoundly affected by epigenic karst systems.

Acknowledgments

This research was carried out in association with the ongoing R&D project registered as ANP 20502-1, “Processos e Propriedades em Reservartórios Carbonáticos Fraturados e Carstificados – POROCARSTE 3D” (UFRN/UNB/UFRJ/UFC/Shell Brasil/ANP) – Porokarst – Processes and Properties in Fractured and Karstified Carbonate Reservoirs, sponsored by Shell Brasil under the ANP R&D levy as “Compromisso de Investimento com Pesquisa e Desenvolvimento”. The CT analyses were performed at the Federal University of Pernambuco, Brazil, supervised by Prof. Antônio Antonino.

References

Agosta, F., Alessandroni, M., Antonellini, M., Tondi, E., Giorgioni, M., 2010. From fractures to flow: A field-based quantitative analysis of an outcropping carbonate reservoir. Tectonophysics 490, 197–213. https://doi.org/10.1016/j.tecto.2010.05.005

Angelim, L.D.A., Nesi, J.R., Torres, H. H. F., Medeiros, V.C., Santos, C.A., Veiga Junior, J.P., Mendes, V.A., 2006. Geologia e recursos minerais do Estado do Rio Grande do Norte-Escala 1: 500.000, Recife: CPRM-Serviço Geológico do Brasil.

Anselmetti, F.S., Eberli, G.P., 1999. The Velocity-Deviation Log: A Tool to Predict Pore Type and Permeability Trends in Carbonate Drill Holes from Sonic and Porosity or Density Logs. Am. Assoc. Pet. Geol. Bull. 83, 450–466. https://doi.org/10.1306/00AA9BCE-1730-11D7-8645000102C1865D

Anselmetti, F.S., Eberli, G.P., 1993. Controls on sonic velocity in carbonates. Pure Appl. Geophys. PAGEOPH 141, 287–323. https://doi.org/10.1007/BF00998333

Aquilina, L., Ladouche, B., Doerfliger, N., Bakalowicz, M., 2003. Deep water circulation, residence time, and chemistry in a karst complex. Ground Water 41, 790–806.

Araújo, R.E.B., La Bruna, V., Rustichelli, A., Bezerra, F.H.R., Xavier, M.M., Audra, P., Barbosa, J.A., Antonino, A.C.D., 2021. Structural and sedimentary discontinuities control the generation of karst dissolution cavities in a carbonate sequence, Potiguar

Basin, Brazil. Mar. Pet. Geol. 123. https://doi.org/10.1016/j.marpetgeo.2020.104753

Aydin, A., 2008. ISRM suggested method for determination of the Schmidt hammer rebound hardness: revised version, in: The ISRM Suggested Methods for Rock Characterization, Testing and Monitoring: 2007-2014. Springer, Cham, pp. 25–33. https://doi.org/10.1007/978-3-319-07713-0_2

Aydin, A., Basu, A., 2005. The Schmidt hammer in rock material characterization. Eng. Geol. 81, 1–14. https://doi.org/10.1016/j.enggeo.2005.06.006

Back, W., Hanshaw, B.B., Pyle, T.E., Plummer, L.N., Weidie, A.E., 1979. Geochemical significance of groundwater discharge and carbonate solution to the formation of Caleta Xel Ha, Quintana Roo, Mexico. Water Resour. Res. 15, 1521–1535. https://doi.org/10.1029/WR015i006p01521

Bagni, F.L., Bezerra, F.H., Balsamo, F., Maia, R.P., Dall'Aglio, M., 2020. Karst dissolution along fracture corridors in an anticline hinge, Jandaíra Formation, Brazil: Implications for reservoir quality. Mar. Pet. Geol. 115, 104249. https://doi.org/10.1016/j.marpetgeo.2020.104249

Bagni, F.L., Erthal, M.M., Tonietto, S.N., Maia, R.P., Bezerra, F.H., Balsamo, F., Córdoba, V.C., de Souza, F.G., Brod, J.A., Fernandes, C.P., Fonseca, J.P.T., 2022. Karstified layers and caves formed by superposed epigenic dissolution along subaerial unconformities in carbonate rocks – Impact on reservoir-scale permeability. Mar. Pet. Geol. 138, 105523. https://doi.org/10.1016/j.marpetgeo.2022.105523

Balsamo, F., Bezerra, F.H.R., Klimchouk, A.B., Cazarin, C.L., Auler, A.S., Nogueira, F.C., Pontes, C., 2020. Influence of fracture stratigraphy on hypogene cave development and fluid flow anisotropy in layered carbonates, NE Brazil. Mar. Pet. Geol. 114, 104207. https://doi.org/10.1016/j.marpetgeo.2019.104207

Bergen, D.V., Carozzi, A.V., 1990. Experimentally-simulated stylolitic porosity in carbonate rocks. J. Pet. Geol. 13, 179–192. https://doi.org/10.1111/j.1747-5457.1990.tb00838.x

Bertotti, G., de Graaf, S., Bisdom, K., Oskam, B., Vonhof, H.B., Bezerra, F.H.R., Reijmer, J.J.., Cazarin, C.L., 2017. Fracturing and fluid-flow during post-rift subsidence in carbonates of the Jandaíra Formation, Potiguar Basin, NE Brazil. Basin Res. 29, 836–853. https://doi.org/10.1111/bre.12246

Bezerra, F.H.R., Brito Neves, B.B., Corrêa, A.C.B., Barreto, A.M.F., Suguio, K., 2008. Late Pleistocene tectonic-geomorphological development within a passive margin - The Cariat?? trough, northeastern Brazil. Geomorphology 97, 555–582. https://doi.org/10.1016/j.geomorph.2007.09.008

Bezerra, F.H.R., de Castro, D.L., Maia, R.P., Sousa, M.O.L., Moura-Lima, E.N., Rossetti, D.F., Bertotti, G., Souza, Z.S., Nogueira, F.C.C., 2020. Postrift stress field inversion in the Potiguar Basin, Brazil – Implications for petroleum systems and evolution of the equatorial margin of South America. Mar. Pet. Geol. 111, 88–104. https://doi.org/10.1016/j.marpetgeo.2019.08.001

Bezerra, F.H.R., Vita-Finzi, C., 2000. How active is a passive margin? Paleoseismicity in northeastern Brazil. Geology 28, 591. https://doi.org/10.1130/0091-7613(2000)28<591:HAIAPM>2.0.CO;2

Bloch, S., 1994. Secondary porosity in sandstones: significance, origin, relationship to subaerial unconformities, and effect on predrill reservoir quality prediction. Soc. Sediment. Geol. 137–159.

Boggs, S.J., 1992. Petrology of Sedimentary Rocks. New York, Macmillan Publishing Co.

Byrnes, A.P., 1994. Measurement of Dependent Variables –Petrophysical Variables, in: Reservoir Quality Assessment and Prediction in Clastic Rocks. SEPM (Society for Sedimentary Geology), pp. 231–246. https://doi.org/10.2110/scn.94.30.0231

Carlotto, M.A., Da Silva, R.C.B., Yamato, A.A., Trindade, W.L., Moreira, J.L.P., Fernandes, R.A.R., Ribeiro, O.J.S., Gouveia, W.P., Carminati, J.P., Qicai, D., Junfeng, Z., Da Silva-Telles, A.C., 2017. Libra: A newborn giant in the brazilian presalt province, in: AAPG Memoir. American Association of Petroleum Geologists, pp. 165–176. https://doi.org/10.1306/13572006M1133685

Carneiro, M.A., Bezerra, F.H.R., Silva, C.C.N. da, Maia, R.P., Cazarin, C.L., 2015. Controle estrutural do sistema cárstico epigenético na Formação Jandaíra, Bacia Potiguar. Geociências (São Paulo) 34, 199–209.

Carozzi, A. V., Bergen, D. Von, 1987. Stylolitic porosity in carbonates: a critical factor for deep hydrocarbon production. J. Pet. Geol. 10, 267–282. https://doi.org/10.1111/j.1747-5457.1987.tb00946.x

Cazarin, C. L., Bezerra, F.H.R., Borghi, L., Santos, R. V., Favoreto, J., Brod, J.A., Auler, A.S., Srivastava, N.K., 2019. The conduit-seal system of hypogene karst in Neoproterozoic carbonates in northeastern Brazil. Mar. Pet. Geol. 101, 90–107. https://doi.org/10.1016/j.marpetgeo.2018.11.046

Cazarin, Caroline L., Bezerra, F.H.R., Borghi, L., Santos, R. V., Favoreto, J., Brod, J.A., Auler, A.S., Srivastava, N.K., 2019. The conduit-seal system of hypogene karst in Neoproterozoic carbonates in northeastern Brazil. Mar. Pet. Geol. 101, 90–107. https://doi.org/10.1016/j.marpetgeo.2018.11.046

Chafetz, H., Barth, J., Cook, M., Guo, X., Zhou, J., 2018. Origins of carbonate spherulites: Implications for Brazilian Aptian pre-salt reservoir. Sediment. Geol. 365, 21–33. https://doi.org/10.1016/j.sedgeo.2017.12.024

Choquette, P.W., James, N.P., 1987. Diagenesis# 12. Diagenesis in Limestones -3. The deep burial environment. Geosci. Canada 14, 3–35.

Choquette, P.W., Pray, L.C., 1970. Geologic Nomenclature and Classification of Porosity in Sedimentary Carbonates. Am. Assoc. Pet. Geol. Bull. 54, 207–250. https://doi.org/10.1306/5D25C98B-16C1-11D7-8645000102C1865D

de Castro, D.L., Bezerra, F.H.R., Sousa, M.O.L., Fuck, R.A., 2012. Influence of Neoproterozoic tectonic fabric on the origin of the Potiguar Basin, northeastern Brazil and its links with West Africa based on gravity and magnetic data. J. Geodyn. 54, 29–42. https://doi.org/10.1016/J.JOG.2011.09.002

de Graaf, S., Reijmer, J.J.G., Bertotti, G. V., Bezerra, F.H.R., Cazarin, C.L., Bisdom, K., Vonhof, H.B., 2017. Fracturing and calcite cementation controlling fluid flow in the shallow-water carbonates of the Jandaíra Formation, Brazil. Mar. Pet. Geol. 80, 382–393. https://doi.org/10.1016/j.marpetgeo.2016.12.014

Dunham, R.J., 1962. Classification of Carbonate Rocks According to Depositional Textures, in: Classification of Carbonate Rocks According to Depositional Textures. AAPG Special Volumes, pp. 108–121.

Embry, A.F., Klovan, J.E., 1971. A Late Devonian reef tract on north-eastern Banks Island. Bull. Can. Pet. Geol. 19, 730–781. https://doi.org/10.35767/gscpgbull.19.4.730

Esteban, M., Wilson, J.L., 1993. Introduction to Karst Systems and Paleokarst Reservoirs, in: Introduction to Karst System and Paleokarst Reservoirs. Special Publications of SEPM, pp. 1–9.

Fairbridge, R.W., 1967. Phases of Diagenesis and Authigenesis, in: Developments in Sedimentology. pp. 19–89. https://doi.org/10.1016/S0070-4571(08)70841-0

Fernandes, A.L., Medeiros, W.E., Bezerra, F.H.R., Oliveira, J.G., Cazarin, C.L., 2015. GPR investigation of karst guided by comparison with outcrop and unmanned aerial vehicle imagery. J. Appl. Geophys. 112, 268–278. https://doi.org/10.1016/j.jappgeo.2014.11.017

Flügel, E., 2010. Microfacies of Carbonate Rocks, Second edi. ed. Springer Berlin Heidelberg, Berlin, Heidelberg. https://doi.org/10.1007/978-3-642-03796-2

Folk, R.L., 1974. The Natural History Of Crystalline Calcium Carbonate: Effect of Magnesium Content And Salinity. J. Sediment. Res. 44, 40–53. https://doi.org/10.1306/74D72973-2B21-11D7-8648000102C1865D

Folk, R.L., 1965. Some aspects of recrystallization in ancient limestones. SEPM Spec. Publ. 13, 14–48.

Ford, D., 1988. Characteristics of Dissolutional Cave Systems in Carbonate Rocks, in: Paleokarst. Springer New York, New York, NY, pp. 25–57. https://doi.org/10.1007/978-1-4612-3748-8_2

Ford, D., Williams, P., 2007. Karst Hydrogeology and Geomorphology. John Wiley & Sons Ltd,., West Sussex, England. https://doi.org/10.1002/9781118684986

Ford, D.C., Williams, P.W., 2013. Karst geomorphology and hydrology, Second edi. ed. John Wiley & Sons.

Friedman, G.M., 1964. Early Diagenesis and Lithification in Carbonate Sediments. SEPM J. Sediment. Res. 34, 777–813. https://doi.org/10.1306/74D71195-2B21-11D7-8648000102C1865D

Fu, Q., 2006. Paleokarst in Middle Devonian Winnipegosis mud mounds, subsurface of south-central Saskatchewan, Canada. Bull. Can. Pet. Geol. 54, 22–36. https://doi.org/10.2113/54.1.22

Ganai, J.A., Rashid, S.A., Romshoo, S.A., 2018. Evaluation of terrigenous input, diagenetic alteration and depositional conditions of Lower Carboniferous carbonates of Tethys Himalaya, India. Solid Earth Sci. 3, 33–49. https://doi.org/10.1016/j.sesci.2018.03.002

Garcia, G., 2014. Modelagem estratigráfica do intervalo cenomaniano-turoniano, formações Açu e Jandaíra, na borda sudoeste da Bacia Potiguar. Universidade Estadual Paulista.

Giuffrida, A., Agosta, F., Rustichelli, A., Panza, E., La Bruna, V., Eriksson, M., Torrieri, S., Giorgioni, M., 2020. Fracture stratigraphy and DFN modelling of tight carbonates, the case study of the Lower Cretaceous carbonates exposed at the Monte Alpi (Basilicata, Italy). Mar. Pet. Geol. 112, 104045. https://doi.org/10.1016/j.marpetgeo.2019.104045

Giuffrida, A., La Bruna, V., Castelluccio, P., Panza, E., Rustichelli, A., Tondi, E., Giorgioni, M., Agosta, F., 2019. Fracture simulation parameters of fractured reservoirs: Analogy with outcropping carbonates of the Inner Apulian Platform, southern Italy. J. Struct. Geol. 123, 18–41. https://doi.org/10.1016/j.jsg.2019.02.007

Goldberg, K., Kuchle, J., Scherer, C., Alvarenga, R., Ene, P.L., Armelenti, G., De Ros, L.F., 2017. Re-sedimented deposits in the rift section of the Campos Basin. Mar. Pet. Geol. 80, 412–431. https://doi.org/10.1016/j.marpetgeo.2016.11.022

Goldscheider, N., Drew, D., 2007. Methods in Karst Hydrogeology, in: IAH: International Contributions to Hydrogeology, 26. CRC Press/Balkema, Taylor & Francis Group. pp. 9–23.

Gutiérrez, F., Fabregat, I., Roqué, C., Carbonel, D., Zarroca, M., Linares, R., Yechieli, Y., García-Arnay, Á., Sevil, J., 2019. Sinkholes in hypogene versus epigene karst systems, illustrated with the hypogene gypsum karst of the Sant Miquel de Campmajor Valley, NE Spain. Geomorphology 328, 57–78. https://doi.org/10.1016/j.geomorph.2018.12.003

Hackspacher, P.C., Corsino, A.R., Srivastava, N.K., Tiriba, V.F., 1985. A Falha de Afonso Bezerra como evidência de significativo tectonismo frágil NW-SE, na Bacia Potiguar emersa – RN. Bol. do Dep. Geol. 10, 33–44.

Hajikazemi, E., Al-Aasm, I.S., Coniglio, M., 2010. Subaerial exposure and meteoric diagenesis of the Cenomanian-Turonian Upper Sarvak Formation, southwestern Iran. Geol. Soc. London, Spec. Publ. 330, 253–272. https://doi.org/10.1144/SP330.12

Hallenberger, M., Reuning, L., Schoenherr, J., 2018. Dedolomitization Potential of Fluids from Gypsum-to-Anhydrite Conversion: Mass Balance Constraints from the Late Permian Zechstein-2-Carbonates in NW Germany. Geofluids 2018, 1–9. https://doi.org/10.1155/2018/1784821

Hanshaw, B.B., Back, W., Deike, R.G., 1971. A geochemical hypothesis for dolomitization by ground water. Econ. Geol. 66, 710–724. https://doi.org/10.2113/gsecongeo.66.5.710

Hayer, J.B., 1979. Sandstone diagenesis - The hole truth. Soc. Econ. Paleontol. Mineral. 26, 127–139.

He, L., Zhao, L., Li, J., Ma, J., Lui, R., Wang, S., Zhao, W., 2014. Complex relationship between porosity and permeability of carbonate reservoirs and its controlling factors: A case study of platform facies in Pre-Caspian Basin. Pet. Explor. Dev. 41, 225–234. https://doi.org/10.1016/S1876-3804(14)60026-4

Heald, M.T.H., Larese, R.E., 1973. The Significance of the Solution of Feldspar in Porosity Development. SEPM J. Sediment. Res. 43, 458–460. https://doi.org/10.1306/74D72798-2B21-11D7-8648000102C1865D

Heap, M., Reuschlé, T., Baud, P., Renard, F., Iezzi, G., 2018. The permeability of stylolite-bearing limestone. J. Struct. Geol. 116, 81–93. https://doi.org/10.1016/j.jsg.2018.08.007

Herlinger, R., Zambonato, E.E., De Ros, L.F., 2017. Influence of Diagenesis On the Quality of Lower Cretaceous Pre-salt Lacustrine Carbonate Reservoirs from Northern Campos Basin, Offshore Brazil. J. Sediment. Res. 87, 1285–1313. https://doi.org/10.2110/jsr.2017.70

Heward, A.P., Chuenbunchom, S., Mäkel, G., Marsland, D., Spring, L., 2000. Nang Nuan oil field, B6/27, Gulf of Thailand: Karst reservoirs of meteoric or deep-burial origin? Pet. Geosci. 6, 15–27. https://doi.org/10.1144/petgeo.6.1.15

Hill, C.A., 1995. H2S-Related Porosity and Sulfuric Acid Oil-Field Karst. Am. Assoc. Pet. Geol. Bull. 74, 1685–1694.

Hopkins, J.C., 1999. Characterization of Reservoir Lithologies within Subunconformity Pools: Pekisko Formation, Medicine River Field, Alberta, Canada. Am. Assoc. Pet. Geol. Bull. 83, 1855–1870. https://doi.org/10.1306/E4FD4283-1732-11D7-8645000102C1865D

James, N.P., Choquette, P.W., 1988. Paleokarst. Springer-Verlag New York. https://doi.org/10.1007/978-1-4612-3748-8

James, N.P., Choquette, P.W., 1984. Limestones - the meteoric diagenetic environment. Geosci. Canada 11, 161–194. https://doi.org/10.1029/sc004p0045

James, N.P., Choquette, P.W., 1983. Diagenesis 6. Limestones — The Sea Floor Diagenetic Environment. Geosci. Canada 10, 162–179.

Jiu, B., Huang, W., Mu, N., Li, Y., 2021. Types and controlling factors of ordovician paleokarst carbonate reservoirs in the southeastern Ordos Basin, China. J. Pet. Sci. Eng. 198, 108162. https://doi.org/10.1016/j.petrol.2020.108162

Jonas, E.C., McBride, E.F., 1977. Diagenesis of sandstone and shale: application to exploration for hydrocarbons: Continuing Education Program Publication 1. Dep. Geol. Sci. Univ. Texas Austin, Austin, Texas. 165.

Klimchouk, A., 2012. Speleogenesis, hypogenic, in: Encyclopedia of Caves. pp. 748–765.

Klimchouk, A., Palmer, A.N., Waele, J. De, Auler, A.S., Audra, P., 2017. Hypogene karst regions and caves of the world. Springer.

Klimchouk, A.B., Ford, D.C., 2000. Types of karst and evolution of hydrogeologic setting, Speleogenesis. Evolution of Karst Aquifers. Huntsville: National Speleological Society.

La Bruna, V., Agosta, F., Lamarche, J., Viseur, S., Prosser, G., 2018. Fault growth mechanisms and scaling properties in foreland basin system: The case study of Monte Alpi, Southern Apennines, Italy. J. Struct. Geol. 116, 94–113. https://doi.org/10.1016/J.JSG.2018.08.009

La Bruna, V., Agosta, F., Prosser, G., 2017. New insights on the structural setting of the Monte Alpi area, Basilicata, Italy. Ital. J. Geosci. 136, 5–22.

La Bruna, V., Bezerra, F.H.R., Souza, V.H.P., Maia, R.P., Auler, A.S., Araujo, R.E.B., Cazarin, C.L., Rodrigues, M.A.F., Vieira, L.C., Sousa, M.O.L., 2021. High-permeability zones in folded and faulted silicified carbonate rocks – Implications for karstified carbonate reservoirs. Mar. Pet. Geol. 128, 105046. https://doi.org/10.1016/j.marpetgeo.2021.105046

La Bruna, V., Lamarche, J., Agosta, F., Rustichelli, A., Giuffrida, A., Salardon, R., Marié, L., 2020. Structural diagenesis of shallow platform carbonates: Role of early embrittlement on fracture setting and distribution, case study of Monte Alpi (Southern Apennines, Italy). J. Struct. Geol. 131. https://doi.org/10.1016/j.jsg.2019.103940

Lamarche, J., Lavenu, A.P.C., Gauthier, B.D.M., Guglielmi, Y., Jayet, O., 2012. Relationships between fracture patterns, geodynamics and mechanical stratigraphy in Carbonates (South-East Basin, France). Tectonophysics 581, 231–245. https://doi.org/10.1016/j.tecto.2012.06.042

Land, L.S., 1980. The isotopic and trace element geochemistry of dolomite: the state of the art, in: Concepts and Models of Dolomitization. SEPM Special Publication No 28. pp. 87–110.

Li, H., Bai, H., Wu, J., Zhao, H., Ma, K., 2017. A method for prevent water inrush from karst collapse column: a case study from Sima mine, China. Environ. Earth Sci. 76, 1–10. https://doi.org/10.1007/s12665-017-6831-2

Liu, H., Ma, T., Tan, X., Zeng, W., Hu, G., Xiao, D., Luo, B., Shan, S., Su, C., 2016. Origin of structurally controlled hydrothermal dolomite in epigenetic karst system during shallow burial: An example from Middle Permian Maokou Formation, central Sichuan Basin, SW China. Pet. Explor. Dev. 43, 1000–1012. https://doi.org/10.1016/S1876-3804(16)30117-3

Liu, H., Tan, X., Li, L., Ding, X., Cao, J., Yang, G., Ma, T., 2019. Eogenetic Karst in Interbedded Carbonates and Evaporites and Its Impact on Hydrocarbon Reservoir: A New Case from Middle Triassic Keikoupo Formation in Sichuan Basin, Southwest

China. J. Earth Sci. 30, 908–923. https://doi.org/10.1007/s12583-019-0888-7

Liu, Z.B., Gao, S.L., Huang, X.R., Yue, Y., Liu, S.L., Wu, S.Q., Zhang, Z.P., Yang, S.B., 2014. Formation and distribution of the Ordovician reservoir in Maigaiti Slope, Tarim basin. Acta Pet. Sin. 35, 654–663.

Liu, Z.B., Wu, S.Q., Liu, S.L., 2013. Reservoir types and main controlling factors of Ordovician in Yubei area, Tarim Basin. Acta Pet. Sin. 34, 638–646.

Lopes, J.A.G., Medeiros, W.E., La Bruna, V., de Lima, A., Bezerra, F.H.R., Schiozer, D.J., 2022. Advancements towards DFKN modelling: Incorporating fracture enlargement resulting from karstic dissolution in discrete fracture networks. J. Pet. Sci. Eng. 209, 109944. https://doi.org/10.1016/j.petrol.2021.109944

Loucks, R. G. Handford, C.R., 1992. Origin and recognition of fractures, breccias, and sediment fills in paleocave-reservoir networks. Permian Basin Sect. SEPM Publ. 92, 31–44.

Loucks, R.G., 1999. Paleocave Carbonate Reservoirs: Origins, Burial-Depth Modifications, Spatial Complexity, and Reservoir Implications. Am. Assoc. Pet. Geol. Bull. 83, 1795–1834. https://doi.org/10.1306/E4FD426F-1732-11D7-8645000102C1865D

Lucia, F.J., 2007. Carbonate reservoir characterization: An integrated approach, 2nd ed. Springer-Verlag Berlin Heidelberg. https://doi.org/10.1007/978-3-540-72742-2

Mádl-Szőnyi, J., Erőss, A., Tóth, Á., 2017. Fluid Flow Systems and Hypogene Karst of the Transdanubian Range, Hungary—With Special Emphasis on Buda Thermal Karst, in: Hypogene Karst Regions and Caves of the World. pp. 267–278. https://doi.org/10.1007/978-3-319-53348-3_17

Matos, R.M.D., 2000. Tectonic evolution of the equatorial South Atlantic, in: Mohriak, W., Taiwani, M. (Eds.), Geophysical Monograph Series. American Geophysical Union (AGU), pp. 331–354. https://doi.org/10.1029/GM115p0331

Matos, R.M.D., 1992. The Northeast Brazilian Rift System. Tectonics 11, 766–791. https://doi.org/10.1029/91TC03092

Matsuda, N.S., Viviers, M.C., 1989. Caracterizaçao do marco radioativo da parte superior da Formacao Jandaıra na Bacia Potiguar, in: In Anais Do XI Congresso Brasileiro de Paleontologia. p. Vol. 2, pp. 1029–1041.

Matthews, R.K., 1974. A process approach to diagenesis of reefs and reef associated limestones. Soc. Econ. Paleontol. Mineral. 18, 234–256.

McBride, E.F., 1977. Secondary porosity-importance. Gulf Coast Assoc. Geol. Soc. Trans. 27, 121–122.

Melo, A.C.C., de Castro, D.L., Bezerra, F.H.R., Bertotti, G., 2016. Rift fault geometry and evolution in the Cretaceous Potiguar Basin (NE Brazil) based on fault growth models. J. South Am. Earth Sci. 71, 96–107. https://doi.org/10.1016/j.jsames.2016.07.006

Menezes, D.F., Bezerra, F.H., Balsamo, F., Arcari, A., Maia, R.P., Cazarin, C.L., 2020. Subsidence rings and fracture pattern around dolines in carbonate platforms – Implications for evolution and petrophysical properties of collapse structures. Mar. Pet. Geol. 113, 104113. https://doi.org/10.1016/j.marpetgeo.2019.104113

Monroe, W.H., 1970. A glossary of Karst terminology. https://doi.org/10.3133/wsp1899K

Moore, C., 2001. Carbonate reservoirs: Porosity, Evolution and Diagenesis in a Sequence Stratigraphic Framework.

Moore, C.H., 1989. Carbonate diagenesis and porosity. Elsevier.

Moore, C.H., Wade, W.J., 2013. Carbonate reservoirs: Porosity and diagenesis in a sequence stratigraphic framework. Newnes.

Morais Neto, J.M., Hegarty, K., Alkmin, F., Matos, R., Karner, G., 2000. Uplift and erosion in the Borborema Province, Northeast Brazil: Insights from Apatite Fission Track Analysis, in: 31st International Geological Congress. Rio de Janeiro.

Morais Neto, J.M., Hegarty, K.A., Karner, G.D., Alkmim, F.F., 2009. Timing and mechanisms for the generation and modification of the anomalous topography of the Borborema Province, northeastern Brazil. Mar. Pet. Geol. 26, 1070–1086. https://doi.org/10.1016/j.marpetgeo.2008.07.002

Morse, J.W., Mackenzie, F.T., 1990. Geochemistry of sedimentary carbonates. Elsevier Scientific Publication Co., New York, USA.

Nader, F.H., Swennen, R., Keppens, E., 2008. Calcitization/dedolomitization of Jurassic dolostones (Lebanon): results from petrographic and sequential geochemical analyses. Sedimentology 55, 1467–1485. https://doi.org/10.1111/j.1365-3091.2008.00953.x

Palmer, A.N., 1991. Origin and morphology of limestone caves. Geol. Soc. Am. Bull. 103, 1–21.

Palmer, T.J., Hudson, J.D., Wilson, M.A., 1988. Palaeoecological evidence for early aragonite dissolution in ancient calcite seas. Nature 335, 809–810.

Panza, E., Agosta, F., Rustichelli, A., Vinciguerra, S.C., Ougier-Simonin, A., Dobbs, M., Prosser, G., 2019. Meso-to-microscale fracture porosity in tight limestones, results of an integrated field and laboratory study. Mar. Pet. Geol. 103, 581–595. https://doi.org/10.1016/j.marpetgeo.2019.01.043

Pessoa Neto, O.C., Soares, U.M., Silva, J.G.F., Roessner, E.H., Florêncio, C.P., Souza, C.A.V., 2007. Bacia Potiguar. Bol. Geociências da Petrobras 15, 357–369.

Pisani, L., Antonellini, M., Bezerra, F.H.R., Carbone, C., Auler, A.S., Audra, P., La Bruna, V., Bertotti, G., Balsamo, F., Pontes, C.C.C., De Waele, J., 2022. Silicification, flow pathways, and deep-seated hypogene dissolution controlled by structural and stratigraphic variability in a carbonate-siliciclastic sequence (Brazil). Mar. Pet. Geol. 139, 105611. https://doi.org/10.1016/j.marpetgeo.2022.105611

Pontes, C.C.C., Bezerra, F.H.R., Bertotti, G., La Bruna, V., Audra, P., De Waele, J., Auler, A.S., Balsamo, F., De Hoop, S., Pisani, L., 2021. Flow pathways in multiple-direction fold hinges: Implications for fractured and karstified carbonate reservoirs. J. Struct. Geol. 146, 104324. https://doi.org/10.1016/j.jsg.2021.104324

Porpino, K.O., Junior, V.S., Santos, M.F.C.F., 2009. Lajedo de Soledade, Apodi, RN. Ocorrência peculiar de megafauna fóssil quaternária no Nordeste do Brasil., in: Sítios Geológicos e Paleontológicos Do Brasil. CPRM, pp. 403–412.

Rabelo, J.G., Maia, R.P., Bezerra, F.H.R., Silva, C.C.N., 2020. Karstification and fluid flow in carbonate units controlled by propagation and linkage of mesoscale fractures, Jandaíra Formation, Brazil. Geomorphology 357, 107090. https://doi.org/10.1016/j.geomorph.2020.107090

Rabelo, J.G., Silva, A.T., Bezerra, F.H.R., Moraes, A., 2015. Modelagem numérica da deformação em carbonatos e implicações na formação de carste. Geol. USP. Série Científica 15, 99. https://doi.org/10.11606/issn.2316-9095.v15i2p99-110

Rajaram, H., Cheung, W., Chaudhuri, A., 2009. Natural analogs for improved understanding of coupled processes in engineered earth systems: examples from karst system evolution. Curr. Sci. 97, 1162–1176.

Raynaud, S., Carrio-Schaffhauser, E., 1992. Rock matrix structures in a zone influenced by a stylolite. J. Struct. Geol. 14, 973–980. https://doi.org/10.1016/0191-8141(92)90028-U

Reis, J.A. dos, de Castro, D.L., de Jesus, T.E.S., Filho, F.P.L., 2014. Characterization of collapsed paleocave systems using GPR attributes. J. Appl. Geophys. 103, 43–56. https://doi.org/10.1016/j.jappgeo.2014.01.007

Renard, F., Bernard, D., Desrues, J., Ougier-Simonin, A., 2009. 3D imaging of fracture propagation using synchrotron X-ray microtomography. Earth Planet. Sci. Lett. 286, 285–291. https://doi.org/10.1016/j.epsl.2009.06.040

Ronchi, P., Jadoul, F., Savino, R., 2004. Quaternary dedolomitization along fracture systems in a late triassic Dolomitized platform (Western Southern Alps, Italy). Carbonates and Evaporites 19, 51–66. https://doi.org/10.1007/BF03175195

Rustichelli, A., Agosta, F., Tondi, E., Spina, V., 2013. Spacing and distribution of bed-perpendicular joints throughout layered, shallow-marine carbonates (Granada Basin, southern Spain). Tectonophysics 582, 188–204. https://doi.org/10.1016/J.TECTO.2012.10.007

Rustichelli, A., Iannace, A., Tondi, E., Di Celma, C., Cilona, A., Giorgioni, M., Parente, M., Girundo, M., Invernizzi, C., 2017. Fault-controlled dolomite bodies as palaeotectonic indicators and geofluid reservoirs: New insights from Gargano Promontory outcrops. Sedimentology 64, 1871–1900. https://doi.org/10.1111/sed.12378

Sampaio, A. V., Schaller, H., 1968. Introdução à estratigrafia cretácea da Bacia Potiguar. Bol. Técnico da Petrobrás 11, 19–44.

Santos Filho, M.A.B., Piovesan, E.K., Fauth, G., Srivastava, N.K., 2015. Paleoenvironmental interpretation through the analysis of ostracodes and carbonate microfacies: study of the Jandaíra Formation, Upper Cretaceous, Potiguar Basin. Brazilian J. Geol. 45, 23–34. https://doi.org/10.1590/23174889201500010002

Schmidt, V., Mcdonald, D.A., 1979. The role of secondary porosity in the course of sandstone diagenesis. SEPM Spec. Publ. 26, 175–207.

Schmidt, V., McDonald, D.A., 1979. The role of secondary porosity in the course of sandstone diagenesis. Soc. Econ. Paleontol. Mineral. 26, 175–207.

Schoenherr, J., Reuning, L., Hallenberger, M., Lüders, V., Lemmens, L., Biehl, B.C., Lewin, A., Leupold, M., Wimmers, K., Strohmenger, C.J., 2018. Dedolomitization: review and case study of uncommon mesogenetic formation conditions. Earth-Science Rev. 185, 780–805. https://doi.org/10.1016/j.earscirev.2018.07.005

Scholle, P.A., Ulmer-Scholle, D.S., 2003. A color guide to the petrography of carbonate rocks : grains, textures, porosity, diagenesis. AAPG.

Silva, O.L., Bezerra, F.H.R., Maia, R.P., Cazarin, C.L., 2017. Karst landforms revealed at various scales using LiDAR and UAV in semi-arid Brazil: Consideration on karstification processes and methodological constraints. Geomorphology 295, 611–630. https://doi.org/10.1016/J.GEOMORPH.2017.07.025

Stafford, K.W., Nance, R., Rosales-Lagarde, L., Boston, P.J., 2008. Epigene and hypogene karst manifestations of the Castile Formation: Eddy County, New Mexico and Culberson County, Texas, USA. Int. J. Speleol. 37, 83–98.

Stoessell, R.K., Moore, C.H., 1983. Chemical Constraints and Origins of Four Groups of Gulf Coast Reservoir Fluids. Am. Assoc. Pet. Geol. Bull. 67, 896–906. https://doi.org/10.1306/03B5B6C8-16D1-11D7-8645000102C1865D

Sujkowski, Z.L., 1958. Diagenesis. Am. Assoc. Pet. Geol. Bull. 42, 2692–2717.

https://doi.org/10.1306/0BDA5C09-16BD-11D7-8645000102C1865D

Sun, C., Yu Hong-feng, Wang Huai-sheng, Liu Hu, Zhang Zheng-hong, Han Jie, Luo Xin-sheng, 2012. Vugular Formation of Carbonates in Ordovician Yingshan Reservoir in Tazhong Northern Slope of Tarim Basinn. Nat. Gas Geosci. 23, 230–236.

Tang, Z., Zhai, C., Zou, Q., Qin, L., 2016. Changes to coal pores and fracture development by ultrasonic wave excitation using nuclear magnetic resonance. Fuel 186, 571–578. https://doi.org/10.1016/j.fuel.2016.08.103

Taylor, J.M., 1950. Pore-Space Reduction in Sandstones. Am. Assoc. Pet. Geol. Bull. 34, 701–716. https://doi.org/10.1306/3D933F47-16B1-11D7-8645000102C1865D

Tian, F., Di, Q., Jin, Q., Cheng, F., Zhang, W., Lin, L., Wang, Y., Yang, D., Niu, C., Li, Y., 2019. Multiscale geological-geophysical characterization of the epigenic origin and deeply buried paleokarst system in Tahe Oilfield, Tarim Basin. Mar. Pet. Geol. 102, 16–32. https://doi.org/10.1016/j.marpetgeo.2018.12.029

Tibana, P., Terra, G.J.S., 1981. Seqüências carbonáticas do cretáceo na Bacia Potiguar. Bol. Técnico da Petrobrás 24, 174–183.

Tucker, M.E., 2001. Sedimentary petrology : an introduction to the origin of sedimentary rocks, 3rd ed. Blackwell Science.

Tucker, M.E., Wright, V.P., 1990. Diagenetic Processes, Products and Environments, in: Carbonate Sedimentology. Blackwell Publishing Ltd., Oxford, UK, pp. 314–364. https://doi.org/10.1002/9781444314175.ch7

Upchurch, S., Scott, T.M., Alfieri, M.C., Fratesi, B., Dobecki, T.L., 2019. Epigene and Hypogene Karst, in: The Karst Systems of Florida. Springer, Cham., pp. 359–441. https://doi.org/10.1007/978-3-319-69635-5_8

Vacher, H.L., Mylroie, J.E., 2002. Eogenetic karst from the perspective of an equivalent porous medium. Carbonates and Evaporites 17, 182–196. https://doi.org/10.1007/BF03176484

Vahrenkamp, V.C., Swar, P.K., 1994. Late Cenozoic dolomites of the Bahamas: metastable analogues for the genesis of ancient platform dolomites, in: Special Publications of Internacional Association of Sedimentologists. pp. 133–153.

Wang, B., Al-Aasm, I.S., 2002. Karst-controlled diagenesis and reservoir development: Example from the Ordovician main-reservoir carbonate rocks on the eastern margin of the Ordos basin, China. Am. Assoc. Pet. Geol. Bull. 86, 1639–1658.

Weidlich, O., 2010. Meteoric diagenesis in carbonates below karst unconformities: Heterogeneity and control factors. Geol. Soc. Spec. Publ. 329, 291–315. https://doi.org/10.1144/SP329.12

White, W.B., 1977. Role of solution kinetics in the development of karst aquifers. Int. Assoc. Hydrogeol. 12, 503–517.

Wilson, M.D., Stanton, P.T., 1994. Diagenetic mechanisms of porosity and permeability reduction and enhancement. Soc. Sediment. Geol. 3–44.

Worden, R.H., Burley, S.D., 2003. Sandstone diagenesis: the evolution of sand to stone. Sandstone Diagenes. Recent Anc. 4, 3–44.

Xavier Neto, P., Medeiros, W.E., 2006. A practical approach to correct attenuation effects in GPR data. J. Appl. Geophys. 59, 140–151. https://doi.org/10.1016/j.jappgeo.2005.09.002

Yang, Y., Zheng, K., Li, Zhiwei, Li, Zenghua, Si, L., Hou, S., Duan, Y., 2019. Experimental study on pore-fracture evolution law in the thermal damage process of coal. Int. J. Rock Mech. Min. Sci. 116, 13–24. https://doi.org/10.1016/j.ijrmms.2019.03.004

Youssef, A.A.A., Awotunde, A.A., 2019. Modelling fluid flow in karst reservoirs using Darcy Model with estimated permeability distribution. Comput. Geosci. 133, 104311. https://doi.org/10.1016/j.cageo.2019.104311

Zang, H., Zheng, X., Jia, Z., Chen, J., Qin, Z., 2015. The impact of hydrogeochemical processes on karst groundwater quality in arid and semiarid area: a case study in the Liulin spring area, north China. Arab. J. Geosci. 8, 6507–6519. https://doi.org/10.1007/s12517-014-1679-1

Zhang, J., Zhou, J., Fu, L., Li, H., Lou, D., 2020. Karstification of Ordovician carbonate reservoirs in Huanghua depression and its control factors. Carbonates and Evaporites 35, 42. https://doi.org/10.1007/s13146-020-00572-x

Zhiqian, G., Zhongbao, L., Shanlin, G., Qunan, D., Shiqiang, W., Shilin, L., 2016. Characteristics and genetic models of Lower Ordovician carbonate reservoirs in southwest Tarim Basin, NW China. J. Pet. Sci. Eng. 144, 99–112. https://doi.org/10.1016/j.petrol.2016.03.007

Zoback, M.D., 2007. Reservoir Geomechanics. Cambridge University Press.

6. CONCLUSÕES

O presente estudo combina dados de campo e laboratório para caracterizar a natureza, distribuição e desenvolvimento de estilólitos, fraturas e descontinuidades primárias como também as feições diagenéticas responsáveis pela dissolução cárstica que afeta as rochas carbonáticas do Lajedo Soledade localizados na Formação Jandaíra da Bacia Potiguar (Brasil).

6.1 Carstificação associada a descontinuidades estruturais e sedimentares

1) As dissoluções cársticas (vugs, canais e cavernas) seguem as descontinuidades estruturais (por exemplo, fraturas e estilólitos perpendiculares ao acamamemento) e as descontinuidades sedimentares (por exemplo, estilólitos paralelos ao acamamento, estratificações plano-paralela e cruzadas tangencial na base). A evidência de dissolução ao longo de estratificações tangenciais provam a ausência de controle dos níveis de paleoágua.
2) Os estilólitos perpendiculares ao acamamento são delimitados pelas camadas (stratabound) ou cortando camadas (non-stratabound). Ambos os estilólitos são alargados pela dissolução e podem cortar camadas formando condutos e posteriormente cavernas.
3) A ausência de dissolução ao longo de alguns estilólitos paralelos às camadas podem servir como barreiras ao fluxo de fluido na horizontal. No entanto, já outros estilólitos paralelos às camadas são dissolvidos e podem gerar porosidade em canal e assim contribuir para a percolação de fluido.
4) Os estilólitos podem ser isolados ou ramificados. Ambos os tipos podem formar zonas estilóliticas que são zonas de maior conecção de poros, sendo zonas de maior porosidade e permeabilidade.
5) Em microescala, a formação e desenvolvimento da dissolução ao longo dos estilólitos. Pequenos poros isolados são formados ao longo do estilólito, sendo posteriomente alargados e conectados uns aos outros. Esse processo leva a formação da porosidade em canal ao longo dos estilólitos, que podem ser alargados com aumento da percolação de fluido, como também explicar a formação de condutos verticais e horizontais, e cavernas.
6) A dissolução ao longo das estratificações plano-paralela e tangencial é relacionada a diferença de tamanho de grãos e/ou diferentes tipos de cimento nos diferentes foresets.

6.2 Carstificação associada a eventos diagenéticos

1) A dissolução por águas meteóricas no sistema cárstico epigênico ocorre nos três eventos diagenéticos (eodiagênese, mesodiagênese e telodiagênese).
   a) O primeiro evento de dissolução, durante a eodiagênese, ocorre devido à percolação de água meteórica em zona vadosa e freática, gerando precipitação de cimento de aragonita ao redor dos grãos e recristalização de cimento de calcita. A transição do cimento de aragonita para calcita gera porosidade em algumas porções.
   b) O segundo evento de dissolução, na mesodiagênese, atua nas fraturas tectônicas.
   c) O terceiro evento, durante a telodiagênese, corresponde ao evento de maior exposição e de maior formação de dissolução devido à dissolução de diversas feições diagenéticas (como estilólitos paralelos ao acamamento, fraturas por compactação, diferentes tipos de cimentos e cristais de dolomita), feições estruturais (fraturas, estilólitos perpendiculares ao acamamento) e descontinuidades estruturais (estratificação plano-paralela e tangencial). Todas essas dissoluções contribuem para a formação e desenvolvimento de vugs, canais e cavernas, que variam de milímetros a centenas de metros de tamanho.
2) As principais microporosidades são móldica, intragrão/intrafóssil e intercristal. Esses tipos de microporosidade contrastam com sistemas de microporos que afetam carbonatos carstificados hipogênicos em outros afloramentos em todo o mundo, que comumente exibem vugs, fraturas ampliadas e sistemas de condutos ou selos pela porosidade interpartícula.
3) As fraturas e estilólitos são os maiores condutores para percolação de fluidos em reservatórios carbonáticos. No entanto, nosso estudo mostra que as microporosidades na matrix da rocha também podem ter um papel importante para a conexão entre microcracks e estilólitos, e contribuem na geração da porosidade em canal, começando da escala microscópio e se expandindo até a escala de afloramento. Camadas com estilólitos apresentam poros maiores, mas menor quantidade de poros.
4) A porosidade 3D indica que o estilólito dentro da zona estilolítica apresenta poros grandes, visto que estes estão conectados, porém em menor quantidade quando comparado a porções fora da zona estilolítica. A esfericidade dos poros no centro

da zona estilolítica é relacionada ao maior tamanho de poro. Consequentemente, estilólitos são bons condutores de fluido.

5) A alta porosidade em microescala nas rochas afetadas pela dissolução epigênica são principalmente associadas aos processos diagenéticos como a cimentação, compactação, recristalização, dolomitização, dedolomitização e dissolução.
6) Em rochas carbonáticas fracamente deformadas, processos diagenéticos e a formação de porosidade em microescala podem influenciar fortemente a dissolução cárstica nas escalas de afloramento (1-10 m) e reservatório (50 – 1000 m). Os resultados deste estudo mostram a importância de estudos focados nas interconexões entre vários estágios diagenéticos e evolução da porosidade cárstica. Além disso, os resultados deste trabalho também destacam a importância de um estudo análogo de superfície para compreender como as propriedades de armazenamento e fluxo de reservatórios carbonáticos podem ser profundamente afetadas por sistemas cársticos epigênicos.

6.3 Considerações finais

Estudar a formação e distribuição de espaços porosos ainda é um desafio para a exploração reservatórios de geofluidos (por exemplo, água subterrânea e injeção de CO_2 no subsolo), uma vez que apresentam padrões heterogêneos tanto em escalas de lâmina quanto em afloramento. Além disso, há uma lacuna de conhecimento sobre a correlação de amostras de rocha microporosas em escala milimétrica e centimétrica para afloramentos macroporosos em escala métrica. Esses espaços porosos, também denominado de porosidade secundária, são frequentemente associados a problemas e desafios durante a perfuração de poços, tais como perdas de fluido de circulação e queda de coluna de perfuração.

Muitos estudos focam em feições estruturais como principais controladores de porosidade e permeabilidade. A relevância desse trabalho com a demanda atual dos reservatórios de petróleo é mostrar que o carste não ocorre apenas ao longo de fraturas. Há carste ao longo de estilólitos e as estratificações plano-paralela e cruzadas, ambas também servindo como condutos de fluidos.

Além disso, os reservatórios de rochas carbonáticas se diferem dos demais (por exemplo, reservatórios associados a fraturamento de rochas metamórficas fraturadas) por apresentarem porosidade espalhada ao longo dos grãos, cimento e matriz, sendo estas desprezadas em muitos estudos. Essa porosidade, não vista em macro e meso escala tem também sua importância no processos de desenvolvimento de porosidade, alargamento e conexão de feições estruturais e consequentemente o aumento de porosidade, gerando o carste.

Na área da engenharia, muitos estudos fazem simulações numéricas e arranjo de poros em análise 3D. No entanto, a formação e arranjo dos poros 3D tem pouca explicação do ponto de vista geológico. É necessário um estudo mais detalhado do padrão de microporosidade, associando características 3D a meso escala, como por exemplo os microporos e sua influência no fluxo de fluido de estilólitos paralelos ao acamamento, como também a influência no fluxo de fluido em rochas que apresentam porosidade intercristal dominante.

REFERÊNCIAS

Agosta, F., Alessandroni, M., Antonellini, M., Tondi, E., Giorgioni, M., 2010. From fractures to flow: A field-based quantitative analysis of an outcropping carbonate reservoir. Tectonophysics 490, 197–213. https://doi.org/10.1016/j.tecto.2010.05.005

Angelim, L.D.A., Nesi, J.R., Torres, H. H. F., Medeiros, V.C., Santos, C.A., Veiga Junior, J.P., Mendes, V.A., 2006. Geologia e recursos minerais do Estado do Rio Grande do Norte-Escala 1: 500.000, Recife: CPRM-Serviço Geológico do Brasil.

Aquilina, L., Ladouche, B., Doerfliger, N., Bakalowicz, M., 2003. Deep water circulation, residence time, and chemistry in a karst complex. Ground Water 41, 790–806.

Araújo, R.E.B., La Bruna, V., Rustichelli, A., Bezerra, F.H.R., Xavier, M.M., Audra, P., Barbosa, J.A., Antonino, A.C.D., 2021. Structural and sedimentary discontinuities control the generation of karst dissolution cavities in a carbonate sequence, Potiguar Basin, Brazil. Mar. Pet. Geol. 123. https://doi.org/10.1016/j.marpetgeo.2020.104753

Aydin, A., 2008. ISRM suggested method for determination of the Schmidt hammer rebound hardness: revised version, in: The ISRM Suggested Methods for Rock Characterization, Testing and Monitoring: 2007-2014. Springer, Cham, pp. 25–33. https://doi.org/10.1007/978-3-319-07713-0_2

Aydin, A., Basu, A., 2005. The Schmidt hammer in rock material characterization. Eng. Geol. 81, 1–14. https://doi.org/10.1016/j.enggeo.2005.06.006

Back, W., Hanshaw, B.B., Pyle, T.E., Plummer, L.N., Weidie, A.E., 1979. Geochemical significance of groundwater discharge and carbonate solution to the formation of Caleta Xel Ha, Quintana Roo, Mexico. Water Resour. Res. 15, 1521–1535. https://doi.org/10.1029/WR015i006p01521

Bertotti, G., de Graaf, S., Bisdom, K., Oskam, B., Vonhof, H.B., Bezerra, F.H.R., Reijmer, J.J.., Cazarin, C.L., 2017. Fracturing and fluid-flow during post-rift subsidence in carbonates of the Jandaíra Formation, Potiguar Basin, NE Brazil. Basin Res. 29, 836–853. https://doi.org/10.1111/bre.12246

Bezerra, F.H.R., Brito Neves, B.B., Corrêa, A.C.B., Barreto, A.M.F., Suguio, K., 2008. Late Pleistocene tectonic-geomorphological development within a passive margin - The Cariat?? trough, northeastern Brazil. Geomorphology 97, 555–582. https://doi.org/10.1016/j.geomorph.2007.09.008

Bezerra, F.H.R., de Castro, D.L., Maia, R.P., Sousa, M.O.L., Moura-Lima, E.N., Rossetti, D.F., Bertotti, G., Souza, Z.S., Nogueira, F.C.C., 2020. Postrift stress field inversion in the Potiguar Basin, Brazil – Implications for petroleum systems and evolution of the equatorial margin of South America. Mar. Pet. Geol. 111, 88–104. https://doi.org/10.1016/j.marpetgeo.2019.08.001

Bezerra, F.H.R., Vita-Finzi, C., 2000. How active is a passive margin? Paleoseismicity in northeastern Brazil. Geology 28, 591. https://doi.org/10.1130/0091-7613(2000)28<591:HAIAPM>2.0.CO;2

Bloch, S., 1994. Secondary porosity in sandstones: significance, origin, relationship to subaerial unconformities, and effect on predrill reservoir quality prediction. Soc. Sediment. Geol. 137–159.

Boggs, S.J., 1992. Petrology of Sedimentary Rocks. New York, Macmillan Publishing Co.

Byrnes, A.P., 1994. Measurement of Dependent Variables –Petrophysical Variables, in: Reservoir Quality Assessment and Prediction in Clastic Rocks. SEPM (Society for Sedimentary Geology), pp. 231–246. https://doi.org/10.2110/scn.94.30.0231

Carlotto, M.A., Da Silva, R.C.B., Yamato, A.A., Trindade, W.L., Moreira, J.L.P., Fernandes, R.A.R., Ribeiro, O.J.S., Gouveia, W.P., Carminati, J.P., Qicai, D., Junfeng, Z., Da Silva-Telles, A.C., 2017. Libra: A newborn giant in the brazilian presalt province, in: AAPG Memoir. American Association of Petroleum Geologists, pp. 165–176. https://doi.org/10.1306/13572006M1133685

Carneiro, M.A., Bezerra, F.H.R., Silva, C.C.N. da, Maia, R.P., Cazarin, C.L., 2015. Controle estrutural do sistema cárstico epigenético na Formação Jandaíra, Bacia Potiguar. Geociências (São Paulo) 34, 199–209.

Cazarin, C.L., Bezerra, F.H.R., Borghi, L., Santos, R. V., Favoreto, J., Brod, J.A., Auler, A.S., Srivastava, N.K., 2019. The conduit-seal system of hypogene karst in Neoproterozoic carbonates in northeastern Brazil. Mar. Pet. Geol. 101, 90–107. https://doi.org/10.1016/j.marpetgeo.2018.11.046

Chafetz, H., Barth, J., Cook, M., Guo, X., Zhou, J., 2018. Origins of carbonate spherulites: Implications for Brazilian Aptian pre-salt reservoir. Sediment. Geol. 365, 21–33. https://doi.org/10.1016/j.sedgeo.2017.12.024

Choquette, P.W., James, N.P., 1987. Diagenesis# 12. Diagenesis in Limestones -3. The deep burial environment. Geosci. Canada 14, 3–35.

Choquette, P.W., Pray, L.C., 1970. Geologic Nomenclature and Classification of Porosity in Sedimentary Carbonates. Am. Assoc. Pet. Geol. Bull. 54, 207–250. https://doi.org/10.1306/5D25C98B-16C1-11D7-8645000102C1865D

de Graaf, S., Reijmer, J.J.G., Bertotti, G. V., Bezerra, F.H.R., Cazarin, C.L., Bisdom, K., Vonhof, H.B., 2017. Fracturing and calcite cementation controlling fluid flow in the shallow-water carbonates of the Jandaíra Formation, Brazil. Mar. Pet. Geol. 80, 382–393. https://doi.org/10.1016/j.marpetgeo.2016.12.014

Fairbridge, R.W., 1967. Phases of Diagenesis and Authigenesis, in: Developments in Sedimentology. pp. 19–89. https://doi.org/10.1016/S0070-4571(08)70841-0

Fernandes, A.L., Medeiros, W.E., Bezerra, F.H.R., Oliveira, J.G., Cazarin, C.L., 2015. GPR investigation of karst guided by comparison with outcrop and unmanned aerial vehicle imagery. J. Appl. Geophys. 112, 268–278. https://doi.org/10.1016/j.jappgeo.2014.11.017

Folk, R.L., 1974. The Natural History Of Crystalline Calcium Carbonate: Effect of Magnesium Content And Salinity. J. Sediment. Res. 44, 40–53. https://doi.org/10.1306/74D72973-2B21-11D7-8648000102C1865D

Folk, R.L., 1965. Some aspects of recrystallization in ancient limestones. SEPM Spec. Publ. 13, 14–48.

Ford, D., 1988. Characteristics of Dissolutional Cave Systems in Carbonate Rocks, in: Paleokarst. Springer New York, New York, NY, pp. 25–57. https://doi.org/10.1007/978-1-4612-3748-8_2

Ford, D., Williams, P., 2007. Karst Hydrogeology and Geomorphology. John Wiley & Sons Ltd,., West Sussex, England. https://doi.org/10.1002/9781118684986

Ford, D.C., Williams, P.W., 2013. Karst geomorphology and hydrology, Second edi. ed. John Wiley & Sons.

Friedman, G.M., 1964. Early Diagenesis and Lithification in Carbonate Sediments. SEPM J. Sediment. Res. 34, 777–813. https://doi.org/10.1306/74D71195-2B21-11D7-8648000102C1865D

Giuffrida, A., Agosta, F., Rustichelli, A., Panza, E., La Bruna, V., Eriksson, M., Torrieri, S., Giorgioni, M., 2020. Fracture stratigraphy and DFN modelling of tight carbonates, the case study of the Lower Cretaceous carbonates exposed at the Monte Alpi (Basilicata, Italy). Mar. Pet. Geol. 112, 104045. https://doi.org/10.1016/j.marpetgeo.2019.104045

Giuffrida, A., La Bruna, V., Castelluccio, P., Panza, E., Rustichelli, A., Tondi, E., Giorgioni, M., Agosta, F., 2019. Fracture simulation parameters of fractured reservoirs: Analogy with outcropping carbonates of the Inner Apulian Platform, southern Italy. J. Struct. Geol. 123, 18–41. https://doi.org/10.1016/j.jsg.2019.02.007

Goldberg, K., Kuchle, J., Scherer, C., Alvarenga, R., Ene, P.L., Armelenti, G., De Ros, L.F., 2017. Re-sedimented deposits in the rift section of the Campos Basin. Mar. Pet. Geol. 80, 412–431. https://doi.org/10.1016/j.marpetgeo.2016.11.022

Goldscheider, N., Drew, D., 2007. Methods in Karst Hydrogeology, in: IAH: International Contributions to Hydrogeology, 26. CRC Press/Balkema, Taylor & Francis Group. pp. 9–23.

Gutiérrez, F., Fabregat, I., Roqué, C., Carbonel, D., Zarroca, M., Linares, R., Yechieli, Y., García-Arnay, Á., Sevil, J., 2019. Sinkholes in hypogene versus epigene karst systems, illustrated with the hypogene gypsum karst of the Sant Miquel de Campmajor Valley, NE Spain. Geomorphology 328, 57–78. https://doi.org/10.1016/j.geomorph.2018.12.003

Hackspacher, P.C., Corsino, A.R., Srivastava, N.K., Tiriba, V.F., 1985. A Falha de Afonso Bezerra como evidência de significativo tectonismo frágil NW-SE, na Bacia Potiguar emersa – RN. Bol. do Dep. Geol. 10, 33–44.

Hajikazemi, E., Al-Aasm, I.S., Coniglio, M., 2010. Subaerial exposure and meteoric diagenesis of the Cenomanian-Turonian Upper Sarvak Formation, southwestern Iran. Geol. Soc. London, Spec. Publ. 330, 253–272. https://doi.org/10.1144/SP330.12

Hanshaw, B.B., Back, W., Deike, R.G., 1971. A geochemical hypothesis for dolomitization by ground water. Econ. Geol. 66, 710–724. https://doi.org/10.2113/gsecongeo.66.5.710

Hayer, J.B., 1979. Sandstone diagenesis - The hole truth. Soc. Econ. Paleontol. Mineral. 26, 127–139.

Heald, M.T.H., Larese, R.E., 1973. The Significance of the Solution of Feldspar in Porosity Development. SEPM J. Sediment. Res. 43, 458–460. https://doi.org/10.1306/74D72798-2B21-11D7-8648000102C1865D

Herlinger, R., Zambonato, E.E., De Ros, L.F., 2017. Influence of Diagenesis On the Quality of Lower Cretaceous Pre-salt Lacustrine Carbonate Reservoirs from Northern Campos Basin, Offshore Brazil. J. Sediment. Res. 87, 1285–1313. https://doi.org/10.2110/jsr.2017.70

Heward, A.P., Chuenbunchom, S., Mäkel, G., Marsland, D., Spring, L., 2000. Nang Nuan oil field, B6/27, Gulf of Thailand: Karst reservoirs of meteoric or deep-burial origin? Pet. Geosci. 6, 15–27. https://doi.org/10.1144/petgeo.6.1.15

James, N.P., Choquette, P.W., 1988. Paleokarst. Springer-Verlag New York. https://doi.org/10.1007/978-1-4612-3748-8

James, N.P., Choquette, P.W., 1984. Limestones - the meteoric diagenetic environment. Geosci. Canada 11, 161–194. https://doi.org/10.1029/sc004p0045

James, N.P., Choquette, P.W., 1983. Diagenesis 6. Limestones — The Sea Floor Diagenetic Environment. Geosci. Canada 10, 162–179.

Jonas, E.C., McBride, E.F., 1977. Diagenesis of sandstone and shale: application to exploration for hydrocarbons: Continuing Education Program Publication 1. Dep. Geol. Sci. Univ. Texas Austin, Austin, Texas. 165.

Klimchouk, A., Palmer, A.N., Waele, J. De, Auler, A.S., Audra, P., 2017. Hypogene karst regions and caves of the world. Springer.

Klimchouk, A.B., Ford, D.C., 2000. Types of karst and evolution of hydrogeologic setting, Speleogenesis. Evolution of Karst Aquifers. Huntsville: National Speleological Society.

La Bruna, V., Agosta, F., Lamarche, J., Viseur, S., Prosser, G., 2018. Fault growth mechanisms and scaling properties in foreland basin system: The case study of Monte Alpi, Southern Apennines, Italy. J. Struct. Geol. 116, 94–113. https://doi.org/10.1016/J.JSG.2018.08.009

La Bruna, V., Agosta, F., Prosser, G., 2017. New insights on the structural setting of the Monte Alpi area, Basilicata, Italy. Ital. J. Geosci. 136, 5–22.

Lamarche, J., Lavenu, A.P.C., Gauthier, B.D.M., Guglielmi, Y., Jayet, O., 2012. Relationships between fracture patterns, geodynamics and mechanical stratigraphy in Carbonates (South-East Basin, France). Tectonophysics 581, 231–245. https://doi.org/10.1016/j.tecto.2012.06.042

Land, L.S., 1980. The isotopic and trace element geochemistry of dolomite: the state of the art, in: Concepts and Models of Dolomitization. SEPM Special Publication No 28. pp. 87–110.

Li, H., Bai, H., Wu, J., Zhao, H., Ma, K., 2017. A method for prevent water inrush from karst collapse column: a case study from Sima mine, China. Environ. Earth Sci. 76, 1–10. https://doi.org/10.1007/s12665-017-6831-2

Loucks, R. G. Handford, C.R., 1992. Origin and recognition of fractures, breccias, and sediment fills in paleocave-reservoir networks. Permian Basin Sect. SEPM Publ. 92, 31–44.

Lucia, F.J., 2007. Carbonate reservoir characterization: An integrated approach, 2nd ed. Springer-Verlag Berlin Heidelberg. https://doi.org/10.1007/978-3-540-72742-2

Mádl-Szőnyi, J., Erőss, A., Tóth, Á., 2017. Fluid Flow Systems and Hypogene Karst of the Transdanubian Range, Hungary—With Special Emphasis on Buda Thermal Karst, in: Hypogene Karst Regions and Caves of the World. pp. 267–278. https://doi.org/10.1007/978-3-319-53348-3_17

Matos, R.M.D., 1992. The Northeast Brazilian Rift System. Tectonics 11, 766–791. https://doi.org/10.1029/91TC03092

Matthews, R.K., 1974. A process approach to diagenesis of reefs and reef associated limestones. Soc. Econ. Paleontol. Mineral. 18, 234–256.

McBride, E.F., 1977. Secondary porosity-importance. Gulf Coast Assoc. Geol. Soc. Trans. 27, 121–122.

Menezes, D.F., Bezerra, F.H., Balsamo, F., Arcari, A., Maia, R.P., Cazarin, C.L., 2020. Subsidence rings and fracture pattern around dolines in carbonate platforms – Implications for evolution and petrophysical properties of collapse structures. Mar. Pet. Geol. 113, 104113. https://doi.org/10.1016/j.marpetgeo.2019.104113

Monroe, W.H., 1970. A glossary of Karst terminology. https://doi.org/10.3133/wsp1899K

Moore, C., 2001. Carbonate reservoirs: Porosity, Evolution and Diagenesis in a Sequence Stratigraphic Framework.

Moore, C.H., 1989. Carbonate diagenesis and porosity. Elsevier.

Moore, C.H., Wade, W.J., 2013. Carbonate reservoirs: Porosity and diagenesis in a sequence stratigraphic framework. Newnes.

Morais Neto, J.M., Hegarty, K., Alkmin, F., Matos, R., Karner, G., 2000. Uplift and erosion in the Borborema Province, Northeast Brazil: Insights from Apatite Fission Track Analysis, in: 31st International Geological Congress. Rio de Janeiro.

Morais Neto, J.M., Hegarty, K.A., Karner, G.D., Alkmim, F.F., 2009. Timing and mechanisms for the generation and modification of the anomalous topography of the Borborema Province, northeastern Brazil. Mar. Pet. Geol. 26, 1070–1086. https://doi.org/10.1016/j.marpetgeo.2008.07.002

Morse, J.W., Mackenzie, F.T., 1990. Geochemistry of sedimentary carbonates. Elsevier Scientific Publication Co., New York, USA.

Palmer, A.N., 1991. Origin and morphology of limestone caves. Geol. Soc. Am. Bull. 103, 1–21.

Palmer, T.J., Hudson, J.D., Wilson, M.A., 1988. Palaeoecological evidence for early aragonite dissolution in ancient calcite seas. Nature 335, 809–810.

Pessoa Neto, O.C., Soares, U.M., Silva, J.G.F., Roessner, E.H., Florêncio, C.P., Souza, C.A.V., 2007. Bacia Potiguar. Bol. Geociências da Petrobras 15, 357–369.

Rabelo, J.G., Maia, R.P., Bezerra, F.H.R., Silva, C.C.N., 2020. Karstification and fluid flow in carbonate units controlled by propagation and linkage of mesoscale fractures, Jandaíra Formation, Brazil. Geomorphology 357, 107090. https://doi.org/10.1016/j.geomorph.2020.107090

Rabelo, J.G., Silva, A.T., Bezerra, F.H.R., Moraes, A., 2015. Modelagem numérica da deformação em carbonatos e implicações na formação de carste. Geol. USP. Série Científica 15, 99. https://doi.org/10.11606/issn.2316-9095.v15i2p99-110

Rajaram, H., Cheung, W., Chaudhuri, A., 2009. Natural analogs for improved understanding of coupled processes in engineered earth systems: examples from karst system evolution. Curr. Sci. 97, 1162–1176.

Rustichelli, A., Agosta, F., Tondi, E., Spina, V., 2013. Spacing and distribution of bed-perpendicular joints throughout layered, shallow-marine carbonates (Granada Basin, southern Spain). Tectonophysics 582, 188–204. https://doi.org/10.1016/J.TECTO.2012.10.007

Santos Filho, M.A.B., Piovesan, E.K., Fauth, G., Srivastava, N.K., 2015. Paleoenvironmental interpretation through the analysis of ostracodes and carbonate microfacies: study of the Jandaíra Formation, Upper Cretaceous, Potiguar Basin. Brazilian J. Geol. 45, 23–34. https://doi.org/10.1590/23174889201500010002

Schmidt, V., Mcdonald, D.A., 1979. The role of secondary porosity in the course of sandstone diagenesis. SEPM Spec. Publ. 26, 175–207.

Schmidt, V., McDonald, D.A., 1979. The role of secondary porosity in the course of sandstone diagenesis. Soc. Econ. Paleontol. Mineral. 26, 175–207.

Scholle, P.A., Ulmer-Scholle, D.S., 2003. A color guide to the petrography of carbonate rocks : grains, textures, porosity, diagenesis. AAPG.

Silva, O.L., Bezerra, F.H.R., Maia, R.P., Cazarin, C.L., 2017. Karst landforms revealed at various scales using LiDAR and UAV in semi-arid Brazil: Consideration on karstification processes and methodological constraints. Geomorphology 295, 611–630. https://doi.org/10.1016/J.GEOMORPH.2017.07.025

Stafford, K.W., Nance, R., Rosales-Lagarde, L., Boston, P.J., 2008. Epigene and hypogene karst manifestations of the Castile Formation: Eddy County, New Mexico and Culberson County, Texas, USA. Int. J. Speleol. 37, 83–98.

Stoessell, R.K., Moore, C.H., 1983. Chemical Constraints and Origins of Four Groups of Gulf Coast Reservoir Fluids. Am. Assoc. Pet. Geol. Bull. 67, 896–906. https://doi.org/10.1306/03B5B6C8-16D1-11D7-8645000102C1865D

Sujkowski, Z.L., 1958. Diagenesis. Am. Assoc. Pet. Geol. Bull. 42, 2692–2717. https://doi.org/10.1306/0BDA5C09-16BD-11D7-8645000102C1865D

Taylor, J.M., 1950. Pore-Space Reduction in Sandstones. Am. Assoc. Pet. Geol. Bull. 34, 701–716. https://doi.org/10.1306/3D933F47-16B1-11D7-8645000102C1865D

Tibana, P., Terra, G.J.S., 1981. Seqüências carbonáticas do cretáceo na Bacia Potiguar. Bol. Técnico da Petrobrás 24, 174–183.

Tucker, M.E., 2001. Sedimentary petrology : an introduction to the origin of sedimentary rocks, 3rd ed. Blackwell Science.

Tucker, M.E., Wright, V.P., 1990. Diagenetic Processes, Products and Environments, in: Carbonate Sedimentology. Blackwell Publishing Ltd., Oxford, UK, pp. 314–364. https://doi.org/10.1002/9781444314175.ch7

Upchurch, S., Scott, T.M., Alfieri, M.C., Fratesi, B., Dobecki, T.L., 2019. Epigene and Hypogene Karst, in: The Karst Systems of Florida. Springer, Cham., pp. 359–441. https://doi.org/10.1007/978-3-319-69635-5_8

Vacher, H.L., Mylroie, J.E., 2002. Eogenetic karst from the perspective of an equivalent porous medium. Carbonates and Evaporites 17, 182–196. https://doi.org/10.1007/BF03176484

Vahrenkamp, V.C., Swar, P.K., 1994. Late Cenozoic dolomites of the Bahamas: metastable analogues for the genesis of ancient platform dolomites, in: Special Publications of Internacional Association of Sedimentologists. pp. 133–153.

Wang, B., Al-Aasm, I.S., 2002. Karst-controlled diagenesis and reservoir development: Example from the Ordovician main-reservoir carbonate rocks on the eastern margin of the Ordos basin, China. Am. Assoc. Pet. Geol. Bull. 86, 1639–1658.

Weidlich, O., 2010. Meteoric diagenesis in carbonates below karst unconformities: Heterogeneity and control factors. Geol. Soc. Spec. Publ. 329, 291–315. https://doi.org/10.1144/SP329.12

White, W.B., 1977. Role of solution kinetics in the development of karst aquifers. Int. Assoc. Hydrogeol. 12, 503–517.

Wilson, M.D., Stanton, P.T., 1994. Diagenetic mechanisms of porosity and permeability reduction and enhancement. Soc. Sediment. Geol. 3–44.

Worden, R.H., Burley, S.D., 2003. Sandstone diagenesis: the evolution of sand to stone. Sandstone Diagenes. Recent Anc. 4, 3–44.

Xavier Neto, P., Medeiros, W.E., 2006. A practical approach to correct attenuation effects in GPR data. J. Appl. Geophys. 59, 140–151. https://doi.org/10.1016/j.jappgeo.2005.09.002

Youssef, A.A.A., Awotunde, A.A., 2019. Modelling fluid flow in karst reservoirs using Darcy Model with estimated permeability distribution. Comput. Geosci. 133, 104311. https://doi.org/10.1016/j.cageo.2019.104311

Zoback, M.D., 2007. Reservoir Geomechanics. Cambridge University Press.

ANEXO A

Coordenadas das colunas estratigráficas.

Colunas estratigráficas	Latitude	Longitude
Coluna 1	-5.593785°	-37.825617°
Coluna 2	-5.594589°	-37.826798°
Coluna 3	-5.590024°	-37.827358°
Coluna 4	-5.594057°	-37.826479°
Coluna 5	-5.594828°	-37.826959°

ANEXO B

Dados coletados pelo martelo de Schmidt. Legenda: Cx = Camada x, Cx/y = Contato da camada x com a camada y.

Coluna	C1	C1/2	C2	C2/3	C3	C3/4	C4	C4/5	C5	C5/6	C6	C6/7	C7	C7/8	C8
Coluna 1	56	56	58	40	56	42	56	56	56	56	48	50	48	50	46
Coluna 1	60	58	60	48	58	44	54	58	58	58	46	52	48	42	46
Coluna 1	58	54	60	46	56	44	56	50	58	58	42	48	48	44	48
Coluna 1	58	58	58	50	58	46	54	58	58	54	44	48	48	54	44
Coluna 1	58	52	60	46	58	40	58	58	56	58	44	50	48	52	48
Coluna 1	60	56	58	48	56	42	60	54	57	54	48	52	48	50	46
Coluna 1	58	52	62	47	58	46	56	56	58	52	40	46	51	52	50
Coluna 1	56	56	59	46	54	48	58	58	58	56	44	48	51	44	46
Coluna 1	58	54	56	44	56	40	56	58	57	52	46	50	51	48	44
Coluna 1	58	54	60	48	54	40	54	58	58	56	46	50	48	52	46
Média	58.0	55.0	59.1	46.3	56.4	43.2	56.2	56.4	57.4	55.4	44.8	49.4	48.9	48.8	46.4
Densidade (g/cm³)	2.59	2.65	2.56	2.48	2.63	2.68	2.69	2.67	2.69	2.61	2.62	2.61	2.6	2.66	2.68
Densidade (kN/m³)	25.4	26.0	25.1	24.3	25.8	26.3	26.4	26.2	26.4	25.6	25.7	25.6	25.5	26.1	26.3
Resistência a compressão uniaxial (MPa)	180	170	190	85	180	85	180	178	190	150	92	115	110	120	115

Coluna	C1	C1/2	C2	C2/3	C3	C3/4	C4 (1)	C4 (2)	C4/5	C5	C5/6	C6
Coluna 2	52	42	52	52	56	48	50	52	44	54	50	42
Coluna 2	50	44	54	54	50	42	54	46	50	50	46	45
Coluna 2	52	46	54	48	52	44	49	52	46	52	46	45
Coluna 2	53	44	54	56	44	44	45	51	48	46	48	48
Coluna 2	50	48	53	56	54	48	48	50	48	48	50	48
Coluna 2	52	44	46	56	50	44	52	53	52	50	48	40
Coluna 2	52	42	52	54	54	46	50	46	46	48	48	45
Coluna 2	54	44	50	56	46	40	46	50	48	50	47	45
Coluna 2	54	44	53	55	48	44	48	49	52	48	48	50
Coluna 2	48	44	46	54	48	46	52	51	46	46	50	45
Média	51.7	44.2	51.4	54.1	50.2	44.6	49.4	50.0	48.0	49.2	48.1	45.3
Densidade (g/cm^3)	2.64	2.58	2.57	2.66	2.51	2.68	2.50	2.50	2.63	2.69	2.67	2.57
Densidade (kN/m^3)	25.9	25.3	25.2	26.1	24.6	26.3	24.5	24.5	24.5	26.4	26.2	26.2
Resistência a compressão uniaxial (MPa)	135	85	125	160	110	95	105	110	95	125	115	100

Coluna	C1	C1/2	C2	C2/3	C3	C3/4	C4	C4/5	C5	C5/6	C6	C6/7	C7
Coluna 4	51	48	45	41	51	50	52	44	40	48	46	47	52
Coluna 4	44	46	48	52	52	54	49	49	48	48	48	48	51
Coluna 4	50	39	42	51	45	54	52	50	46	48	54	46	48
Coluna 4	54	40	48	50	52	56	46	48	40	49	40	48	50
Coluna 4	45	40	41	52	52	55	48	49	50	46	52	48	53
Coluna 4	50	44	49	49	51	54	51	50	44	46	43	44	50
Coluna 4	53	39	52	47	44	52	52	48	51	42	45	47	48
Coluna 4	57	46	52	52	52	53	50	50	46	52	50	49	52
Coluna 4	45	40	40	50	48	50	48	44	40	50	52	49	54
Coluna 4	53	48	47	51	52	55	49	48	43	48	50	42	54
Média	50.2	43.6	46.4	49.5	49.9	53.3	49.7	48.0	45.1	47.7	48.7	46.8	51.1
Densidade (g/cm^3)	2.62	2.77	2.69	2.74	2.64	2.71	2.71	2.72	2.68	2.76	2.70	2.67	2.72
Densidade (kN/m^3)	25.7	27.2	26.4	26.9	25.9	25.9	25.9	26.7	26.7	27.1	27.1	26.2	26.7
Resistência a compressão uniaxial (MPa)	120	95	110	130	130	150	135	115	100	125	125	110	135

ANEXO C

Dados de porosidade e permeabilidade pelo Coreval em plugs horizontais. Observação: as amostras foram retiradas com o martelo geológico e os plugs retirados diretamente com a plugadeira. Legenda: φ_0 (%) = porosidade em pressão ambiente e φ (%) = porosidade em pressão confinante (1000 psi).

Coluna	Tipo de amostra	Camada	Litologia	Nome	Espessura camada (cm)	Porosidade φ_0 (%)	Porosidade φ (%)	Permeabilidade Klikenberg (mD)	Comprimento (mm)	Diâmetro (mm)
Coluna 1	Plug	8	Packstone	CARB0398	33	11.50	11.12	0.073	50.54	24.81
Coluna 1	Plug	7.5	Packstone	CARB0400		8.94	8.56	0.009	50.46	24.81
Coluna 1	Plug	7	Packstone-grainstone	CARB0397	37	5.93	5.59	0.004	50.59	24.87
Coluna 1	Plug	6.5	Grainstone	CARB0395		4.52	4.23	0.001	50.43	24.5
Coluna 1	Amostra	6	Grainstone	CARB0392	87	15.80	15.48	0.283	48.35	24.67
Coluna 1	Plug	5.5	Packstone-grainstone	CARB0390		5.36	5.05	0.006	50.71	24.73
Coluna 1	Plug	5	Packstone	CARB0388	55	8.03	7.66	0.022	50.4	24.47
Coluna 1	Plug	4.5	Packstone	CARB0386		7.22	6.86	0.004	50.48	24.79
Coluna 1	Plug	4	Packstone	CARB0385	70	9.12	8.74	0.005	48.34	25.01
Coluna 1	Plug	3.5	Packstone	CARB0382		11.00	10.62	0.024	50.48	24.6
Coluna 1	Plug	3	Packstone	CARB0381	24	6.04	5.71	0.002	51.01	24.7
Coluna 1	Plug	2.5	Packstone	CARB0375		1.55	1.42	0.000	50.61	24.75
Coluna 1	Plug	2	Packstone	CARB0377	30	8.26	7.89	0.004	44.94	24.78
Coluna 1	Plug	1.5	Packstone	CARB0373		11.35	10.98	0.027	50.57	24.64
Coluna 1	Plug	1	Grainstone	CARB0378	68	8.29	7.92	0.003	36.12	24.59
Coluna 2	Amostra	6	Packstone	CARB0340	50	7.21	6.85	0.005	43.34	25.25
Coluna 2	Plug	5.5	Packstone	CARB0328		11.10	10.72	0.001	44.9	24.63
Coluna 2	Plug	5	Packstone	CARB0327	40	13.16	12.81	0.099	47.99	24.4
Coluna 2	Plug	4.5	Packstone-grainstone	CARB0325		2.27	2.10	0.004	41.27	24.78
Coluna 2	Plug	4	Grainstone	CARB0324	95	10.04	9.66	0.050	36.24	24.47

Coluna 2	Plug	3.5	Grainstone	CARB0321		5.78	5.45	0.181	34.58	24.58
Coluna 2	Plug	3	Grainstone	CARB0319	40	5.55	5.23	0.001	49.65	24.48
Coluna 2	Plug	2.5	Grainstone	CARB0318		11.46	11.09	0.031	34.41	24.51
Coluna 2	Plug	2	Packstone-grainstone	CARB0315	70	9.78	9.40	0.015	33.86	24.43
Coluna 2	Plug	1.5	Packstone-grainstone	CARB0329		8.10	7.73	0.008	48.15	24.47
Coluna 2	Plug	1	Packstone	CARB0313	14	10.20	9.82	0.041	41.56	24.39
Coluna 3	Samples	10	Crystalline carbonate	CARB0362	57	10.58	10.20	0.192	51.56	25.07
Coluna 3	Plug	9.5	Crystalline carbonate	CARB0358		3.69	3.44	0.001	50.37	24.75
Coluna 3	Plug	9	Mudstone	CARB0359	67	7.21	6.85	0.003	50.52	24.5
Coluna 3	Plug	8.5	Grainstone	CARB0356		10.88	10.51	0.010	50.56	24.56
Coluna 3	Amostra	8	Grainstone	CARB0363	15	7.58	7.22	0.001	51.21	24.69
Coluna 3	Plug	7.5	Grainstone	CARB0354		15.92	15.61	10.568	50.66	24.78
Coluna 3	Amostra	7	Grainstone	CARB0365	60	16.95	16.64	0.109	15.45	25.19
Coluna 3	Plug	6.5	Packstone-grainstone	CARB0352		5.98	5.64	0.002	50.58	24.82
Coluna 3	Amostra	6	Packstone-grainstone	CARB0367	40	8.84	8.46	0.178	19.8	25.35
Coluna 3	Plug	5.5	Packstone-grainstone	CARB0349		7.13	6.78	0.007	50.66	24.78
Coluna 3	Amostra	5	Grainstone	CARB0366	64	12.34	11.97	0.174	17.42	25.22
Coluna 3	Plug	4.5	Grainstone	CARB0345		6.58	6.23	0.006	50.52	24.73
Coluna 3	Amostra	4	Grainstone	CARB368	10	12.28	11.91	0.065	18.68	25.11
Coluna 3	Plug	3.5	Packstone	CARB0348		8.30	7.93	0.013	50.46	24.74
Coluna 3	Amostra	3	Grainstone	CARB0369	37	8.59	8.21	0.007	51.09	25.22
Coluna 3	Plug	2.5	Packstone	CARB0343		8.55	8.18	0.006	50.54	24.76
Coluna 3	Amostra	2	Packstone	CARB0370	50	15.79	15.47	0.276	51.35	25.1
Coluna 3	Plug	1.5	Packstone	CARB0341		13.74	13.39	2.222	50.35	24.64
Coluna 3	Amostra	1	Packstone	CARB0371	20	12.46	12.09	0.033	50.9	25.24
Coluna 5	Amostra	7	Packstone	CARB0421	40	10.48	10.10	0.160	51.12	25.22

Coluna 4	Plug	6.5	Packstone	CARB0413		4.24	3.97	0.002	36.02	24.8
Coluna 4	Amostra	6	Grainstone	CARB0420	35	9.58	9.20	0.159	50.69	25.11
Coluna 4	Plug	5.5	Grainstone	CARB0412		12.39	12.02	0.119	31.95	24.7
Coluna 4	Amostra	5	Grainstone	CARB0419	44	12.52	12.16	0.792	14.95	25.09
Coluna 4	Plug	4.5	Grainstone	CARB0409		12.24	11.87	0.085	35.84	24.75
Coluna 4	Amostra	4	Grainstone	CARB0418	37	8.53	8.15	0.008	50.94	25.18
Coluna 4	Plug	3.5	Grainstone	CARB0407		6.66	6.31	0.008	37.39	24.83
Coluna 4	Plug	3	Grainstone	CARB0406	70	9.77	9.39	0.034	38.45	24.78
Coluna 4	Plug	2.5	Grainstone	CARB0404		13.56	13.20	0.103	36.19	24.76
Coluna 4	Amostra	2	Grainstone	CARB0416	40	8.58	8.20	0.222	31	25.25
Coluna 4	Plug	1.5	Grainstone	CARB0402		12.02	11.65	0.165	34.14	24.71
Coluna 4	Amostra	1	Packstone	CARB0415	20	5.64	5.32	0.001	50.95	25.15

ANEXO D

Dados de porosidade e permeabilidade pelo Coreval em plugs verticais. Observação: as amostras foram retiradas com o martelo geológico e os plugs retirados diretamente com a plugadeira. Legenda: φ_0 (%) = porosidade em pressão ambiente e φ (%) = porosidade em pressão confinante (1000 psi).

Foco nos estilólitos	Coluna	Tipo de amostra	Camada	Nome	Porosidade φ_0 (%)	Porosidade φ (%)	Permeabilidade Klikenberg (mD)
Não	Coluna 1	Plug	8	CARB0933B	7.80	7.43	0.009
Não	Coluna 1	Plug	7	CARB0932B	6.00	5.66	0.006
Não	Coluna 1	Plug	6	CARB0931C	5.87	5.54	0.016
Não	Coluna 1	Plug	5	CARB0930B	6.21	5.87	0.006
Não	Coluna 1	Plug	4.5	CARB0929B	6.45	6.10	0.011
Não	Coluna 1	Plug	4	CARB0928B	3.59	3.34	0.003
Não	Coluna 1	Plug	2.5	CARB0927E	3.33	3.09	0.001
Não	Coluna 1	Plug	1.5	CARB 0926B	7.56	7.20	0.008
Sim	Coluna 1	Plug	8	CARB0933A1	12.49	12.12	0.078
Sim	Coluna 1	Plug	7	CARB0932A2	12.05	11.68	0.061
Sim	Coluna 1	Plug	6	CARB0931D2	14.83	14.49	0.142
Sim	Coluna 1	Plug	5	CARB0930A2	10.57	10.19	0.011
Sim	Coluna 1	Plug	4.5	CARB0929A1	10.91	10.53	0.004
Sim	Coluna 1	Plug	4	CARB0928A2	10.57	10.19	0.011
Sim	Coluna 1	Plug	2.5	CARB0927B2	8.02	7.65	0.002
Sim	Coluna 1	Plug	1.5	CARB 0926A2	9.78	9.40	0.003
Não	Coluna 2	Plug	6.8	CARB0941 C	8.73	8.35	0.034
Não	Coluna 2	Plug	5	CARB0940 B	9.82	9.44	0.037
Não	Coluna 2	Plug	4.8	CARB0939 B	6.40	6.05	0.017
Não	Coluna 2	Plug	4	CARB0938 B	4.34	4.06	-0.208
Não	Coluna 2	Plug	3.5	CARB0937 III4	5.92	5.59	0.013
Não	Coluna 2	Plug	2.8	CARB0936 B	4.22	3.94	0.179

Não	Coluna 2	Plug	1	CARB0935 IB	2.23	2.07	0.005
Não	Coluna 2	Plug	1.5	CARB0934 3IA	2.37	2.19	0.001
Sim	Coluna 2	Plug	6.8	CARB0941 A1	13.48	13.13	0.095
Sim	Coluna 2	Plug	5	CARB0940 A1	15.36	15.04	0.159
Sim	Coluna 2	Plug	4.8	CARB0939 A1	14.66	14.32	0.149
Sim	Coluna 2	Plug	4	CARB0938 A2	11.50	11.12	0.067
Sim	Coluna 2	Plug	3.5	CARB0937 1B	9.70	9.32	0.051
Sim	Coluna 2	Plug	2.8	CARB0936 A1	13.64	13.29	0.093
Sim	Coluna 2	Plug	1	CARB0935 A	15.07	14.74	0.112
Sim	Coluna 2	Plug	1.5	CARB0934 2IA	12.80	12.44	0.014
Não	Coluna 3	Amostra	10	CARB0362	10.95	10.57	0.113
Não	Coluna 3	Amostra	9	CARB0360	13.50	13.15	4.040
Não	Coluna 3	Amostra	8	CARB0363	13.31	12.96	0.034
Não	Coluna 3	Amostra	7	CARB0365	17.26	16.96	0.043
Não	Coluna 3	Amostra	6	CARB0366	12.55	12.18	0.191
Não	Coluna 3	Amostra	5	CARB0367	11.63	11.26	0.033
Não	Coluna 3	Amostra	4	CARB0368	14.42	14.08	0.113
Não	Coluna 3	Amostra	3	CARB0369	9.30	8.92	0.017
Não	Coluna 3	Amostra	2	CARB0370	15.79	15.48	0.126
Não	Coluna 3	Amostra	1	CARB0371	11.75	11.38	0.034
Não	Coluna 4	Amostra	7	CARB0421	10.61	10.23	0.057
Não	Coluna 4	Amostra	6	CARB0420	8.80	8.42	0.009
Não	Coluna 4	Amostra	5	CARB0419	10.38	10.00	0.024
Não	Coluna 4	Amostra	4	CARB0418	9.97	9.59	0.033
Não	Coluna 4	Amostra	3	CARB0417	11.68	11.31	0.059
Não	Coluna 4	Amostra	2	CARB0416	9.44	9.06	0.073
Não	Coluna 4	Amostra	1	CARB0415	8.14	7.77	0.002